Massively parallel reporter assay for mapping gene-specific regulatory regions at single nucleotide resolution

Authors: Alastair J Tulloch[1,3], Ryan N Delgado[1,3], Rinaldo Catta-Preta[1,3,4], Constance L Cepko[1,2,3]

1. Department of Genetics, Harvard Medical School, Boston, MA 02115, USA.
2. Department of Ophthalmology, Harvard Medical School, Boston, MA 02115, USA.
3. Howard Hughes Medical Institute, Harvard Medical School, Boston, MA 02115, USA.
4. Current affiliations: Ocular Genomics Institute, Mass Eye and Ear, Boston, MA 02114, USA and Department of Ophthalmology, Harvard Medical School, Boston, MA 02114, USA

Corresponding author: Constance L. Cepko, Department of Genetics, Harvard Medical School, 77 Avenue Louis Pasteur, Boston MA 02115, USA, Ph (617) 432-7618, Fax (617) 432-7595
cepko@genetics.med.harvard.edu

ABSTRACT

Precise gene regulation is essential for the development and function of complex tissues, yet comprehensive mapping of *cis*-regulatory modules (CRMs) remains challenging due to limitations in throughput, resolution, and the ability to assay within specific cell types. Here, we introduce two complementary approaches—a locus-specific massively parallel reporter assay (LS-MPRA) and a degenerate MPRA (d-MPRA)—specifically designed to address some of these shortcomings. LS-MPRA leverages bacterial artificial chromosomes (BACs) to generate high-complexity libraries spanning large genomic regions, enabling unbiased interrogation of millions of DNA fragments potentially relevant for the regulation of a specific gene or set of genes. The d-MPRA employs systematic mutagenesis to resolve the functional architecture of CRMs at nucleotide resolution, thereby nominating critical nucleotides as potential TF binding sites, or for other regulatory roles.

We applied these methods to retinal genes that are stably expressed in differentiated cells of the retina, in rod photoreceptors and in subsets of bipolar interneurons, using both *in vivo* and *ex vivo* preparations of mouse tissue. LS-MPRA recapitulated some of the known CRMs for these genes—such as the proximal promoter region of *Rho*—and identified potentially novel CRMs, including those located within neighboring genes. The method was then applied to a gene that is dynamically expressed in subsets of retinal progenitor cells, *Olig2,* where it identified three distinct CRM regions (Olig2-NR1, NR2, and NR3). D-MPRA and subsequent motif analyses nominated critical TF binding sites within these regions. CUT&RUN experiments confirmed direct binding of these candidates. Moreover, extending LS-MPRA to chick retina and spinal cord demonstrated the applicability of these methods across species and tissues.

Together, the integrated LS-MPRA and d-MPRA strategies provide a robust, high-resolution platform for discovery of the *cis*-regulatory code underlying tissue-specific gene expression. It does not require prior knowledge of potential CRMs, and is quite rapid and straightforward to deploy, using typical molecular biology methods. The fragment size can be scaled to create short CRMs, e.g. for cell type-specific expression within viral vectors. It should

enable CRM discovery at a scale and affordability for laboratories wishing to focus on a particular locus or set of loci.

INTRODUCTION

The precise regulation of gene expression is fundamental to the development and function of complex tissues. Intricate transcriptional programs govern cell fate decisions and ensure the proper spatial and temporal expression of genes. Central to these programs are *cis*-regulatory modules (CRMs), which integrate combinatorial inputs from transcription factors (TFs) and other regulatory mechanisms to orchestrate gene expression in a context-dependent manner. Despite extensive research identifying individual enhancers and promoters, a comprehensive understanding of the regulatory landscapes that dictate cellular diversity remains elusive. This gap is largely attributable to limitations in conventional assays regarding throughput, resolution, and the reliance on cultured cells.

Massively parallel reporter assays (MPRAs) have emerged as powerful platforms for systematically interrogating enhancer activity (Agarwal *et al.*, 2025, Arnold *et al.*, 2013, Inoue & Ahituv, 2015, Lagunas *et al.*, 2023, McAfee *et al.*, 2022, Melnikov *et al.*, 2012, Shen *et al.*, 2016a). Most MPRAs rely on predetermined sets of DNA fragments, identified through chromatin, RNA, and/or bioinformatic analyses. They are often broad in scale, in some cases, extending to genome-wide analyses. Constructing such libraries is both time-consuming and resource-intensive, and the selection process can be inherently biased. When an investigator aims to identify CRMs for only one or a few genes, most MPRAs are more complex and expensive than is required, and genome-wide MPRA libraries may lack the resolution needed to detect CRMs for genes that are transiently expressed or limited to small cell populations. CRMs for specific genes might not only lead to an understanding of gene regulation, but they can be used for cell type-specific gene expression for perturbations in specific settings and/or for clinical applications. To provide methods for these latter applications, we developed a locus-specific MPRA (LS-MPRA) that leverages bacterial artificial chromosomes (BACs) to generate highly complex libraries for the unbiased interrogation of millions of fragments surrounding genes of interest (Rabe, 2020). Fragment size can be chosen by the investigator, which is especially useful when a small fragment might be required, e.g. for cell type-specific expression in a viral vector. The LS-MPRA library approach not only identifies potential CRMs under homeostatic conditions, but can be run in a perturbed condition, to identify CRMs that might direct a response to e.g. drug treatment. In addition, we devised a degenerate MPRA (d-MPRA) technique to resolve the functional architecture of CRMs at single-nucleotide resolution. By systematically introducing random point mutations into fragments identified in the LS-MPRA, d-MPRA nominates sites required for repression and/or activation of CRMs. Integration of these data with *de novo* motif discovery, single cell RNA sequencing (scRNA-seq) data, and CUT&RUN assays can be used to further analyze the connection between CRM activity and specific transcriptional regulators.

In this study, we first determined that these methods can identify CRMs for stably expressed, cell type-specific genes, previously identified by our laboratory and others. These assays were successfully carried out in the mouse *in vivo* and in explant cultures. We then investigated the regulation of more challenging genes, *Olig2* and *Ngn2,* that are dynamically expressed within subsets of retinal progenitor cells (RPCs) during development. CRMs for Olig2 were run through the d-MPRA method, where binding sites for known and previously unreported TF regulators of retinal development were identified. Analysis of the patterns of Olig2 RNA expression and those of these predicted TF regulators, within single cells, ruled in the possibility

that the suggested TFs might regulate Olig2 repression and activation. Binding of the suggested TFs was then carried out and was validated by CUT&RUN assays.

These methods can be launched without any prior knowledge of a gene's architecture, and without synthesizing fragments or producing a library of specific PCR products. They offer a modular framework that can be readily adapted to diverse model systems. The methods are straightforward, requiring only basic molecular biology skills. They are rapid, with library preparation taking 1–2 weeks. Moreover, the methods can be run in a multiplexed fashion, allowing one to combine libraries from several BACs.

RESULTS

LS-MPRA for stably expressed cell type-specific genes

The overall LS-MPRA protocol is shown in **Fig. 1A**. Fragment libraries from large contiguous genomic regions (~150–250 kb) within a BAC encoding a locus of interest are generated. Essentially random DNA fragments are generated by digestion by the NEBNext® Ultra™ II FS DNA Module enzyme, followed by size selection on an agarose gel. The fragments are then cloned into a barcode library with a synthetic, minimal promoter (TATAA) and GFP, with an intron in the GFP open reading frame (ORF), to allow selection of GFP cDNA vs contaminating plasmid DNA, for some applications. The barcodes are located in the 3'UTR and were used to track DNA fragment activity. Because there are many overlapping fragments from a given region, active genomic regions appear as peaks, where barcode signals from each fragment accumulate. Libraries of at least $6.2x10^6$ and as many as $1.3x10^7$ fragments were made (Table S3), with each nucleotide in the BAC residing in a different position within at least 5000 fragments and as many as 11,000 fragments. BAC libraries are delivered to the cells of interest, in our case by electroporation into the retina. After incubation, a cDNA library is generated using a RT primer that enables capture of barcoded transcripts, followed by PCR amplification. A gel is then run for isolation of the appropriate sized fragments. The cDNA-derived barcodes are sequenced and mapped to the fragment library. Similar to other MPRAs, CRM activity is inferred from cDNA barcode ratio relative to the barcode frequency in the electroporated library.

In order to associate a given DNA fragment with a particular barcode (**Fig. 1B**), an association library, derived from the original LS-MPRA library, is created and sequenced. This association library is made by excision of the minimal promoter and GFP, followed by ligation (**Fig. 1C**). This is followed by paired end sequencing, from the barcode at the 3' end and the fragment with a potential CRM from the 5' end. This allows for the association of each fragment with a specific barcode. This baseline sequencing serves two additional purposes. One is normalization of the barcode reads recovered from electroporated tissues or cells to their frequency within the electroporated library, ensuring that barcode enrichments reflect true CRM activity rather than variability in fragment representation. The second is that it allows mapping of each fragment to the BAC and an assessment of library coverage across the BAC.

As an initial test of the LS-MPRA approach, BAC clones containing genes previously analyzed for CRM activity were selected. These genes are stably expressed in specific cell types of the mature retina. They were *Rho* (rhodopsin), expressed in rod photoreceptors, *Cabp5* (calcium-binding protein 5), expressed in subsets of cone bipolar cells and in rod bipolar cells (Haeseleer *et al.*, 2000, Shekhar *et al.*, 2016), *Grm6* (metabotropic glutamate receptor 6), expressed in all ON-bipolar cells (Ueda *et al.*, 1997), and *Vsx2* (visual system homeobox 2; homolog of *Chx10*), expressed in all bipolar cells and some Mueller glial cells (Hatakeyama *et al.*, 2001, Liu *et al.*, 1994, Rowan & Cepko, 2004). LS-MPRA libraries for each of the BACs encoding these genes were made as described above (library characteristics in Table S3 and Supplemental Document A). The libraries were pooled and electroporated into postnatal day 3 (P3) retinas *in vivo* or *ex vivo,* with sacrifice and/or tissue collection 7 days later. This developmental window was chosen as it is the period when rod photoreceptors and bipolar cells are generated from RPCs, and RPCs are readily electroporated, while postmitotic cells are not. The Rho library was present at 5% the level of the other libraries as rods are the predominant cell type produced at this time (Young, 1985), and *Rho* is a highly expressed gene. This and all

LS-MPRA experiments in this study were performed using three replicates, with each replicate generated by pooling retinas from several animals. Three retinas were pooled following *in vivo* electroporation, and 3–4 retinas were pooled following *ex vivo* electroporation and culture.

Analysis of the sequences of the fragment-association libraries showed that all regions of the BACs were fairly equally represented when aligned to the mouse mm10 reference genome (Library Coverage plots; **Figs. 2, 2S**). When the frequencies of cDNA barcodes representing different genomic regions of each BAC were plotted across the genomic regions, clear signals were observed for all 4 BACs (LS-MPRA plots; **Figs. 2, 2S**). The barcode frequency plot for the Rho LS-MPRA library revealed distinct candidate CRM regions (peaks; **Fig. 2A**) in one, or both, of the *in vivo* and *ex vivo* conditions. Several of these regions are conserved across vertebrate and placental mammal species, correspond to areas of open chromatin, as indicated by ATAC-seq data (Lyu *et al.*, 2021), and are annotated as candidate *cis*-regulatory elements in the mouse ENCODE database (not shown; (Consortium *et al.*, 2020). Consistent with previous reports identifying the Rho proximal promoter region (PPR) at -176bp to +70bp relative to the *Rho* transcription start site (TSS) (Zack *et al.*, 1991), the *in vivo* Rho LS-MPRA revealed a clear CRM peak at -251bp to +65bp (peak **iii**; **Fig. 2A**). The expanded region of interest (ROI; **Fig. 2B**) clearly demarcates the CRM peak (peak **iii**), which correlates with the ATAC-seq open chromatin profiles. Two additional Rho CRMs known to induce reporter expression *in vitro*—the rhodopsin enhancer region (RER; -1.575 kb to -1.476 kb) and the Crx bound region (CBR; -3.165 kb to -2.693 kb) (Corbo *et al.*, 2010, Nie *et al.*, 1996)—exhibited minor peaks only in the *ex vivo* LS-MPRA (peaks **iv,v**).

In addition to the CRM peaks directly associated with *Rho*, two peaks were identified by the Rho LS-MPRA at approximately -123 kb (peak **i**) and -78 kb (peak **ii**) upstream of the *Rho* TSS. These peaks localize within the putative promoter regions of *Rpl32* (a ribosomal RNA gene) and *Ift122* (encoding an intraflaggelar transport protein), respectively, suggesting that the LS-MPRA captured regulatory activity in addition to that of *Rho*. To investigate this possibility, we analyzed publicly available single-cell RNA sequencing (scRNA-seq) data from P8 mouse retina (Clark *et al.*, 2019). In this dataset of 10,200 retinal cells, *Rpl32* was detected in 7,916 cells and *Ift122* in 1,092 cells, while *Rho* was detected in 8,809 cells. The fragment immediately upstream of *Rpl32* was cloned into a plasmid upstream of a TATAA minimal promoter and EGFP reporter, and electroporated *in vivo* into P3 retinas and incubated for 7 days before analysis. GFP expression driven by this fragment was expressed in most electroporated cells (data not shown). Follow up experiments might reveal that this small CRM (237 bp) is active in most tissues, suggesting it would be useful for applications where such breadth of expression driven by a small CRM is desirable. These expression patterns support the notion that some of the CRM activity captured by the Rho LS-MPRA reflects regulatory elements associated with neighboring genes that are co-expressed in retinal cells during this stage of development.

LS-MPRA plots for bipolar cell subtype markers also revealed several relevant peaks. In the Grm6 LS-MPRA, a distinct peak at -8.152kb to -7.857kb relative to the TSS (peak **i, Fig. 2SA**) overlapped with a previously identified CRM (-8.126kb to -7.926kb; (Kim *et al.*, 2008)), which is moderately conserved across vertebrate and placental mammal species and localizes to an area of open chromatin. In the Vsx2 LS-MPRA, two distinct peaks at -37.617kb to -37.364kb and at -17.833kb to -17.559kb relative to the TSS (peaks **ii,iii; Fig. 2SB**) overlapped with a Vsx2 enhancer active in RPCs (-37.726kb to -37.117kb (Buenaventura *et al.*, 2018) or -37.778kb to -36.813kb (Honnell *et al.*, 2022)) and a Vsx2 enhancer active in bipolar cells (-17.724kb to -17.560kb (Kim *et al.*, 2008) or -19.654kb to -15.836kb (Honnell *et al.*, 2022)), respectively. Both

peaks are conserved across vertebrate and placental mammal species and localize to areas of open chromatin. However, a broad region previously described as a Vsx2 enhancer (-2.145kb to +87bp; (Rowan & Cepko, 2005)) did not align with any peaks in the LS-MPRA. Similarly, no peaks in the Cabp5 LS-MPRA (**Fig. 2SC**) corresponded to the known Cabp5 CRM at -289bp to +156bp relative to the TSS (Kim *et al.*, 2008). These results suggest that while LS-MPRA successfully identified several previously characterized CRMs, some known elements did not exhibit significant activity under these experimental conditions.

LS-MPRA for genes expressed dynamically during retinal development

We are interested in how different RPCs produce different types of retinal cells. Previous work has suggested that there are intrinsic differences among different RPCs over time, and even at one time in development (Cepko, 2014). We previously found that Olig2, a transiently expressed proneural basic helix-loop-helix (bHLH) transcription factor, marks a subset of RPCs at each time in development (Hafler *et al.*, 2012, Shibasaki *et al.*, 2007, Trimarchi *et al.*, 2008). It is expressed in neurogenic RPCs that divide one or two times, and produce a limited repertoire of cell types among those born at that time. In the embryonic day 13 or 14 (E13–14) retina, cone photoreceptors and horizontal cells, a type of interneuron, are produced. In the postnatal period, Olig2+ RPCs produce rod photoreceptors and amacrine interneurons. We were interested in the regulators of Olig2 at these two different times, as different CRMs might lead us to the intrinsic differences between embryonic and postnatal RPCs. The Olig2 LS-MPRA library was thus generated (library characteristics in Table S3) and delivered to E14 mouse retinas, which were incubated *ex vivo* for 28 hours. For each of the three experimental replicates, 8 retinas were pooled. Barcode enrichment plots from this library revealed distinct candidate CRM regions (peaks; **Fig. 3A**), several of which are conserved across vertebrate and placental mammalian species and correspond to areas of open chromatin. Notably, two CRM candidate regions identified by LS-MPRA (**Fig. 3B**), located at -1.881 kb to -1.700 kb and -85.027 kb to -84.781 kb relative to the Olig2 TSS, overlap with broader regions previously implicated as potential Olig2 regulatory elements in mouse embryonic stem cells (Chen *et al.*, 2008). Other regions with possible regulatory activity (indicated in **Fig. 3A**), previously identified using *in vitro* assays or in the mouse spinal cord (Fan *et al.*, 2023, Friedli *et al.*, 2010, Sun *et al.*, 2006), did not exhibit CRM activity in the retina by LS-MPRA.

The peaks at-1.881 kb to -1.700 kb were quite small, so an additional assay was run to determine if they were relevant for Olig2 regulation. Knock-out mice for Notch1 have been shown to overproduce cone photoreceptors during the embryonic period, and rod photoreceptors in the neonatal period (Jadhav *et al.*, 2006, Yaron *et al.*, 2006). Moreover, Olig2 expression in mouse retinal explants is also transiently upregulated in response to Notch inhibition (Kaufman *et al.*, 2019). To investigate the precise dynamics of Notch regulation of Olig2 in the E14 retina, as well as to determine if the small CRMs identified in the LS-MPRA were of relevance to Olig2 regulation, E14 retinal explants were treated with the γ-secretase inhibitor, LY411575, which inhibits Notch signaling. Notch inhibition was found to increase endogenous *Olig2* RNA levels in E14 retinas over 24 hours of treatment, with a peak at 12 hours (**Fig. 4A**). Two small Olig2 CRM candidates, one just 5' (-1.881 kb to -1.700 kb) and one 3' (+6.721 kb to +6.933 kb) of the Olig2 TSS, also exhibited an increase in activity, also with a peak at 12 hours post Notch inhibition (**Fig. 4B**). In addition, one CRM within the intron of the Gm41492 predicted gene, at -84.781 kb to -85.027 kb relative to the Olig2 TSS, also exhibited an increase in CRM activity

with Notch inhibition. The three Olig2 potential CRMs, now named Notch signaling-responsive (NR) regions 1, 2, and 3, were conserved, and exhibited open chromatin. Reanalysis of one replicate using only unique barcodes also identified these three peaks, including NR3, indicating that barcode collisions did not account for the minor NR3 peak (see Supplemental Document B). Together, these findings suggest that NR1–3 function as CRMs that respond to disruptions in Notch signaling to enhance Olig2 expression in RPCs that produce cone photoreceptors. More broadly, these experiments demonstrate that the LS-MPRA can be used to rapidly identify CRMs that respond to perturbations that are relevant to the gene under study.

Analysis of cell type-specific CRM activity

To investigate the cellular specificity of the Olig2 CRMs, NR1, NR2, and NR3, each fragment was cloned individually or as a composite into a plasmid with the endogenous Olig2 promoter and TSS (-75bp to +51bp) upstream of an EGFP reporter. First, to determine whether the inclusion of the Olig2 promoter, and/or other sequences within the plasmid, had background transcriptional activity, we electroporated backbone plasmids containing GFP alone or GFP under the Olig2 minimal promoter into E14 retinas (**Fig. 5SA**). Minimal and sporadic *GFP* RNA signal was observed in these controls. This background level was judged to be low enough to allow for assay of specific CRM activity. The Olig2 CRMs were cloned into the backbone plasmid, oriented as they appear in the genome relative to the TSS. These constructs were electroporated into E14 retinas *ex vivo* and incubated for 24 hours before analysis (**Fig. 5A**).

Electroporated cells were identified by expression of the CAG-BFP co-electroporated control plasmid. Immunolabeling for GFP and Olig2 in transverse retinal sections (**Fig. 5B**) revealed that all Olig2+ electroporated cells, identified by immunohistochemistry (IHC), expressed GFP, also identified by IHC, when driven by NR1, NR2, or the combined NR1-3 composite; additionally, most Olig2+ electroporated cells expressed GFP when driven by NR3 alone, albeit at lower levels (**Fig. 5C**, left column; Table S5). These findings suggest that NR1, NR2, and NR3 contain functional CRMs for Olig2, with NR3 exhibiting very weak CRM activity. However, when the GFP+ electroporated cells were examined for Olig2 protein expression using IHC, few GFP+ cells demonstrated detectable Olig2 protein (**Fig. 5C**, middle column; Table S5), and many Olig2- electroporated cells expressed GFP (**Fig. 5C**, right column; Table S5). This lack of correlation raised two possibilities: either NR1-3 CRM activities were not confined to Olig2+ RPCs, and/or the transient nature of Olig2 expression, combined with the stability of EGFP, resulted in a temporal mismatch that limited the detection of co-localized Olig2 protein and GFP protein. This possibility was suggested by the known short half-life of murine Olig2 RNA (~1.66hrs) and protein (~3.5hrs) (Rayon *et al.*, 2020).

We first determined if the short half-lives of Olig2 RNA and protein created a situation where detection of the endogenous Olig2 transcript and protein in the same cell was unlikely. Fluorescent *in situ* hybridization (FISH) for *Olig2* transcript, combined with immunolabeling for Olig2 protein, showed that most cells expressed either the transcript or the protein, but not both simultaneously (**Fig. 6A**). A similar pattern was observed when comparing GFP protein expression and *GFP* transcript levels in retinas electroporated with the NR1 CRM (**Fig. 6B**). This observation might indicate that the NR1 CRM activity is also dynamically regulated. To at least partially accommodate this temporal mismatch when assessing the specificity of the Olig2 CRMs, we examined RNA, rather than protein, for Olig2 and GFP, reasoning that RNA might be a more accurate read-out of both the CRM activity and endogenous Olig2 transcription.

FISH for *Olig2* and *GFP* RNA, along with intrinsic GFP fluorescence (**Fig. 6C**), revealed a pattern similar to the quantification of immunostaining (**Fig. 5C**). The vast majority of *Olig2* RNA+ electroporated cells expressed *GFP* RNA and/or protein when GFP expression was driven by NR1, NR2, or the composite construct (**Fig. 6D**, left column; Table S6). Approximately 40% of *Olig2* RNA+ electroporated cells co-expressed GFP when driven by NR3 alone, further supporting its lower but detectable CRM activity. Importantly, a substantial proportion of *GFP* RNA+ cells co-expressed *Olig2* RNA when GFP was driven by NR1, NR2, or the composite construct (**Fig. 6D**, middle-left column; Table S6), and this proportion exceeded that observed when the analysis was limited to GFP protein+ cells (**Fig. 6D**, middle-right column; Table S6). When the expression of GFP RNA or protein was compared in cells that expressed or did not express *Olig2* RNA, a greater fraction of Olig2+ cells expressed GFP when it was driven by any of the four constructs (Mann-Whitney test with Holm-Šídák method for correcting multiple comparisons, $p<0.05$ each). These findings indicate a significant enrichment of CRM activities in the Olig2+ cells. In addition, these findings suggest that measuring co-localization at the RNA level may provide a more accurate assessment of CRM activity for transiently expressed genes.

D-MPRA for identification of sequences important for CRM activity

To identify nucleotides within potential CRMs that are necessary for their activity, we developed the d-MPRA. Most nucleotides identified are suspected to be within TF binding sites, though other roles, e.g. sites that affect chromatin structure, might also play a role. Libraries with point mutations were created via error-prone PCR amplification of each NR1-3 CRM. Each library was then cloned into a vector backbone. An intraplasmid duplication (IPD) was then made to serve as a barcode before inserting a GFP reporter into the completed library (**Fig. 7A**). In the IPD process, the mutant library was nicked on the plus strand upstream and the minus strand downstream of the mutated CRM fragments. Strand-displacing polymerase, lacking exonuclease activity, extended these nicks, linearizing the libraries such that each end carried an exact copy of a particular mutated fragment. The final step involved inserting a minimal promoter and GFP ORF cassette between the two duplicated CRM copies. The 3' copy of the mutated CRM was thus in the 3' UTR, and served as a barcode in the cDNA (**Fig. 7A**). This configuration allowed the possibility that the 5' and/or 3' mutated CRM could influence transcription of GFP. In addition, it was possible that the 3' fragment could influence the stability of the transcript. To somewhat override this effect, a WPRE sequence was also included in the 3'UTR of all library members. The IPD method was used so that the step of making and sequencing the association library, as was done for the LS-MPRA, was unnecessary.

Mutations reducing positive activity, presumed TF binding that enhances activity, should result in depleted barcode abundance, while those diminishing repressor TF binding should lead to enrichment (**Fig. 7B**). Similar to LS-MPRAs, the abundance of barcodes of mutated fragments was normalized to their baseline abundance in the d-MPRA plasmid libraries.

The d-MPRA libraries for Olig2 NR1-3 CRMs were constructed with a mutational frequency of ~0.02–0.2% per nucleotide and a complexity of at least $2x10^7$ transformants (see Supplemental Document A for mutational rate, co-occurrence across CRMs, and analyses comparing bulk fragments vs singleton mutations). These libraries were electroporated into E14 *ex vivo* retinas, which were incubated for 24 hours before RNA extraction. The 3'UTR region containing transcribed mutated CRMs was reverse transcribed to generate cDNA, PCR amplified, gel purified, indexed, and sequenced. Normalized log2-transformed values were

averaged across replicates, and a sliding window average (window size = 5) was applied to smooth the data and reduce noise. This approach ensured robust comparisons across experimental conditions. The resulting d-MPRA plots for Olig2-NR1 (**Fig. 7C**), Olig2-NR2 (**Fig. 7D**), and Olig2-NR3 (**Fig. 7E**) revealed peaks and troughs, indicating that mutations at multiple sites influence CRM activity. In three independent electroporation experiments for each CRM, the d-MPRA readouts exhibited low variance between experimental replicates. The clear alignment of peaks and troughs with specific nucleotide positions supports the notion that these regions are important for CRM activity.

To identify over-represented sequences in sites corresponding to peaks or troughs in the d-MPRA plots, *de novo* motif discovery analysis, HOMER, was performed. This analysis focused on all three Olig2 CRMs, with an emphasis on NR2, which is proximal to the *Olig2* TSS. Across the Olig2-NR2 region, 16 *de novo* motifs were identified (**Fig. 8A**), several of which overlapped with d-MPRA peaks or troughs. The presence and density of binding motifs in this region are consistent with the open chromatin profile observed in ATAC-seq data. Notably, motifs matching known binding sites for Foxn4, Pax6, Mybl1, and Otx2—recognizable regulators of retinal development (Cvekl & Callaerts, 2017, Farhy *et al.*, 2013, Kaufman *et al.*, 2019, Li *et al.*, 2004, Marquardt *et al.*, 2001, Nishida *et al.*, 2003, Oron-Karni *et al.*, 2008, Remez *et al.*, 2017, Wang *et al.*, 2014)—were detected (**Figs. 8B-D**). Mybl1 and Otx2 motifs (Motifs 1 and 14, respectively) corresponded to troughs in the d-MPRA plot, whereas the shared motif (Motif 3) for Foxn4 (typically an enhancer) and Pax6 (frequently a repressor) did not align with any prominent peaks or troughs (**Fig. 8A**). The shared motif for Foxn4 and Pax6 in Olig2-NR2 likely represents a regulatory balance between activation and repression, reflecting the complex interplay of these TFs in fine-tuning Olig2 expression.

To assess whether RPCs that express Olig2 could use these TFs to regulate Olig2, scRNAseq data (Clark *et al.*, 2019) were examined for co-expression with Olig2 at E14. The dataset, originally generated using the 10X Genomics platform, was further processed in Seurat, where filtering, normalization, and dimensionality reduction was carried out to identify distinct retinal cell populations (**Fig. 8E**). As expected, Olig2 expression was enriched in a subset of neurogenic RPCs (**Fig. 8F**). Notably, Mybl1, Pax6, Foxn4, and Otx2 were co-expressed with Olig2 in subsets of these cells (**Fig. 8G**), with 37.7%, 55.5%, 30.7%, and 67.3% of neurogenic RPCs that expressed Olig2 also expressed Mybl1, Pax6, Foxn4, and Otx2, respectively. The expression of Mybl1, Foxn4, and Otx2 were significantly enriched in Olig2+ RPCs (Fisher's exact test Odds Ratios [OR]: 11.8 [$p<0.0001$], 7.1 [$p<0.0001$], and 8.5 [$p<0.0001$], respectively), whereas Pax6 (OR: 0.96, $p=0.31$) was not, perhaps reflecting a role as a repressor. These results support the hypothesis that these factors are functionally intertwined in the regulation of Olig2 expression.

To examine whether the suggested Olig2 regulatory TF's bind to the Olig2-NR2 CRM, a CUT&RUN analysis was carried out. A significant enrichment of Mybl1, Pax6, and Foxn4 binding, with peaks that aligned with the NR2 region (**Fig. 8H**), provided evidence for their direct regulatory roles via the Olig2-NR2 CRM. Together, these findings suggest that the Olig2-NR2 CRM is a target for multiple retinal developmental regulators, potentially mediating Olig2 expression in neurogenic RPCs.

Using *de novo* motif discovery analysis on Olig2-NR1, 20 motifs were identified (**Fig. 8SA**), some of which correspond to binding sites for several retinal TFs, including Sox4, Sox11, Lhx2, Dlx2, Isl1, Foxp1, Mybl1, and Otx2. These factors play critical roles in retinal development: Sox4 and Sox11 are active in neurogenic RPCs and regulate the generation and

survival of RGCs (Jiang *et al.*, 2013); Lhx2 is suggested to influence the progression of RPC competence states (Gordon *et al.*, 2013); Dlx2 is required for terminal RGC differentiation (de Melo *et al.*, 2005, Zhang *et al.*, 2017); Isl1 is essential in the gene regulatory network governing RGC development (Mu *et al.*, 2008); Foxp1 has been implicated in regulating the competence of RPCs to generate early-born retinal cell types (Zhang *et al.*, 2023); and Mybl1 and Otx2 are known to influence neural progenitor cell cycle regulation (Kaufman *et al.*, 2019), and photoreceptor and horizontal cell development (Nishida *et al.*, 2003, Wang *et al.*, 2014), respectively.

In the d-MPRA analysis, specific motifs in Olig2-NR1 aligned with these predicted TF binding sites. For instance, Motifs 13 and 16 matched shared binding sites for Sox4 and Sox11 (**Fig. 8SB**); scRNA-seq co-expression data of RPCs (**Fig. 8SG**) revealed that 74.1% of Olig2-expressing neurogenic RPCs co-expressed Sox4 (enrichment OR: 5.3 [p<0.0001]) and 89.3% co-expressed Sox11 (enrichment OR: 3.1 [p<0.0001]). In contrast, Motif 11 contained a shared binding site for both Lhx2 and Dlx2 (**Fig. 8SC**); among Olig2+ neurogenic RPCs, 29.6% co-expressed Lhx2 (enrichment OR: 1.0, p=0.94) and 21.1% co-expressed Dlx2 (enrichment OR: 3.7 [p<0.0001]). Motif 8 matched an Isl1 binding site (**Fig. 8SD**) and was associated with only 5.0% co-expression in Olig2+ RPCs (**Fig. 8SG**) (enrichment OR: 0.33 [p<0.0001]), implying it might suppress Olig2 expression. Motif 18 contained a Foxp1 binding site (**Fig. 8SE**), with 40.9% of Olig2+ neurogenic RPCs co-expressing Foxp1 (enrichment OR: 0.81 [p<0.0001]), as shown in **Fig. 8SG**. Additionally, binding sites for Mybl1 and Otx2 were identified in Motifs 2 and 12, respectively (**Fig. 8SF**); scRNA-seq data (**Fig. 8G**) indicate that these TFs may also contribute to the regulation of Olig2 expression via Olig2-NR1. Taken together, and considering the alignment of motifs with d-MPRA peaks and troughs as well as the quantified co-expression data from **Figs. 8SG** and **8G**, these results suggest that Sox4, Sox11, Dlx2, and Isl1 may predominantly function to repress Olig2 expression. Lhx2, Foxp1, Mybl1, and Otx2 are likely to act as activators through the Olig2-NR1 CRM.

The *de novo* motif discovery analysis of Olig2-NR3 identified 19 motifs (**Fig. 8SH**), several of which aligned with peaks or troughs in the d-MPRA plot. Among these, four motifs containing known TF binding sites active in the developing retina were associated with troughs, suggesting potential enhancer activity. Motif 13 matched a binding site for Bhlhb5 (encoded by *Bhlhe22*) (**Fig. 8SI**), a TF involved in retinal interneuron subtype specification (Feng *et al.*, 2006, Huang *et al.*, 2014); scRNA-seq co-expression data (**Fig. 8SL**) revealed that among Olig2+ RPCs, 21.6% co-expressed Bhlhb5 (enrichment OR: 3.5 [p<0.0001]). Motifs 3 and 5 contained binding sites for Ngn2 (**Fig. 8SJ**), a TF expressed in neurogenic RPCs during both early and late retinal development (Hufnagel *et al.*, 2010, Kowalchuk *et al.*, 2018, Ma & Wang, 2006); 81.4% of Olig2-expressing RPCs co-expressed Ngn2 (**Fig. 8SL**) (enrichment OR: 15.4 [p<0.0001]). Motif 15 matched a binding site for Lhx9 (**Fig. 8SK**), a TF expressed in early retinal development that is necessary for interneuron subtype specification (Balasubramanian *et al.*, 2014, Balasubramanian *et al.*, 2018). scRNA-seq analysis (**Fig. 8SL**) established that 7.7% of RPCs expressing Olig2 co-expressed Lhx9 (enrichment OR: 3.3 [p<0.0001]). The combined scRNA-seq analysis, d-MPRA, and motif discovery analysis confirmed that there are likely Bhlhb5, Ngn2, and Lhx9 binding sites in relevant regions of Olig2-NR3, and that they exhibit some degree of co-expression with Olig2, supporting the hypothesis that these TFs may regulate Olig2 expression via the Olig2-NR3 CRM.

The d-MPRA and motif analyses reveal a complex transcriptional network potentially regulating Olig2 expression, with some of the same TFs as candidate regulators across Olig2-

NR1, NR2, and NR3 CRMs. Olig2-NR2 emerged as potentially the most important regulatory hub, where motif discovery, scRNA-seq enrichment, and CUT&RUN validation confirmed direct binding of Mybl1, Pax6, and Foxn4. The d-MPRA approach provided a robust, high-resolution method for nominating functionally relevant TF binding sites, with motif-associated peaks and troughs aligning with known retinal regulators. The identification of additional candidates in Olig2-NR1 and NR3 provides candidates to expand our understanding of the gene regulatory network governing Olig2 expression, setting the stage for future *in vivo* studies to dissect their functional roles in retinal development.

LS-MPRAs for Neurogenin-2 in the developing mouse retina

To further test the LS-MPRA in identifying CRMs regulating transiently expressed genes of regulatory importance in the retina, *Ngn2* was analyzed. Ngn2, a proneural bHLH TF, is expressed in a subset of RPCs, those that will produce at least one postmitotic cell (Hufnagel *et al.*, 2010). Though known regulatory regions for Ngn2 have been elucidated in the ventral neural tube, where it also is expressed, their activities in the developing retina were unknown (Henke *et al.*, 2009, Nakazaki *et al.*, 2008, Scardigli *et al.*, 2003, Scardigli *et al.*, 2001, Simmons *et al.*, 2001). The Ngn2 LS-MPRA library (library characteristics in Table S3) was delivered to the E14 mouse retina and processed through the LS-MPRA pipeline, as described for Olig2. The aligned barcode enrichment plot revealed distinct candidates for CRMs (**Fig. 9A**). Among these, Ngn2-CRM3 was highly conserved across vertebrate and placental mammal species and corresponded to an open chromatin region located -136 bp to +150 bp relative to the *Ngn2* TSS. It also is located in a 4.4kb fragment with regulatory activity in the embryonic mouse spinal cord (Simmons *et al.*, 2001). To investigate the functionality of Ngn2-CRM3 and three additional CRM candidates identified in the LS-MPRA plot (Ngn2-CRM1, CRM2, and CRM4), each fragment was cloned into a plasmid containing a TATAA minimal promoter and EGFP reporter. These constructs were electroporated into E14 retinas and incubated *ex vivo* for 24 hours prior to analysis.

FISH for *Ngn2* and *GFP* RNA, alongside detection of intrinsic GFP fluorescence, in transverse retinal sections (**Fig. 9B**), demonstrated that Ngn2-CRM2 and Ngn2-CRM3 fragments consistently drove GFP expression in Ngn2+ cells. Co-localization analysis revealed that a substantial majority of *Ngn2* RNA+ electroporated cells expressed *GFP* RNA and/or protein when GFP expression was driven by these two CRMs (**Fig. 9C**, left column; Table S7). Approximately 57% of *Ngn2* RNA+ cells co-expressed *GFP* RNA when driven by Ngn2-CRM1, suggesting that this fragment may also function as a CRM, albeit less specifically for Ngn2. In contrast, GFP expression driven by Ngn2-CRM4 was sparse, and even fewer cells co-expressed *Ngn2* RNA, indicating that the LS-MPRA peak associated with this region does not correspond to a functional Ngn2 CRM in these conditions.

The proportion of *GFP* RNA+ cells co-expressing *Ngn2* RNA when GFP expression was driven by Ngn2-CRM2 or CRM3 (approximately 21% and 38%, respectively; **Fig. 9C**, middle-left column; Table S7) was lower compared to the corresponding co-expression analysis for Olig2 CRMs (**Fig. 6**). Similar to Olig2 CRMs, however, the proportion of *GFP* RNA+ cells driven by any Ngn2-CRM candidate region was consistently greater than that observed when the analysis was restricted to GFP protein+ cells (**Fig. 9C**, middle-right column; Table S7). These findings suggest that the rapid degradation of transient Ngn2 protein (~30mins half-life,

(McDowell *et al.*, 2014, Vosper *et al.*, 2007)) and, likely, *Ngn2* transcript, limits the overlap between Ngn2 and GFP expression.

To address this limitation, the *ex vivo* incubation period was reduced from 24 to 16 hours and focused on Ngn2-CRM3, the most robust CRM candidate. Shortening the incubation period resulted in an increase in the proportion of *GFP* RNA+ cells co-expressing *Ngn2* RNA (38% vs. 49%; **Fig. 9C,D**, right column; Table S7). Further evidence for this is provided by the concurrent decrease in the proportion of *GFP* RNA+ cells within the population of *Ngn2* RNA-negative cells when the incubation period was shortened (69% vs. 39%; **Fig. 9C,D**, right column; Table S7). This improvement supports the hypothesis that Ngn2's transient expression window and rapid turnover obscured co-expression of *GFP* and *Ngn2* RNA.

LS-MPRAs in chick retina and spinal cord

To determine if LS-MPRAs can be used to identify CRMs across species and tissues, regulatory elements controlling chick OLIG2 (cOLIG2) expression were carried out. Expression in the chick embryonic day 5 (E5) retina, a developmental stage equivalent to the E14 mouse retina, as well as in the chick spinal cord at two time points: E2 and E4, were examined with LS-MPRA. Olig2 is expressed in spinal cord progenitor cells that give rise to motor neurons and oligodendrocytes (Lu *et al.*, 2000, Zhou *et al.*, 2000). Electroporating the cOLIG2 LS-MPRA at E2 should capture the transcriptional activity of motor neuron progenitor cells (Hollyday & Hamburger, 1977), while delivery at E4 should capture the activity within oligodendrocyte precursor cells (Soula *et al.*, 2001). The cOLIG2 LS-MPRA library (library characteristics in Table S3) was electroporated into E5 chick retina explants and incubated *ex vivo* for 24 hours or electroporated into the E2 or E4 spinal cord and incubated *in ovo* for 24 hours or 48 hours, followed by LS-MPRA analysis.

Barcode enrichment plots from these experiments, aligned to the galGal6 chick reference genome, revealed distinct candidate CRM regions in both spinal cord and retina (**Fig. 10A**). One region, spanning -36.729kb to -36.428kb relative to the *cOLIG2* TSS, is highly conserved across vertebrates and orthologous to the Olig2-NR1 CRM identified in the mouse retina (97.3% sequence conservation shared across a 225bp region). Interestingly, this CRM candidate (cOLIG2-CRM1) was active in RPCs and in the E4 spinal cord but showed no detectable activity in electroporated E2 spinal cord. In addition to CRM1, two proximal CRM candidates—CRM2 (-264bp to -53bp) and CRM3 (+8.948kb to +9.036kb)—were identified in chick and assessed for their functional relevance to cOLIG2 expression.

To determine whether cOLIG2-CRM1, CRM2, and CRM3 function as CRMs, each fragment was cloned into a plasmid containing the *cOLIG2* minimal promoter and an EGFP reporter. These constructs were electroporated into E5 chick retinas and incubated *ex vivo* for 24 hours prior to analysis. FISH for *cOLIG2* and *GFP* RNA, alongside intrinsic GFP protein expression in transverse retinal sections (**Fig. 10B**), demonstrated that cOLIG2-CRM1 and cOLIG2-CRM2 consistently drove GFP expression in cOLIG2+ cells. Co-localization analysis revealed that the majority of electroporated *cOLIG2* RNA+ cells expressed *GFP* RNA and/or protein when GFP expression was driven by these two CRMs (**Fig. 10C**, left column; Table S8). In contrast, GFP expression driven by cOLIG2-CRM3 was nearly absent, indicating that the LS-MPRA peak associated with this region does not correspond to a functional cOLIG2 CRM in these conditions. Notably, the CRM3 peak overlaps with an AscI recognition site, a sequence rarely found in vertebrate genomes, which was used in the LS-MPRA design to facilitate

barcode–fragment association (**Fig. 1C**). This likely led to an under-representation of this region in the association library, thereby generating a false positive due to normalization using the association library flanking the AscI site in the BAC.

The proportion of *GFP* RNA+ cells co-expressing *cOLIG2* RNA when GFP was driven by cOLIG2-CRM1 or CRM2 (**Fig. 10C**, middle-left column; Table S8) was nearly identical to the proportion of GFP protein+ cells (**Fig. 10C**, middle-right column; Table S8). This suggests a more synchronized developmental window of cOLIG2 RNA and protein expression in chick compared to mouse (**Fig. 6A**). However, as observed in the mouse retina, a high proportion of cOLIG2-electroporated cells expressed *GFP* RNA (**Fig. 10C**, right column; Table S8), underscoring the challenges of detecting CRMs for transiently expressed transcription factors.

To further assess CRM activity in spinal cord progenitor cells, the cOLIG2-CRM constructs were electroporated into the ventral horn of E2 chick spinal cords (**Fig. 10SA**) and incubated *in ovo* for 24 hours. FISH for *cOLIG2* and *GFP* RNA in transverse spinal cord sections (**Fig. 10SB**) revealed that, similar to the chick retina, cOLIG2-CRM1 and cOLIG2-CRM2 drove *GFP* RNA expression in cOLIG2+ cells. However, both regions also exhibited GFP expression in cOLIG2- cells, suggesting either that their CRM activity is not restricted to cOLIG2-expressing progenitors in the spinal cord, or that low levels of *cOLIG2* RNA are undetectable in some GFP+ cells. No GFP expression was observed from cOLIG2-CRM3, further supporting the conclusion that this fragment does not function as a cOLIG2 CRM.

These findings highlight the ability of LS-MPRAs to identify orthologous CRMs that may regulate gene expression across species and developmental contexts. The conservation of cOLIG2-CRM1 with the mouse Olig2-NR1 CRM suggests a shared regulatory mechanism for Olig2 in vertebrate retinal and oligodendrocyte precursor cells, while the species- and tissue-specific activities of other CRMs underscore the complexity of gene regulation across development and across species.

Olig2 CRMs active in embryonic RPCs are active in postnatal RPCs that produce rod photoreceptors.

Thus far, we have primarily focused on the regulatory elements controlling Olig2 expression in RPCs destined to produce cones and horizontal cells. Later in development, after all cone and horizontal cells have been generated, postnatal neurogenic RPCs express Olig2 and produce primarily rod photoreceptors (Hafler *et al.*, 2012). An interesting question concerns whether these two distinct Olig2+ RPC populations share the same regulatory mechanisms governing Olig2 expression. To address this, we electroporated plasmids containing Olig2-NR1, NR2, NR3, or all three CRMs, into P0 retinas and incubated them *in vivo* for 24 hours before analysis.

Immunolabeling for GFP and Olig2 in transverse P1 retinal sections (**Fig. 11A**) and co-localization analysis revealed that the vast majority of Olig2+ electroporated cells expressed GFP when driven by NR1, NR2, NR3, or the combined NR1-3 composite (**Fig. 11B**, left column; Table S9). These findings indicate that NR1, NR2, and NR3 function as CRMs in RPCs that primarily produce rods in the postnatal retina. Notably, at this postnatal stage, most GFP+ electroporated cells also expressed Olig2 protein (**Fig. 11B**, middle column; Table S9), suggesting that the temporal activation of these CRMs is more closely aligned with Olig2 expression compared to their earlier activity in embryonic RPCs.

Since the majority of RPCs after P0 express Olig2, only a small number of Olig2-electroporated cells were present in the analysis. Despite their limited representation, most of these cells still exhibited GFP expression (**Fig. 11B,** right column; Table S9). Similar to the embryonic retina, this could reflect a temporal mismatch in the co-expression of Olig2 and GFP or indicate a subset of Olig2- cells with CRM activity.

Overall, these findings suggest that the same regulatory elements govern Olig2 expression in embryonic RPCs and the neonatal RPCs, as NR1, NR2, and NR3 serve as CRMs in both populations. The more synchronized co-expression of Olig2 and GFP in postnatal RPCs further implies that Olig2 regulation in late RPCs is more tightly coupled to its downstream gene expression programs compared to its earlier, less synchronous expression in early RPCs. This may be a reflection of slower developmental processes, as at least the cell cycle is longer in the later stages of retinal development (Alexiades & Cepko, 1996, Young, 1985).

DISCUSSION

In this study, we introduce novel LS-MPRA and d-MPRA approaches to search the *cis*-regulatory landscape of key developmental genes. By leveraging BAC-based libraries to survey large genomic regions and employing a degenerate MPRA strategy for nucleotide-resolution mapping, these methods overcome some of the limitations inherent to synthetic MPRAs. This approach enables the unbiased identification of candidate CRMs while precisely delineating potential TF binding sites, thereby nominating both activators and repressors that regulate expression of a gene. These methods also offer a rapid and simple route to identify CRMs that can be deployed in applications where driving gene expression in a specific context is required. The scale, expense, and relatively simple molecular methods enable CRM discovery by any laboratory with basic molecular biology skills.

LS-MPRA for stably expressed genes

The LS-MPRA was benchmarked using genes with known CRMs for stably expressed, cell type-specific genes. The experiments were carried out *in vivo* or in intact retinal explants, for discovery of CRMs relevant to authentic gene regulation in specific cell types. In postnatal retinas, CRMs were identified for the Rho PPR as well as some of the known CRMs for Grm6 and Vsx2. Interestingly, while the Rho LS-MPRA consistently detected a clear CRM peak at the PPR in both *in vivo* and *ex vivo* conditions, the previously identified RER and CBR Rho CRMs were seen only in *ex vivo* retinas. Of note, deletions of RER and CBR from the mouse genome showed that these two CRMs are dispensable for Rho expression, while the PPR is required (Sun *et al.*, 2023). The LS-MPRA in *ex vivo* retinas displayed a smaller signal to noise ratio around the *Rho* locus, particularly for the RER and CBR regions, but not around other loci on this BAC, perhaps reflecting differences in the requirements for a specific tissue environment or time course for proper *Rho* expression. Another requirement for RER and CBR activity might be the use of the Rho PPR. Both the RER and CBR were shown to enhance expression in constructs that used the Rho promoter (Corbo *et al.*, 2010), but neither had been tested using a heterologous promoter, as was used here. In the Vsx2 LS-MPRA, 2 of the 3 known CRMs were readily identified, with those 2 CRMs located quite some distance from the TSS, at -37 and -17 kb. It is unclear why the previously identified, promoter proximal CRM was not captured. One possible explanation is that the relatively short fragment lengths used to construct the libraries may not encompass the broader genomic context required for activation of this proximal CRM. Another potential explanation is again the choice of the promoter, as the Vsx2 promoter was used to identify the promoter proximal CRM in the previous study. The LS-MPRA for two other bipolar cell genes, Grm6 and Cabp5, also showed some positive and some negative results. Grm6 is expressed in the majority of retinal bipolar cells, and our previously described CRM for this gene, at -8kb, was identified by the LS-MPRA in both *ex vivo* and *in vivo* conditions. In contrast, the LS-MPRA failed to capture the known Cabp5 enhancer. It is not clear why this CRM was not identified here. Deeper sequencing of the cDNA libraries and/or using only a single BAC library for Cabp5, rather than the multiplexed format with 4 BACs used here, likely would increase the sensitivity. Sensitivity also should be increased by isolating electroporated cells of interest and/or pharmacologically or genetically increasing gene expression, as we did for Olig2. Finally, the choice of promoter may again play a role as the SV40 promoter was used in the earlier study for identification of the Cabp5 CRM.

LS-MPRA for transiently expressed genes

A focus of our laboratory is the mechanisms of cell fate determination in the retina. Our early study of RNA expression in RPCs showed that some TFs were expressed in subsets of RPCs, at one time and across the period of neurogenesis (Trimarchi *et al.*, 2008). We are interested in whether heterogeneity in RPC gene expression accounts for differences in the types of cells produced. Olig2 was identified as expressed in subsets of RPCs. Using a retroviral lineage tracing method to mark clones derived from Olig2 RPCs, we found that they divide only once or twice, and produce a limited repertoire of cell types: cones and horizontal cells in the embryonic period and rods and amacrine cells in the postnatal period. Interestingly, intermingled with the embryonic Olig2+ RPCs are Olig- RPCs, which produce RGCs, the output neurons of the retina. To address how these Olig2+ RPCs might differ from Olig2- RPCs, our goal is to leverage Olig2 regulation. We thus developed the MPRA methods to identify candidates for its regulation, and to see if these regulators might vary over time, in correlation with the different daughter cell types produced at different times.

The LS-MPRA for Olig2 did indeed identify CRMs that lead to potential regulatory sites as well as their cognate TFs. However, it was difficult to validate the specificity of these CRMs, due to the short half-life of endogenous Olig2 RNA and protein. Nonetheless, when tested as single or combined CRMs in individual plasmid constructs, there was activity in a high proportion of Olig2+ cells. CRM activity in Olig2- cells may reflect a mix of cell states, such as those that have recently downregulated Olig2 but retain GFP, RPCs initiating CRM-driven GFP expression prior to detectable *Olig2* levels, or cells in which the CRM functions independently of Olig2 expression. In addition, several technical and biological considerations may contribute to the apparent disconnect between reporter activity and endogenous Olig2 or Ngn2 expression. Introducing putative CRMs on plasmids removes them from their native genomic context, which may bypass normal chromatin accessibility constraints or local repressive influences and allow activity in cells where the endogenous gene is not expressed. These CRMs may also regulate genes other than Olig2 or Ngn2, reflecting broader or context-dependent roles. Finally, both Olig2 and Ngn2 are likely regulated by many more regulatory elements than the few tested here, so their endogenous expression may not depend solely on these specific CRMs. Despite GFP expression in Olig2- cells, several other lines of evidence increase confidence that Olig2-NR1, NR2, and NR3 are excellent candidates for specific Olig2 regulation. First, in the LS-MPRA, the same CRMs were found across 3 replicates, even though the signal to noise near the Olig2 locus was modest. The modest ratio is likely due to the fact that a modest or small percentage of RPCs express Olig2, reported to be ~14% in a previous study, (Brzezinski *et al.*, 2011), or 2.3% in a more recent study (Clark *et al.*, 2019). Additionally, and perhaps most importantly, it is expressed only briefly. To boost the signal, to potentially gain confidence in the candidate CRMs identified in the LS-MPRA, we were able to implement a drug manipulation. Notch inhibition greatly increases the production of cones (Jadhav *et al.*, 2006, Yaron *et al.*, 2006), and here we show that this same inhibition leads to greater Olig2 expression, with a peak at 12 hours post inhibition. Importantly, the activity of Olig2-NR1, NR2, and NR3 was upregulated by Notch inhibition with the same magnitude and kinetics as seen for the endogenous Olig2 locus. This experiment shows that the LS-MPRA can be used to not only nominate CRMs for a gene, but to nominate CRMs that respond to perturbation, which might be particularly useful when the experiment is run in the full library format (i.e. all BAC fragments are assayed for a response). Additional evidence that Olig2-NR1, NR2, and NR3 are valid came from the d-MPRA and the follow-on experiments. The d-MPRA showed some of the same potential TF binding sites in

more than one CRM, and several of these TFs have been shown to be important in retinal development, including TFs that play a role in cone and horizontal cell development, e.g. Otx2. In keeping with this, scRNAseq data show significant co-expression of Olig2 with the predicted TFs. Finally, CUT&RUN, using retinal tissue, showed binding of the suggested TFs to the CRMs. These data collectively provide support for the legitimacy of Olig2-NR1, NR2, and NR3 as key regulatory regions.

The binding of Mybl1 to Olig2-NR2 and potentially to Olig2-NR1, suggests that it plays a role in cone and/or horizontal cell development, likely as an activator of Olig2 expression. Its role in cone development was suggested previously by a study which tracked RNA expression in cultures induced to produce cones (Kaufman *et al.*, 2019). In contrast, Pax6—a master regulator essential for maintaining RPC multipotency and guiding cell fate decisions—has been shown to function as both an activator and a repressor (Cvekl & Callaerts, 2017, Farhy *et al.*, 2013, Marquardt *et al.*, 2001, Oron-Karni *et al.*, 2008, Remez *et al.*, 2017); its binding to Olig2-NR2 may keep Olig2 off in multipotent RPCs, and/or keep Olig2 off in RPCs that produce RGCs. Meanwhile, Foxn4, which is critical for the specification of amacrine and horizontal cells (Li *et al.*, 2004), may modulate Olig2 expression for control of the ratio of cone to horizontal cell fates. The overlapping motifs for Pax6 and Foxn4 in Olig2-NR2 may represent a region that balances activation and repression for modulation of early cell fate decisions.

Our results also reveal that different CRMs may be differentially engaged during retinal development. For instance, while Olig2-NR1 appears to integrate inputs from TFs such as Sox4, Sox11, Lhx2, Foxp1, Mybl1, and Otx2, Olig2-NR3 harbors binding sites for TFs including Bhlhb5, Ngn2, and Lhx9. As Sox4 and Sox11 binding sites might represent repressor sites, it is curious that they are co-expressed in 74% and 89% of Olig2+ cells. As they, as well as Lhx2 and Dlx2, play a role in RGC development, these expression patterns and roles in Olig2 regulation might represent a dynamic and complex gene regulatory network governing the production of the early born cell types. Consistent with this idea, and with the role of Bhlhb5 in later-born cell types, its binding site within the Olig2-NR3 may be engaged later in retinal development, considering a subset of bipolar cells exhibit a history of Olig2 expression (Hafler *et al.*, 2012), and some mature bipolar cells maintain Olig2 expression. This nuanced and complex regulation underscores the broader utility of LS-MPRA and d-MPRA for discerning CRMs and TFs that are either cell type-specific or shared across distinct developmental competence states. Future studies employing targeted perturbations, such as CRISPR/Cas9-mediated disruption of specific TF binding sites, will be essential to validate these CRMs and establish the roles that they play in gene regulation.

Considerations for use of LS-MPRA and d-MPRA.

There are several issues to consider when choosing a method for CRM identification. Data describing open/active chromatin, conserved genomic sequences, and RNA expression, are increasingly comprehensive, but do not cover all cell types and non-model organisms. However, with the advent of single cell multi-omics, one can anticipate that these gaps will eventually be filled over the period of the next few years. When such data are available, and predict very few CRMs, one can simply PCR a potential CRM from genomic DNA, and test individually. In other cases, these types of data nominate a high number of potential CRMs. Producing many individual PCR products, cloning them into expression vectors, sequencing, introducing into cells, and assaying the results from single constructs, are much more time-consuming and expensive than LS-MPRAs. For example, we have identified potential CRMs for Otx2. Using

predictions from open chromatin, eRNAs, and DNA conservation, >20 CRMs were nominated (Chan *et al.*, 2020, Emerson & Cepko, 2011, Lonfat *et al.*, 2021). Assessing each potential CRM and its relevant TF binding sites spanned more than several years. In addition to this level of effort, testing each potential CRM in isolation precludes a quick recognition of the relative strength of each CRM. Speed and expense also can be addressed using LS-MPRA by multiplexing libraries from several genes. Finally, when one needs a relatively small CRM, e.g. for expression in a viral vector, one can choose the fragment size during the BAC library preparation step. CRMs predicted by open chromatin typically do not provide this option.

One critical requirement for identification of CRMs using any method is introduction of constructs into cells. Tissue culture cells offer easy access. However, they often do not recapitulate the endogenous *in vivo* context and are often a single, irrelevant cell type. Even when multiple cell types are present, as in organoids, the correct environment may not be present. This may be exemplified by the difference between CRM identification for the *Rho* gene in the *in vivo* versus *ex vivo* retinal explants. The LS-MPRA from *ex vivo* retinas showed noisier CRM signals, and failed to show as good a signal-to-noise ratio for the required Rho CRM, the PPR. This did not seem to hold true for the other *in vivo* versus *ex vivo* comparisons for Vsx2 and Grm6. If one can electroporate *in vivo*, as we do here, the LS-MPRA likely will provide the most reliable results. If electroporation into the cell type of interest is not possible, one can introduce libraries using viral vectors, as was done with an AAV library for identification of CRMs for specific cell types of the central nervous system (Hrvatin *et al.*, 2019). Selected genomic regions were chosen bioinformatically, which may introduce a bias, and each predicted element was individually generated by PCR, which is time-consuming and limits library size. Bias may also be introduced by the choice of the promoter or other elements in the expression construct. We chose a simple TATAA promoter to reduce background activity, but as genomic sequences can influence each other, we may have missed some CRMs due to this choice. In addition, while the BAC-based approach enables the survey of large genomic regions, it cannot capture all potential regulatory inputs, and it remains possible that some distal regulatory sequences lie outside of the BACs used here.

When using a CRM as a reagent to gain genetic access to specific cell types, further analysis of its architecture is often unnecessary. However, for those aiming to understand the regulation of a gene of interest, the d-MPRA offers a powerful approach to rapidly pinpoint individual nucleotides that positively or negatively influence CRM activity. Traditional methods, such as introducing single-base mutations or deletions and testing each construct individually, are time-consuming and often yield qualitative, rather than quantitative, results. Repressor sites, in particular, are rarely identified this way. With the growing availability of TF binding site databases, d-MPRA can efficiently highlight key nucleotides and nominate candidate TFs involved in CRM regulation. When multiple CRMs are available, comparing predicted TF binding sites across them can further strengthen TF candidacy. Examining RNA expression data provides additional support. To validate these predictions, TF binding assays performed *in vivo* or *in vitro* can confirm binding to the endogenous locus. It would also be valuable to integrate LS-MPRA and d-MPRA with analyses of DNA methylation, particularly in regions near genes of interest across stages of retinal development, building on prior studies of methylation in adult tissues associated with disease (Advani *et al.*, 2024). Importantly, LS-MPRA and d-MPRA methods are adaptable across species, as demonstrated here in both chick and mouse, and can be applied to different regions of the developing embryo.

METHODS

RESOURCE AVAILABILITY

Raw and processed image data are available upon request. All original code and unprocessed sequencing files are available on the Harvard Dataverse (DOI: doi:10.7910/DVN/TW0ZQL) (Tulloch, 2025). All processed LS-MPRA genome tracks are available to view on a Track Hub in the UCSC Genome Browser (https://github.com/cattapre/ALAS00). Primer sequences are available in Table S1. Any additional information is available from the lead contact upon request. Plasmids that are required for these methods will be deposited to Addgene.

EXPERIMENTAL MODEL AND SUBJECT DETAILS

All experimental procedures were preapproved by the Harvard Medical Area Standing Committee on Animals (HMA IACUC). Timed and untimed pregnant CD-1 mice used for sequencing and histology were purchased from Charles River Laboratories and were housed in a climate-controlled pathogen free facility. Mouse tissues were collected for sequencing experiments at E14, P3, or P10 and for histological experiments at E14 or P1 as noted within the text. Chick tissues were collected for sequencing experiments at E3, E5, and E6 and for histological experiments at E3 and E5, as noted within the text.

METHOD DETAILS

Electroporation and Culture

For plasmid DNA injections, glass needles were created by pulling Wiretrol II capillaries (Drummond Scientific Company, cat. #5-000-2005) using a needle puller (Sutter Instrument, Model P-97). The glass needles were beveled on two edges with a microgrinder (Narishige, cat. #EG-401). Plasmid DNA with individual or composite enhancers as well as d-MPRA libraries and most LS-MPRA libraries were concentrated to 2.0µg/µl along with control plasmids containing either bpCAG-mCherry or CAG-BFP concentrated to 0.5µg/µl. When pooling libraries for multiplexing, LS-MPRAs for Grm6, Vsx2, and Cabp5 were concentrated to 1µg/µl and the Rho LS-MPRA library was concentrated to 50ng/µl, with the bpCAG-mCherry control plasmid concentrated to 0.25µg/µl.

Ex vivo electroporation: perinatal mouse and chick eyes were enucleated from animals and placed in fresh 1×PBS. Using a beveled glass needle, plasmid DNA (prepared in 1×PBS supplemented with 0.01% Fast Green (Millipore Sigma cat. #F7252) was injected into the subretinal space. Injected eyes were either transferred to a modified electroporation chamber (Montana *et al.*, 2011) or placed between platinum disk electrode tweezers (Bulldog Bio, cat. #CUY650P2). All retinas were electroporated with five 50 ms pulses at 40 V delivered at 1-second intervals using a NEPA21 type II Nepagene electroporator; electric currents were applied in both directions between electrodes to maximize electroporation efficiency.

Following electroporation, E14 mouse and E5 chick retinas were removed from surrounding tissues and placed in a culture medium consisting of a 1:1 mixture of DMEM:F12, supplemented with 10% FBS, 200 mM L-glutamine (Sigma-Aldrich, cat. #G3126), and 100 U/mL penicillin with 100mg/mL streptomycin (Invitrogen/Gibco, cat. #15140-122) in microcentrifuge tubes, and cultured on a nutator at 37°C for 16-28 hrs, depending on the experiment. P3 mouse retinas were removed from surrounding tissues and placed directly onto a nucleopore track-etched polycarbonate membrane (Watman, cat. #110410) in a 12-well tissue culture dish, floating on 2ml explant media consisting of 50% Minimum Essential Medium

(Millipore Sigma, cat. #51412C)(v/v), 25% HBSS (Thermo Fisher Scientific, cat. #14-025-092) (v/v), 25% heat-inactivated horse serum (Thermo Fisher Scientific, cat. #26050-088), 200mM L-glutamine (Sigma-Aldrich, cat. #G3126), 5.75mg/mL glucose, 25mM HEPES (Invitrogen/Gibco, cat. #15630-080), and 100 U/mL penicillin with 100mg/mL streptomycin (Invitrogen/Gibco, cat. #15140-122). The P3 retinas were covered with 20µl of explant media, and incubated at 37ºC, 5% CO_2 for 7 days; each day, 1ml of media was replaced with new media and 20µl of explant media was reapplied on the retina to keep moist.

In vivo electroporation: P0 and P3 mouse pups were anesthetized by cryoanesthesia on ice and injected subcutaneously with 0.012mg/ml buprenorphine (approximately 20µl; PAR Pharma). A small skin incision was made by a 30-gauge needle across the eyelid and the eye was exposed. A small drop of 0.5% proparacaine hydrochloride (Bausch & Lomb, cat. #24208-730-06) was placed onto the surface of the eye. A beveled glass needle containing plasmid DNA (prepared in 1×PBS supplemented with 0.01% Fast Green, Millipore Sigma cat. #F7252) was inserted through the sclera into the subretinal space. Plasmid DNA was delivered using a Femtojet Express pressure injector (Eppendorf, cat. #920010521) set at 330 Pa for 3 seconds. The eyelids were then closed with a cotton applicator. Tweezer-type electrodes (Harvard Apparatus, BTX, model 520, 7 mm diameter, cat. #450165) were placed with the positive end slightly above the injected eyelid and the negative electrode on the contralateral side of the head. An electric field was applied using an electroporator (BEX, cat. #CUY21EDIT), delivering five 50 ms pulses at 80 V with 1-second intervals. Eyelids were dried with a cotton applicator to ensure eyelid closure.

In ovo electroporation: Fertilized chick eggs were incubated at 37°C in a humidified chamber until they reached Hamburger and Hamilton (HH) stages 11-13 (E2) or stages 22-24 (E4). A small window was created in the eggshell, and a solution containing plasmid DNA was injected into the neural tube using a beveled glass needle. Platinum chopstick electrodes with 4mm tips (Bulldog Bio, cat. #CUY611P7-4) were positioned flanking the neural tube: at E2, electrodes were placed against the outer membrane to ensure targeted DNA delivery into the ventral neural tube. At E4, due to the natural 90º rotation of the neural tube, a small hole was made in the membrane to enable precise electrode placement on the lateral sides. Electroporation was performed using a NEPA21 Type II Nepagene electroporator with five 50 ms pulses at 25 V delivered at 1-second intervals. After electroporation, the eggs were resealed and incubated for 24–48 hours before tissue collection. Electroporation success was assessed by detecting fluorescence from control plasmids (bpCAG-mCherry or CAG-BFP).

To ensure sequencing replicates contained a sufficient representation of enriched barcodes at each age, pools of at least 8 mouse retinas for each E14 LS-MPRA and d-MPRA experiment, 3 mouse retinas for each P3 LS-MPRA experiment, 3 chick retinas or 1-2 chick spinal cords for each LS-MPRA experiment were used. When indicated and either coupled with *ex vivo* electroporation or *ex vivo* culture alone, the γ-secretase inhibitor LY411575 (MilliporeSigma, cat. #SML0506) was added to a final concentration of 1µM. A 10,000× stock was prepared at 10 mM in DMSO and stored at –20°C. Just prior to use, the 10 mM stock was diluted 1:10 in 1×PBS to yield a 1000× working solution; 1 µl of the working solution was added per 1 ml culture.

RNA Isolation

To isolate RNA for barcode sequencing or to quantify gene expression, up to 8 mouse retinas, 3 chick retinas, or 2 chick spinal cords were pooled and homogenized using 21-gauge needles in

250µl TRI Reagent (MilliporeSigma, cat. #T9424). Total RNA was isolated using the Zymo Directzol Microprep Kit (Zymo Research, cat. #R2061), omitting on-column DNase treatment. For LS-MPRA and d-MPRA library preparations, polyA RNA was subsequently enriched using the Dynabeads mRNA Purification Kit (Thermo Fisher Scientific, cat. #61006). The specific cDNA synthesis protocols for each experiment are detailed in following sections.

Retinal Cell Dissociation

Mouse retinas electroporated at E14 or P3 and cultured *ex vivo* were dissociated using papain digestion. For each sample, a papain mix was prepared by combining 315 µl HBSS, 35 µl 1M HEPES (pH 7), 20 µl 50 mM L-cysteine (freshly prepared), 0.4 µl 0.5 M EDTA (pH 8), 19.6 µl UltraPure Water, and 10 µL papain solution (Worthington Biochemical, cat. #LS003126), followed by incubation at 37°C for 15 mins to activate the enzyme. Retinas were incubated in 400 µL of activated papain mix at 37°C for 7 mins, then centrifuged at 600×g for 2.5 mins. The supernatant was removed, and cells were resuspended in 1 mL HBSS/FBS mix (10% FBS in HBSS), centrifuged again, and resuspended in 600 µL DMEM/BSA mix (4 mg/mL BSA in DMEM). Cells were gently triturated using a fire-polished Pasteur pipette or a P1000 low-retention pipette, centrifuged again at 600×g for 2.5 mins, and finally resuspended in 200–1000µl of the appropriate solution for downstream applications.

Fixed Tissue Preparation

Retinas electroporated *in vivo* were first dissected from surrounding tissues while retaining the lens in 1×PBS. Retinas in *ex vivo* culture were removed from culture media. Spinal cords *in ovo* were dissected from surrounding tissues in 1×PBS. All tissues were fixed in 4% paraformaldehyde in 1×PBS for 20 mins and rinsed three times in 1×PBS for 30 mins. Tissues were transferred to 30% sucrose in 1×PBS and gently agitated until fully infiltrated (approximately 30–60 mins). Retinas were equilibrated in a 1:1 mixture of 30% sucrose in 1×PBS and Tissue-Tek OCT (VWR, cat. #25608 930), and were then placed in cryomolds (Sakura Finetek, cat. #4565) in this medium and snap frozen on dry ice. Spinal cords were equilibrated in 100% Tissue-Tek OCT prior to snap freezing. Cryosections (20 µm thick) were air dried for 20 mins at 37ºC and stored at –80°C.

Fluorescent in situ Hybridization

For multiplexed HCR™ RNA-FISH, probe sets were manufactured by Molecular Instruments based on the sequences provided: *Olig2* (NM_016967.2), *Neurog2* (XM_030252394), *OLIG2* (NM_001031526.1), and *GFP* (d2eGFP sequence; Lot no. RTA210). Frozen sections on slides were rinsed two times for 5 mins in PBS, pre-hybridized in probe hybridization buffer (Molecular Instruments HCR™ Buffers [v3.0]) for 10 mins at 37ºC, and hybridized with 0.4 pmol of each probe set (Molecular Instruments HCR™ Probes [v3.0]) in hybridization buffer O/N at 37ºC. Excess probes were removed in serial 15 mins incubations at 37ºC in mixtures of 1:0, 3:1, 1:1, 1:3, and 0:1 of probe wash buffer (Molecular Instruments HCR™ Buffers [v3.0]) and 5× sodium chloride sodium citrate with 0.1% Tween-20 (SSCT) followed by a 5 min rinse at RT in 5×SSCT. Sections were then incubated in amplification buffer (Molecular Instruments HCR™ Buffers [v3.0]) for 30 mins at RT before incubating in a dark humidifying chamber with 6 pmol of h1 and 6pmol of h2 snap-cooled (heated at 95°C for 90s and incubated at RT for 30 mins in the dark) hairpins for each probe set in amplification buffer for 6–18hrs at RT. Alex546-

and Alexa647-labeled hairpins were used. Excess hairpins were removed in sequential rinses in 5×SSCT at RT for 5 mins, 2x30 mins, and 5 mins and proceeded to immunostaining.

Immunohistochemistry

New frozen sections on slides that were first washed two times for 5 mins in PBSTw (1×PBS with 0.1% Tween-20), or immediately following RNA-FISH, were blocked with 2.5% donkey serum (Jackson ImmunoResearch, cat. #017-000-121) in PBSTw for 1hr at RT. Tissues were incubated in primary antibodies O/N at 4ºC and with secondary antibodies for 1 hr at RT in blocking solution, rinsed three times with PBSTw between and after antibody incubations, and mounted using Fluoromount-G (SouthernBiotech, cat. # 0100-01). Mouse monoclonal antibodies raised against Olig2 (1:500, Millipore cat. #MABN50), chicken polyclonal antibodies raised against GFP (1:1000, Abcam, cat. #ab13970), and rabbit polyclonal antibodies raised against BFP (1:200, Abcam, cat. #ab286131) were used. Alexa405-, Alexa488-, and Alexa647-conjugated secondary antibodies (1:200; Jackson ImmunoResearch) raised in donkey against respective primary antibody species as well as DAPI (1:1000, Invitrogen cat. #D1306) were also used.

Microscopy

Samples were imaged with a Yokogawa CSU-W1 single disk (50mm pinhole size) spinning disk confocal unit attached to a motorized Nikon Ti inverted microscope equipped with a Nikon linear-encoded motorized stage with a Mad City Labs 500 mm range Nano-Drive Z piezo insert, an Andor Zyla 4.2 Plus sCMOS camera using a Nikon S Plan Fluor 40x/1.3 DIC H/N2 oil immersion objective lens. The final digital resolution of the image was 0.16 µm/pixel. Fluorescence from (405 nm, 488 nm, 550 nm, and 640 nm) was collected by illuminating the sample with directly modulated solid-state lasers 405 nm diode 100 mW (at the fiber tip) laser line, 488 nm diode 100 mW laser line, 561 nm DPSS 100 mW laser line and 640 nm diode 70 mW laser line in a Toptica iChrome MLE laser combiner, respectively. Signal from each channel was acquired sequentially with hard-coated Chroma ET455/50 nm, Chroma ET525/36 nm, Chroma ET605/52 nm, and Chroma ET705/72 nm emission filters in a filter wheel placed within the scan unit, for blue, green, red, and far-red channels, respectively. All images were captured using the 16-bit dual gain high dynamic range camera mode and no binning. Nikon Elements AR acquisition software was used to acquire the data. Z-stacks were acquired using Piezo Z-device, with the shutter closed during axial movement. Images were acquired by collecting all colors in a Z-step, then each Z-stack before XY-stage movement, with a 15% tile overlap for correct stitching. Data were saved as ND2 files.

Vector Design

<u>Barcoded Stagintbc7</u>: The parent vector, Stagint7, is a minimal pUC19-based construct containing a kanamycin resistance gene, an SV40 polyadenylation site, a multiple cloning site immediately upstream of a minimal TATAA promoter, an intron-containing EGFP open reading frame, and a rabbit β-globin polyadenylation sequence. This vector is based on the previously described Stagia3 vector used for retinal enhancer assays (Billings *et al.*, 2010). The parent vector was linearized between the EGFP ORF and polyadenylation sequence via an AscI (NEB, cat. #R0558) recognition sequence, inserting Illumina adapter sequences flanking a recreated AscI recognition sequence, a unique 8-bp library barcode tag for multiplexing (used only for Rho, Grm6, Vsx2, and Cabp5 libraries), and a 24-bp barcode using an Enhanced Gibson

Assembly reaction (Rabe & Cepko, 2020). Barcodes consisted of either twelve SW base repeats or four VHBD base repeats to prevent high GC content and homopolymer repeats as well as to provide sufficient barcode complexity. The barcoded Stagintbc7 vector used to create LS-MPRA libraries (Rabe, 2020) was generated by combining 100 ng of linearized parent vector with 25 nM of each primer pair (see Table S1) and, along with the pre-mixed Enhanced Gibson Assembly reaction, incubated at 50ºC for 1 hr. The assembled product was purified with a Zymo DNA Clean & Concentrator Kit (Zymo Research, cat. #D4013).

For the creation of the four Stagintbc7 multiplexed libraries, four unique DNA library tags were generated using the DNABarcodes R package (Buschmann, 2017) to ensure that all barcodes differed from one another by at least five bases while avoiding homopolymer repeats. The create.dnabarcodes function was used with a Hamming distance metric of 5, and additional filters were applied to exclude triplet repeats, ensure GC content balance, and prevent self-complementarity. The selected library barcode tags included: ATACAGGC, TGTGCAAG, CACGAAGA, and GTGAACCT.

Statadual_WPRE: This vector, used for d-MPRA library construction, is derived from Stagia3 but replaces the minimal TATAA promoter and intron-containing EGFP ORF of Stagint7 with a WPRE sequence.

Assembly of LS-MPRA Libraries

BAC Isolation and Preparation: BACs were first isolated from stab cultures (BACPAC Resources). Cultures were streaked onto chloramphenicol-treated LB agar plates and incubated overnight at 37°C. A single colony was picked and grown in LB media supplemented with chloramphenicol (12.5 µg/mL) in 5 ml overnight, followed by expansion to 500 ml. The culture was pelleted, and BAC DNA was extracted using a large construct DNA isolation kit with ATP (Qiagen, cat. #12462). DNA concentrations were determined using the Qubit dsDNA HS Assay Kit (ThermoFisher, cats. #Q32851 and # Q32856). For sequencing validation, samples were sent to Plasmidsaurus for large plasmid sequencing. BAC clones used in all experiments included RP23-219M6 (*Rho*), RP23-417M10 (*Grm6*), RP23-127O21 (*Vsx2*), RP24-125H22 (*Cabp5*), CH29-613 (*Olig2*), RP23-182M12 (*Ngn2*), and CH261-60J3 (*OLIG2*).

BAC Fragmentation and Adapter Ligation: BAC DNA (500 ng) was enzymatically digested, end-repaired, and dA-tailed using the NEBNext Ultra II FS DNA Module kit (NEB, cat. #E7810S) with a 20-min enzyme incubation. Digested DNA was purified using SPRIselect beads with a 1.2x left-side size selection ratio. Concentrations were determined using the Qubit dsDNA HS Assay Kit. Double-stranded adapters (Table S1) were annealed from complementary oligonucleotides and diluted to a molar concentration approximately 100-fold higher than fragments in 1×T4 DNA ligase buffer (NEB, cat. #B0202S). The 5' adapter sequence included an Illumina adapter sequence and a 25-bp homologous sequence for Gibson Assembly insertion into the Stagintbc7 vector, while the 3' adapter sequence included a 23-bp homologous sequence and an AscI recognition sequence. Adapters were ligated to fragments using the Blunt/TA Ligase Master Mix (NEB, cat. #M0367), adding a 1:1 mixture of ligase mix and 18 µl fragments with 2 µl adapters, incubating at RT for 1 hr. Adapter-ligated DNA was purified using the Zymo DNA Clean & Concentrator Kit and quantified using the Qubit dsDNA HS Assay Kit.

Adapter-ligated Fragment Amplification and Purification: Adapter-ligated fragments were amplified using NEBNext Ultra II Q5 Master Mix (NEB, cat. #M0544) in a 300 µl reaction with 0.5 µM primers (Table S1) complementary to the 5' and 3' adapter ends and at an annealing temperature of 64°C for 15 cycles. Amplified DNA was purified using the Zymo DNA Clean &

Concentrator Kit. To ensure proper fragment size selection, adapter-ligated fragments were resolved on a 1% agarose gel, and the desired size range (fragment plus ~90 bp of adapter sequence) was gel purified using Agarose Dissolving Buffer (Zymo Research, cat. #D4001-1-100) and the Zymo DNA Clean & Concentrator Kit.

Cloning into Barcoded Library: The Stagintbc7 barcoded library was linearized with PacI (NEB, cat. #R0547) and EcoRI-HF (NEB, cat. #R3101). The digested vector was purified via 0.75% agarose gel electrophoresis and gel extraction. An Enhanced Gibson Assembly was performed with 100 ng vector and a 10:1 molar insert:vector ratio at 50ºC for 1hr. The assembled product (Rabe, 2020) was purified with a Zymo DNA Clean & Concentrator Kit.

Library Transformation and Amplification

All barcoded libraries—Stagintbc7, LS-MPRA, and d-MPRA—were electroporated into DH10β electrocompetent cells in a pre-cooled 1 mm cuvette (BTX, cat. #45 0134) with the following parameters: 2 kV, 25 µF, and 200 Ω on a BioRad GenePulser II. Transformed cells were outgrown in 2 ml SOC media at 37°C for 2 hrs, and then grown in 3D culture by embedding bacterial transformations in 0.5% sodium alginate matrices with $CaCO_3$ and LB to reduce clonal bias inherent in 2D cultures. To prepare 3D cultures (Rabe, 2020), the transformed bacterial cells grown in SOC were mixed with 12.5 ml of 1% sodium alginate (mixed 1g/100ml LB O/N, then autoclaved) and LB to a volume of 20 ml. Then, 250µl of a $CaCO_3$ suspension (10 g in 100 ml diH_2O; Sigma Aldrich, 310034) and 1000× kanamycin (25 µL) were combined in 2.5 ml LB, mixed immediately before use, and added to the bacterial-alginate solution. Lastly, 41.7 µl of 37% HCl in 2.5 ml LB was added for a final volume of 25 ml, and the mixture was gently rocked for 5 minutes before being poured into a sterile 150 mm petri dish. Cultures were incubated at 37°C for 16–20 hours to allow gel formation and outgrowth.

Following incubation, 6.25 ml of 20× SSC + 40 mM EDTA solution (pH 8.0) was added to dissolve the 3D culture, and was gently rocked at RT for 15 min. Bacterial cells were pelleted (6,000×g, 15 min), washed with 25 ml LB, and centrifuged again. The pellet was resuspended in 300 ml LB containing 50 µg/ml kanamycin and 0.05 mg/ml alginate lyase (Sigma Aldrich, cat. #A1603) and incubated at 37°C with shaking (250 RPM) for 6–8 hrs. Cultures were then pelleted for plasmid preparation or storage at –20°C. Plasmids were extracted using a Plasmid Maxi kit (Qiagen, cat. #12163).

To estimate the complexity of transformed libraries, a serial dilution was performed after the transformation and prior to 3D culture. One microliter of the 2 ml culture in SOC was removed and subjected to three sequential dilutions (1:500, 1:5000, and 1:50,000) to represent 1/10,000th, 1/100,000th, and 1/1,000,000th of the total transformation, respectively. For dilution preparation, 1 µl of the culture was added to 499 µl SOC, mixed, and 50 µl of this dilution was transferred to 450 µl SOC, followed by an additional 1:10 dilution under the same conditions. 100 µl of each dilution was plated onto kanamycin-treated LB agar and incubated O/N at 37°C. The number of resulting colonies was used to estimate transformation complexity, with a quantifiable optimal range of 20–200 colonies per plate.

Assembly of d-MPRA Libraries

CRMs of interest were PCR-amplified from their respective BAC clones using primers designed to incorporate 20–30 bp overlapping sequences for Gibson Assembly into the Statadual_WPRE vector (Table S1). PCR reactions were performed using NEBNext Ultra II Q5 Master Mix under

standard conditions, and amplicons were gel-purified using the Zymo DNA Clean & Concentrator kit.

Mutagenesis was performed using the GeneMorph II Random Mutagenesis Kit (Agilent, cat. #200550), following the manufacturer's protocol with 100 pg of input DNA and MutF/R primers (Table S1), which amplify the entire CRM region and incorporated overlapping sequences. PCR products were gel-purified, and 100–200 ng of each mutagenized fragment was assembled into the EcoRI/PacI-linearized Statadual_WPRE vector via Enhanced Gibson Assembly at a 10:1 insert-to-vector molar ratio. The assembled libraries were electroporated into DH10β electrocompetent cells, expanded in 3D bacterial culture, and purified as previously described.

For intraplasmid duplication (IPD), 3 µg of purified intermediate plasmid libraries were digested with the nicking endonuclease Nt.BspQI (NEB, cat. #R0644) at 50°C for 1 hr, column-purified, and incubated with Bst 2.0 WarmStart Polymerase (8 units, NEB, cat. #M0538) in 1× Isothermal Amplification Buffer supplemented with 6 mM $MgSO_4$ and 200 µM dNTPs (GoldBio, cat. #D9001) in a 50 µl reaction at 65°C for 45 mins, followed by enzyme inactivation at 80°C for 20 mins. To reduce self-ligation, 2.5 units of Taq DNA polymerase (NEB, cat. #M0273) was added, and the reaction was incubated at 65°C for 20 mins for dA-tailing. The prominent linear band was gel-excised and purified.

The final d-MPRA insert (a minimal TATAA promoter and intron-containing EGFP ORF) was PCR-amplified from Stagint7 with primers designed to incorporate 20–30 bp overlapping sequences for Gibson Assembly into the linearized IPD product (Table S1), gel-purified, and assembled with 25 fmol of linearized, IPD-processed vector in an Enhanced Gibson Assembly reaction (Rabe, 2020). The completed d-MPRA libraries were electroporated into DH10β electrocompetent cells, expanded in 3D bacterial culture, and purified as previously described.

CUT&RUN

Experiments were performed using freshly dissociated E14 mouse retinas with the CUTANA™ ChIC/CUT&RUN Kit (EpiCypher, cat. #14-1048) according to the manufacturer's protocol. Mouse monoclonal antibodies raised against Pax6 (Developmental Studies Hybridoma Bank, cat. #AB_528427) and against Foxn4 (Santa Cruz Biotechnologies, cat. #sc-377166) as well as rabbit polyclonal antibodies raised against Mybl1 (Millipore-Sigma, cat. #HPA008791) were used, adding 500ng of the respective antibody to each sample during the antibody binding stage. Indexed libraries were prepared with the NEBNext UltraII DNA Library Prep Kit (NEB, cat. #E7103) and the NEBNext Multiplex Oligos for Illumina Dual Index Sets (NEB, cats. #E7600S or #E7780S). All experiments were validated following Next-Generation sequencing using the SNAP-CUTANA K-MetStat Panel of nucleosome spike-ins in control reactions and the manufacturer's protocol (Appendix 1.6; EpiCypher, cat. #14-1048).

Sequencing Library Preparation

<u>LS-MPRA Fragment–Barcode Association Libraries</u>: To excise the minimal promoter and GFP ORF, enabling BAC fragments to be positioned adjacent to their corresponding barcodes for sequencing, 2–3 µg of the LS-MPRA library was digested with AscI and resolved on a 1% agarose gel (Rabe, 2020). The fragment containing both the barcode and insert (~2.1 kb plus the fragment size) was excised and gel-purified. 500 ng of purified fragment was circularized in a 100 µl Quick Ligation reaction (NEB, cat. #M2200) at RT for 5 mins. The ligation product was

column-purified and treated with 50 µl exonuclease (Lucigen, cat. #E3101K) to remove residual linear fragments.

Following gel resolution, the smallest and brightest band was excised and gel-purified. Because the ligation product already contained Illumina read primer sequences, 50 ng of purified product was used as a template for index PCR with NEBNext Q5 Ultra II Master and NEBNext Multiplex Oligos for Illumina Dual Index Set for 15 cycles. PCR products were purified via two-sided SPRISelect bead purification (0.5x to 0.9x).

LS-MPRA Barcode Abundance Libraries: To assess barcode abundance in RNA, polyA RNA was reverse-transcribed using the Protoscript II Kit (NEB, cat. #E6560) and a reverse transcription primer at 1µM specific to all barcoded transcripts (bc7_cdnaR; Table S1). The resulting cDNA was purified using the Zymo Oligo Clean & Concentrator Kit (Zymo, cat. #D4060) and then amplified for 30 cycles using NEBNext Q5 Ultra II Master Mix with two primers: one that anneals to a region of the GFP ORF upstream of the intron and the other downstream of the barcode-flanking Illumina adapter sequences [bc7_cdnaF and bc7_cdnaR2 (Table S1), respectively], ensuring the intron-containing plasmid DNA was not included. The cDNA-derived amplicons (~356–364 bp) were gel-purified from a 1% agarose gel. Indexed barcode amplicons were generated with 50 ng purified product, NEBNext Q5 Ultra II Master Mix, and NEBNext Multiplex Oligos for Illumina Dual Index Set for 15 cycles, followed by two-sided purification using SPRISelect beads (0.95x-1.2x).

d-MPRA Libraries: Amplicons for d-MPRA mutagenesis analysis were generated from both plasmid libraries and RNA (Rabe, 2020). cDNA was synthesized from polyA RNA using the Protoscript II Kit and the reverse transcription primer at 1µM specific to all d-MPRA barcoded transcripts [bc7_cdnaR_WPRE, (Table S1)], purified with the Zymo Oligo Clean & Concentrator Kit, and amplified for 30 cycles using NEBNext Q5 Ultra II Master Mix with two primers: one that anneals to a region of the GFP ORF upstream of the intron and the other downstream of the barcode and upstream of the WPRE sequence [bc_cdnaF and MutR, respectively (Table S1)]. The resulting cDNA band (~290 bp plus the CRM size) was gel-purified. For plasmid d-MPRA libraries, the corresponding fragment was generated by digesting with BsrGI (NEB, cat. #R3575) and NdeI (NEB, cat. #R0111), which excises the CRM barcode and WPRE sequence, and gel purifying the product (~760 bp plus the CRM size).

For both plasmid library and RNA-derived amplicons, Illumina adapter sequences were added to each side of the mutated CRM sequence [dualmut_IllR1F or dualmut_IllR2F and dualmut_IllR2R primers (Table S1)]. These fragments, amplified from 50 ng template with NEBNext Q5 Ultra II Master Mix, were gel-purified and subjected to index PCR with NEBNext Multiplex Oligos for Illumina Dual Index Set for 15 cycles. PCR products were purified via two-sided SPRISelect bead purification (0.6x to 0.9x).

Illumina sequencing

All indexed LS-MPRA, d-MPRA, and CUT&RUN libraries were analyzed using an Agilent TapeStation High Sensitivity D1000 assay. Indexed samples were sequenced using 2×150 bp paired end reads on an Illumina NovaSeq instrument at either MedGenome Inc. or Admera Health, with the range of sequencing depth between 20M-50M reads.

Expression Constructs

CRM expression constructs were cloned into the Stagia3 expression vector with an Enhanced Gibson Assembly (Rabe & Cepko, 2020). For all constructs, the vector backbone was amplified from the expression vector using primers compvec_F/R (Table S1). For Olig2 and OLIG2 constructs, the intron-containing EGFP (GFPint) along with the rabbit β-globin polyadenylation sequence was amplified from Stagint7 whereas the insert for the Ngn2 constructs also included the TATAA minimal promoter upstream of EGFP. Olig2 CRMs, the Olig2 minimal promoter, Ngn2 CRMs, OLIG2 CRMs, and the OLIG2 minimal promoter were amplified from their respective BAC clones (all primers in Table S1). Coordinates for all regions are included in Table S2.

For individual constructs, Olig2-NR1 or Olig2-NR2 CRMs were inserted upstream the Olig2 minimal promoter and GFPint, whereas Olig2-NR3 CRM was assembled downstream of the GFPint + polyA sequence. The Olig2 composite construct was assembled accordingly, placing the NR1 and NR2 fragments adjacent to each other and upstream of the Olig2 minimal promoter, GFPint + polyA sequence, and NR3 fragment. Backbone plasmids containing GFPint alone or GFPint under the Olig2 minimal promoter in the absence of CRM fragments were also assembled (primers in Table S1)

The mouse Ngn2-CRM constructs were assembled placing the Ngn2-CRM1, CRM2, or CRM3 fragments upstream of the TATAA minimal promoter and GFPint, while the CRM4 fragment was placed downstream of the GFPint+polyA sequence. The chick OLIG2-CRM constructs were similarly constructed, with OLIG2-CRM1 or CRM2 fragments assembled upstream of the cOLIG2 minimal promoter, while the OLIG2-CRM3 fragment was assembled downstream of the GFPint+polyA sequence.

ddPCR

All ddPCR assays were performed on the Bio-Rad ddPCR system, including the automated droplet generator (Bio-Rad, cat. #1864101). *Olig2* gene expression was determined using Evagreen-based ddPCR with *Hprt* as a normalization control (primers in Table S1). cDNA was generated from isolated RNA with the LunaScript RT SuperMix Kit (NEB, cat. #E3010) from ~2–3 ng of total RNA and purified with the Zymo Oligo Clean & Concentrator kit. 1 ng of cDNA was added to each 22 µl ddPCR reaction; no-RT controls confirmed the absence of genomic DNA amplification (all assays spanned exon–exon junctions).

SEQUENCING, QUANTIFICATION, AND STATISTICAL ANALYSES

LS-MPRA Barcode Association and Quantification Analysis

Paired-end 150-bp sequencing reads were processed to establish barcode-fragment associations and quantify barcode abundances. Two custom shell scripts were used for sequencing data analysis.

Barcode-Fragment Association For barcode-fragment association, sequencing reads were aligned to the mm10 reference genome using Minimap2 version 2.28 (Li, 2018) and Bowtie2 version 2.5.4 (Langmead & Salzberg, 2012). Adapter sequences were trimmed using bbduk from the BBTools suite version 39.18 (Bushnell *et al.*, 2017), and barcode sequences were extracted from Read 1 using UMI-tools extract version 1.1.6 (Smith *et al.*, 2017). Valid barcode-fragment pairs were identified using UMI-tools group and filtered for library-specific sequences. Genomic coordinates were corrected based on barcode positions, and results were output as BigWig tracks

using deepTools bamCoverage version 3.5.5 (Ramirez *et al.*, 2016). Genomic coordinate manipulation, barcode overlap correction, and file conversions were performed using Bedtools version 2.31.1 (Quinlan & Hall, 2010), Samtools version 1.21 (Danecek *et al.*, 2021, Li *et al.*, 2009), and SeqKit version 2.6.1 (Shen *et al.*, 2016b).

An earlier version of the pipeline differed primarily in its alignment and filtering steps. Instead of Minimap2, it used BLAT version 35 (Kent, 2002) to align BAC sequences to the genome, extending flanking regions by 1 kb. Additionally, overlapping barcode-associated reads were collapsed using R packages GenomicRanges version 1.50.2 (Lawrence *et al.*, 2013), regioneR version 1.30.0 (Gel *et al.*, 2016), and data.table version 1.16.4 (Barrett *et al.*, 2025). Barcode extraction followed a similar approach but lacked the library-specific filtering step included in the updated version. By replacing BLAT with Minimap2 and incorporating stricter filtering, the updated pipeline improved alignment efficiency and accuracy.

Barcode Abundance Quantification: For barcode abundance quantification, extracted barcode sequences were filtered against a whitelist to exclude sequencing errors and ensure accuracy. The whitelist was generated by extracting reverse-complement barcode sequences from a reference FASTA file containing known barcode-fragment associations using the Biostrings R package version 2.66.0 (Pagès *et al.*, 2025). Pairwise Hamming distances were computed using the stringdist R package version 0.9.15 (van der Loo, 2014) to define a mutation threshold. All possible barcode variants within this threshold were enumerated and stored in an RDS file for downstream filtering. Sequencing reads were matched against this whitelist using UMI-tools extract, and barcode counts were normalized to library input using deepTools bamCompare. Normalized BigWig tracks were generated for visualization and analysis.

An earlier version of the pipeline extracted barcodes using bbduk and SeqKit, without applying Hamming distance-based error correction. Unique barcode counts were merged with barcode-fragment associations, and fragment counts were expanded to match observed barcode frequencies before normalization with bamCompare. While both methods yielded comparable results, the whitelist-based approach provided better error correction and filtering, enhancing reliability in downstream analyses.

All LS-MPRA plots were displayed on the Integrative Genomics Viewer (IGV) (Robinson *et al.*, 2011), and aligned with analyses of genetic conservation from the UCSC Genome Browser database (Perez *et al.*, 2025) as well as with RefSeq genes (O'Leary *et al.*, 2016).

ATAC-seq Analysis

Open chromatin regions were determined based on pseudo-bulk re-analysis of published single-cell ATAC-seq datasets (Lyu *et al.*, 2021), and deposited under accession number GSE181251. Deposited bam files were converted back to FASTQ format using bamtofastq version 1.3.2 from 10XGenomics (Github). Single-cell FASTQ files for E14 and P8 mouse retinas were analyzed using cellranger atac count version 2.0.0 (Satpathy *et al.*, 2019), where reads were filtered and aligned to the mm10 mouse genome, barcode counted, and transposase cut sites identified. Regions of accessible chromatin were detected on a single-cell basis. Bam files contained all the aligned paired-end reads were used to determine pseudo-bulk genome coverage using Deeptools version 3.5 (Ramirez *et al.*, 2016), normalized using RPKM, and filtered for blacklisted (Amemiya *et al.*, 2019), gap and repeat regions, and visualized using IGV (Robinson *et al.*, 2011, Thorvaldsdottir *et al.*, 2013).

CUT&RUN Analysis

Analysis of sequenced samples from the CUT&RUN experiments were analyzed as previously described (Catta-Preta *et al.*, 2025). FASTQ files containing the reads were controlled for quality using FASTQC version 0.11.9 (Andrews, 2010), and further cleaned up of remaining adapter sequences using Trim Galore version 0.6.6 (Krueger, 2015). The resulting pair-ended reads were aligned to the mm10 mouse genome using BWA mem version 0.7.17 (Li & Durbin, 2009), and duplicates removed with Samtools version 1.15.1 (Li *et al.*, 2009). Peaks of enriched immunoprecipitated regions against IgG (negative) control were called using MACS version 2.1.1 (Zhang *et al.*, 2008) with a p-value of 0.05, extension size 200, no lambda baseline correction. Genome coverage from the bam files for all samples was determined using Deeptools version 3.5 (Ramirez *et al.*, 2016), normalized using RPKM, and filtered for blacklisted (Amemiya *et al.*, 2019), gap, and repeat regions. Coverage was visualized using IGV (Robinson *et al.*, 2011, Thorvaldsdottir *et al.*, 2013). Motif enrichment and specific motif presence was determined using Homer version 4.11.1 (Heinz *et al.*, 2010).

D-MPRA Plasmid and Experimental Library Processing

To analyze barcode-fragment associations and quantify changes in mutated fragment (i.e., barcode) frequency in d-MPRA plasmid and experimental libraries, sequencing data were processed through a pipeline involving read merging, alignment, barcode extraction, and statistical analysis of barcode frequencies across CRM sequences.

Plasmid Library Processing: Plasmid control libraries were processed by merging paired-end reads and aligning them to reference sequences using Minimap2 and pysam version 0.22.1 (Bonfield *et al.*, 2021). Barcode and fragment associations were then analyzed by parsing Minimap2's cs tags, with mutations identified and quantified using custom Python scripts that leveraged NumPy version 1.26.3 (Harris *et al.*, 2020) and pandas version 2.1.4 (McKinney, 2010) for data handling. Reads containing deletions within homopolymer regions were excluded based on positions identified from reference FASTA sequences, and reads failing to align fully across the contig were discarded. Monte Carlo simulations were implemented using multiprocessing to perform 10 independent subsampling replicates, and barcode mutation frequencies were normalized to wild-type sequence counts for accurate mutation rate estimation.

Experimental Library Processing: Reads from experimental d-MPRA libraries were merged and aligned similarly to the plasmid workflow, and barcode-fragment associations were identified. An additional filtering step was applied to remove reads that failed to align fully across the contig, reducing false-positive mutation calls.

Mutation Filtering and Statistical Analysis: Both plasmid and experimental workflows applied stringent mutation filtering, discarding deletions occurring in homopolymer regions. Substitutions and deletions were quantified using pysam to parse cs tags from alignments produced by Minimap2, and filtered with logic implemented in numpy and pandas. Barcode frequencies were normalized relative to plasmid control counts using data structures and sampling routines implemented in pandas, numpy, and Python's multiprocessing library. Monte Carlo sampling was used to refine barcode frequency estimates while accounting for sequencing depth. Final mutation statistics, including mean and standard deviation across positions and replicates, were compiled using pandas and json, ensuring accurate and robust quantification of sequence variation. This workflow ensured precise quantification of barcode frequency in both plasmid and experimental d-MPRA libraries while minimizing sequencing artifacts.

Visualization of d-MPRA Profiles

To visualize barcode frequency distributions across CRMs, normalized mutation rates from Monte Carlo-sampled plasmid controls and experimental d-MPRA libraries were compared and plotted. Barcode frequencies corresponding to substitutions and deletions in the experimental datasets were extracted from position-level JSON summaries. These values were normalized to corresponding wild-type-corrected rates from plasmid controls and $\log_2$-transformed to assess relative mutation enrichment or depletion.

To reduce noise and account for local sequence context, the data were smoothed using a five-base sliding window moving average. A baseline correction was applied to each dataset by subtracting the median $\log_2$-transformed value prior to smoothing. For each genomic position, only sites present in both control and experimental datasets were retained for comparison. Edge regions flanking the CRM, specifically, the first 18 and last 14 positions, were excluded from visualization to eliminate non-informative regions required for construct assembly.

For each replicate, baseline-corrected mutation rates were plotted individually alongside the average profile across all replicates. All visualizations were generated in Python using matplotlib version 3.8.2 (Hunter, 2007) and numpy.

Quantification of *Olig2* Transcript Levels Using ddPCR

ddPCR was used to quantify the concentration of *Olig2* transcripts in treated and control retinas across multiple time points. Normalized transcript concentrations were determined from ddPCR reactions and analyzed in GraphPad Prism. Statistical comparisons between treated and control groups were performed using unpaired t-tests assuming equal standard deviations, with multiple testing correction applied using the Holm-Šídák method.

Quantification of Barcode Enrichment Using AUC Analysis

CRM barcode enrichment was quantified by calculating the area under the curve (AUC) using BigWig sequencing files. Normalized barcode count values were extracted for the CRM genomic regions, and AUC was computed using the trapezoidal rule. Statistical analysis was performed in GraphPad Prism using Brown-Forsythe and Welch's ANOVA tests, followed by Dunnett's T3 multiple comparisons test to assess significance.

Quantification of Cell Populations Using a Semi-Automatic Colocalization Analysis Toolbox

Fluorescent cell counting was performed using a semi-automatic object-based colocalization analysis (OBCA) toolbox developed by Lunde and Glover (Lunde & Glover, 2020). This toolbox comprises two ImageJ plugins, a Microsoft Excel macro, and a MATLAB script, facilitating efficient analysis of complex imaging data. The first ImageJ plugin was employed to enhance visualization of multichannel 3D images, optimizing features relevant to OBCA. The second plugin enabled semi-automatic quantification of colocalization across multiple fluorescence channels. In this study, cells expressing a specific gene transcript or protein, GFP driven by CRM activity, and BFP from an electroporation control plasmid were identified. The toolbox provided counts of cells co-expressing the gene transcript, GFP protein, and/or GFP transcript. These data were used to calculate the percentage of electroporated (BFP+) cells expressing the specific gene transcript that also expressed GFP protein, GFP transcript, or both, for each analyzed section. Additionally, the percentage of GFP+ cells co-expressing the gene transcript was determined.

Motif Analysis

De novo motif analysis was performed on CRM sequences using the HOMER tool (findMotifsGenome.pl) (Heinz *et al.*, 2010). The motif search was performed on CRM coordinates in the mm10 genome assembly using a fixed size for each CRM region and a randomly generated reference genome directory. HOMER's built-in TF binding site database, derived from JASPAR, was used to detect known TF binding sites within the discovered motifs. The analysis output was used to identify potential regulatory factors enriched in these enhancer regions. The comprehensive list of potential TF binding sites within each predicted motif of the Olig2 CRMs is available at the online repository (Tulloch, 2025).

Visualization of PFMs: Position frequency matrices (PFMs) for selected TFBSs were parsed and visualized using a custom Python script. PFMs were read into a pandas DataFrame and transposed to organize nucleotide frequencies by position. Rows were normalized to ensure that nucleotide frequencies summed to one at each position. The information content at each position was calculated using Shannon entropy, incorporating a small pseudocount to avoid undefined logarithmic values. Sequence logos were generated using Logomaker (Tareen & Kinney, 2020), with bit scores computed by multiplying nucleotide frequencies by their respective information content.

Single-Cell RNA-Seq Data Acquisition and Processing

scRNA-seq data for retinal development across multiple ages were obtained from the published data repository at https://github.com/gofflab/developing_mouse_retina_scRNASeq (Clark *et al.*, 2019). The dataset included:

1. a gene expression counts matrix (*10x_mouse_retina_development.mtx*)
2. gene feature annotations (*10x_mouse_retina_development_feature.csv*)
3. sample-level metadata (*10x_mouse_retina_development_phenotype.csv*).

The raw counts matrix was processed and analyzed using Seurat v4.0 (Butler et al., 2018).

Data Preprocessing: The scRNA-seq data were processed in R using Seurat (Hao *et al.*, 2024). The raw counts matrix was loaded with `Read10X()` and converted into a Seurat object. Genes detected in fewer than three cells were removed, and cells with fewer than 200 detected genes or >5% mitochondrial gene content were excluded. To normalize for sequencing depth, the SCTransform workflow was applied, followed by identification of highly variable genes.

Subset Analysis by Developmental Age: To focus on specific developmental stages, cells were subsetted based on "age metadata". Two ages were subsetted: E14 and P8. Dimensionality reduction, clustering, and Uniform Manifold Approximation and Projection (UMAP) visualization (McInnes *et al.*, 2018) were performed on each subset independently.

Dimensionality Reduction and Clustering: Principal component analysis (PCA) was performed on the top 2,000 variable genes. UMAP was used for visualization, and clustering was conducted using `FindNeighbors()` and `FindClusters()` with a resolution of 0.5 to delineate distinct retinal cell populations. UMAP plots were generated using `DimPlot()`, with cells color-coded by cell type, developmental stage, or gene expression levels.

Gene Expression and Co-Expression Analysis: The expression of individual genes of interest was visualized using `FeaturePlot()`. A continuous color gradient (light grey to blue) was applied to indicate expression levels. To visualize gene co-expression, `FeaturePlot()` was used with blend = TRUE, where cells expressing Gene1 appeared in blue, Gene2 in red, and co-expressing cells in pink. The third panel of the blended plot, which represents co-expression, was

extracted and saved using `ggsave()`. All visualizations were generated in R using ggplot2 (Wickham, 2016).

Quantification of Co-Expressing Cells: Expression data for genes of interest were extracted from the RNA assay slot of the Seurat object using `GetAssayData()`. Cells were classified as expressing a gene if their count was greater than zero. The number of cells expressing each gene individually and both genes concurrently was computed. The percentage of Gene1-expressing cells that also expressed Gene2 was calculated as:
Percent Co-Expression
=(Cells expressing both genesTotal cells expressing Gene1)×100\text{Percent Co-Expression}
= \left(\frac{\text{Cells expressing both genes}}{\text{Total cells expressing Gene1}}\right)
\times 100Percent Co-Expression
=(Total cells expressing Gene1Cells expressing both genes)×100

Statistical Analysis of Gene Co-Expression with Olig2 from scRNAseq
To assess whether specific genes were significantly enriched or depleted in *Olig2*-expressing cells, Fisher's exact test for each gene of interest was performed. Gene expression data were obtained from the RNA count matrix of the retinal single-cell dataset. Cells were classified as expressing a given gene if the raw count value was greater than zero.

For each gene, a 2×2 contingency table was constructed, categorizing cells as *Olig2*+ or *Olig2*− and as expressing or not expressing the target gene. Fisher's exact test was then applied to each contingency table to determine whether the presence of a given gene was significantly associated with *Olig2* expression. To account for multiple hypothesis testing, the Benjamini-Hochberg false discovery rate (FDR) correction was applied to the resulting p-values. Genes with an adjusted p-value (FDR q-value) below 0.05 were considered significantly enriched or depleted in *Olig2*-expressing cells. An odds ratio greater than 1 indicated that the gene was enriched in *Olig2*+ cells, whereas an odds ratio less than 1 indicated depletion in *Olig2*+ cells.

LEGENDS

Figure 1. Overview of the LS-MPRA. (**A**) Schematic representation of LS-MPRA. BACs containing genomic regions of interest are enzymatically fragmented to generate a high-complexity DNA library. Size selected fragments are cloned into a vector containing a minimal promoter that will drive expression of GFP and a barcode positioned within the 3′ untranslated region (UTR). The LS-MPRA library is then electroporated into retinal cells, where CRM activity is inferred by quantifying barcode enrichment in transcribed mRNA. (**B**) Illustration of fragment-barcoding strategy and necessary elements to sequence, wherein each DNA fragment is uniquely barcoded. (**C**) Preparation and sequencing of the plasmid library, associating fragment-barcode pairs, and establishing a baseline for barcode abundance, which is used to normalize barcode counts after mapping of barcode-labeled fragments to genomic coordinates. ORF, open reading frame; BC, barcode.

Figure 2. Rho LS-MPRA to identify CRMs in the neonatal mouse retina. (**A**) LS-MPRA barcode enrichment plots for the Rho locus aligned to a genome browser track from *in vivo* and *ex vivo* experiments (N=3 experimental replicates, combined), and annotated with: (i) known *Rho* regulatory regions, (ii) the coverage of the barcode–fragment association library across the locus, (iii) $\log_2$-transformed base conservation among 60 vertebrate and 40 placental mammal species, (iv) regions of open chromatin in the P8 mouse retina, and (v) RefSeq gene models for the locus. (**B**) Expanded view of a region of interest from the Rho LS-MPRA plot, showing peaks (**i-v**) that correspond to known regulatory regions (red bars), genomic conservation, and areas of open chromatin.

Supplemental Figure 2S. Grm6, Vsx2, and Cabp5 LS-MPRAs to identify CRMs in the neonatal mouse retina. Barcode enrichment plots from the Grm6 (**A**), Vsx2 (**B**), and Cabp5 (**C**) LS-MPRAs, aligned with genome browser tracks and annotated with (i) known regulatory regions, (ii) coverage of the barcode-fragment association library across the locus, (iii) $\log_2$ base conservation across 60 vertebrate or 40 placental mammal species, (iv) regions of open chromatin in the P8 mouse retina, and (v) RefSeq gene models. Expanded regions of interest (yellow dashed boxes) show peaks (**i-iii**) or regions that align with known regulatory elements for each gene.

Figure 3: Olig2 LS-MPRA to identify candidate CRMs in the developing mouse retina. (**A**) Barcode enrichment plot from the Olig2 LS-MPRA, aligned with a genome browser track and annotated with (i) previously described *Olig2* regulatory regions identified in mouse embryonic stem cells, fertilized murine oocytes, a mouse lymphoma cell line, or in mouse ventral neural tube (Chen *et al.*, 2008, Fan *et al.*, 2023, Friedli *et al.*, 2010, Sun *et al.*, 2023), (ii) coverage of the barcode-fragment association library across the locus, (iii) $\log_2$ base conservation across 60 vertebrate or 40 placental mammal species, (iv) regions of open chromatin in the E14 mouse retina, and (v) RefSeq gene models. (**B**) Two expanded regions of interest from the Olig2 LS-MPRA, showing peaks that align with known regulatory elements, genomic conservation, and open chromatin. Candidate CRMs identified within blue bars.

Figure 4. Dynamic CRM activity and *Olig2* expression following inhibition of Notch signaling. (**A**) Bar plot showing relative endogenous *Olig2* RNA expression in the retina over 0–24 hours

of treatment with the γ-secretase inhibitor LY411575 or DMSO, normalized to the 0-hour control. Unpaired *t*-tests with Holm's multiple comparisons correction were performed for each Control vs. Treated timepoint. (**B**) Barcode enrichment plot from the Olig2 LS-MPRA, aligned with a genome browser track after 0–28 hours of LY411575 treatment. Notch inhibitor-responsive CRM candidate regions (NR1–3, blue boxes) displayed differential barcode enrichment across the treatment period. Statistical analysis was performed using one-way Welch's ANOVA with Dunnett's T3 multiple comparisons test on AUC values, normalized to the 0-hour timepoint. Error bars in (**A**) and (**B**) represent SEM. Asterisks indicate statistical significance (*$p \leq 0.05$, **$p \leq 0.01$, ***$p \leq 0.001$).

Figure 5. Co-localization of GFP driven by Olig2 CRMs and Olig2 in retinal cells. (**A**) Schematic of plasmid constructs containing one or all Notch inhibitor-responsive regions driving GFP expression with the endogenous *Olig2* minimal promoter, alongside the experimental workflow. (**B**) Representative transverse sections of E14 retinas electroporated with these plasmids, incubated *in vitro* for 24 hours, and stained using IHC for GFP and Olig2. Merged and single-channel images show GFP colocalization with Olig2 (orange arrow) as well as GFP^+ cells lacking detectable Olig2 expression (yellow arrow). (**C**) Quantification of GFP and Olig2 co-localization, represented as pie charts showing (i) the percentage of electroporated Olig2+ cells that express GFP protein, (ii) the percentage of GFP protein+ cells that express Olig2, and (iii) the percentage of electroporated Olig2- cells that express GFP protein in retinas electroporated at E14 with plasmids containing one or all Notch inhibitor-responsive regions driving GFP. Scale bar: 20µm.

Supplemental Figure 5S. Activity of backbone plasmids containing the *Olig2* minimal promoter and *EGFP*. (**A**) Representative transverse sections of E14 retinas incubated *in vitro* for 24 hours show sparse *GFP* RNA and GFP fluorescence driven by control plasmids containing either *EGFP* alone or *EGFP* under the *Olig2* minimal promoter. Pie charts of the percentage of electroporated cells with detectable GFP expression.

Figure 6. Co-localization of CRM-directed RNA and *Olig2* RNA or protein in retinal cells. (**A-C**) Representative transverse sections of E14 retinas incubated *in vitro* for 24 hours for analysis of localization patterns of Olig2 and/or GFP. (**A**) Sections stained for Olig2 protein (cyan, yellow arrows) using IHC and *Olig2* RNA (red, magenta arrows) using FISH. A 100% stacked column plot quantifies the overlap between Olig2 protein and *Olig2* RNA expression. (**B**) Intrinsic GFP fluorescence and *GFP* RNA driven by Olig2-NR1 (yellow and magenta arrows). (**C**) In retinas electroporated with plasmids containing one or all Notch inhibitor-responsive regions, *Olig2* RNA co-localized with GFP protein only (yellow arrow), *GFP* RNA only (magenta arrow), or both (orange arrow). (**D**) Pie charts quantifying (column 1) the percentage of electroporated *Olig2* RNA+ cells that expressed GFP, (column 2) the percentage of *GFP* RNA+ cells that expressed *Olig2* RNA, (column 3) the percentage of GFP protein+ cells that expressed *Olig2* RNA, and (column 4) the percentage of *Olig2* RNA- cells that expressed GFP in retinas electroporated. Scale bar: 20µm.

Figure 7. Degenerate MPRAs to identify functional residues within candidate CRMs. (**A**) Schematic of d-MPRA library assembly. Point mutations were introduced into *Olig2* CRM fragments via error-prone PCR, followed by intraplasmid duplication (IPD) to generate

constructs with duplicated mutant CRMs flanking a minimal promoter and GFP ORF. The 3′ CRM copy, located in the 3′ UTR, served as a barcode, with a WPRE sequence included to potentially stabilize transcripts. (**B**) Conceptual diagram illustrating expected d-MPRA results, showing predicted changes in CRM activity upon disruption of enhancer or repressor binding sites. (**C-E**) d-MPRA plots displaying $\log_2$ fold changes in mutational frequencies using a 5-base pair sliding window average, normalized across the *Olig2*-NR1 (**C**), *Olig2*-NR2 (**D**), and *Olig2*-NR3 (**E**) regions.

Figure 8. TF binding sites within the Olig2-NR2 CRM. (**A**) TF binding motifs predicted using HOMER identified within the *Olig2*-NR2 CRM candidate, aligned with the average d-MPRA plot for this region (from Fig. 7). (**B-D**) Position frequency matrices of TF binding sites aligned to motifs predicted by HOMER in *Olig2*-NR2: Mybl1 to Motif 1 (**B**), Foxn4 and Pax6 to Motif 3 (**C**), and Otx2 to Motif 14 (**D**). (**E**) UMAP visualization of scRNA profiles from E14 mouse retinas, with cell types previously identified by marker genes by Clark et al. (2019). (**F**) Expression of *Olig2* on UMAP. (**G**) Co-expression (pink) of *Olig2* (blue) with *Mybl1, Foxn4, Pax6*, or *Otx2* (red) on UMAP. Percentages of respective populations that co-express *Olig2* are indicated (* denotes significance). (**H**) TF occupancy track aligned to (i) *Olig2* LS-MPRA barcode enrichment after 12-hour LY411575 treatment (replicate of Fig. **4B**) and (ii) gene models. Occupancy peaks for Mybl1, Foxn4, and Pax6 align with the Olig2-NR2 CRM candidate (blue box).

Supplemental Figure 8S. TF Binding sites in Olig2-NR1 and NR3 CRMs. (**A, H**) TF binding motifs identified within Olig2-NR1 (**A**) and Olig2-NR3 (**H**) CRM candidates, aligned with the average d-MPRA plot (from Fig. 7). (**B-F, I-K**) Position frequency matrices of transcription factors aligning to Olig2-NR1: Sox4/11 to Motifs 13 and 16 (**B**), Lhx2 and Dlx2 to Motif 11 (**C**), Isl1 to Motif 8 (**D**), Foxp1 to Motif 18 (**E**), Mybl1 to Motif 2 (**F**), and Otx2 to Motif 12 (**F**); or Olig2-NR3: Ngn2 to Motifs 3 and 5 (**I**), Bhlhe22 to Motif 13 (**J**), and Lhx9 to Motif 15 (**K**). (**G, L**) Co-expression (pink) of *Olig2* (blue) with *Sox11, Sox4, Lhx2, Dlx2, Isl1,* or *Foxp1* (red) for Olig2-NR1 (**G**) and *Ngn2, Bhlhe22,* or *Lhx9* (red) for Olig2-NR3 (**L**) on UMAP visualization of E14 mouse retinal gene expression. Percentages of respective populations that co-express *Olig2* are indicated (* denotes significance).

Figure 9. Ngn2 LS-MPRA to identify CRM candidates active in mouse retinal cells expressing *Ngn2*. (**A**) Ngn2 LS-MPRA barcode enrichment plot aligned with a genome browser track, annotated with (i) known *Ngn2* regulatory regions, (ii) coverage of the barcode-fragment association library, (iii) $\log_2$ base conservation across 60 vertebrate or 40 placental mammal species, (iv) regions of open chromatin in E14 mouse retina, (v) gene models, and (vi) CRM candidate regions 1-4 (blue boxes). (**B**) Representative transverse sections of E14 retinas incubated for 24 hours *in vitro*, showing localization of *Ngn2* RNA with *GFP* RNA only (magenta arrow) or both intrinsic GFP and *GFP* RNA (orange arrows) in retinas electroporated with plasmids containing one of the CRM1-4 regions. (**C**) Pie charts showing the percentage of *Ngn2* RNA+ cells expressing GFP (column 1), *GFP* RNA+ cells expressing *Ngn2* RNA (column 2), GFP protein+ cells expressing *Ngn2* RNA (column 3), and *Ngn2* RNA- cells expressing GFP (column 4) in retinas electroporated at E14 with plasmids containing CRM1-4 regions driving GFP. (**D**) Co-localization analysis of Ngn2-CRM3 plasmid and GFP following 16-hour incubation *in vitro*. Scale bar: 20µm.

Figure 10. OLIG2 LS-MPRA to identify CRM candidates in chick embryos. (**A**) OLIG2 LS-MPRA barcode enrichment plot following electroporation into E5 chick retinal explants, and E2 spinal cords and E4 spinal cords *in ovo*, aligned with a genome browser track and annotated with (i) coverage of the barcode-fragment association library, (ii) $\log_2$ base conservation across 77 vertebrate species, (iii) gene models, and (iv) CRM candidate regions 1-3 (blue boxes). (**B**) Representative transverse sections of E5 chick retinas incubated for 24 hours *in vitro*, showing localization of chick *OLIG2* RNA with *GFP* RNA only (magenta arrow) or both intrinsic GFP fluorescence and GFP RNA (orange arrows) driven by plasmids containing one of the CRM1-3 regions. (**C**) Pie charts showing the percentage of *OLIG2* RNA+ cells expressing GFP (column 1), *GFP* RNA+ cells expressing *OLIG2* RNA (column 2), GFP protein+ cells expressing *OLIG2* RNA (column 3), and *OLIG2* RNA- cells expressing GFP (column 4) in retinas electroporated at E5 with plasmids containing CRM1-3 regions driving GFP and visualized by FISH. Scale bar: 20µm.

Supplemental Figure 10S. Activity of OLIG2 CRMs in OLIG2+ cells within embryonic chick spinal cords. (**A**) Schematic of an E2 chick transverse spinal cord with the field of view (red outline) shown in **B**. (**B**) Representative transverse hemi-sections of ventral E2 chick spinal cords incubated for 24 hours *in ovo*, showing (i) *OLIG2* RNA localized with *GFP* RNA (orange arrow), (ii) *OLIG2* expression in GFP- cells (yellow arrows), and (iii) *GFP* RNA expression in *OLIG2*- cells (magenta arrows). GFP expression is driven by plasmids containing one of the CRM candidate regions (CRM1-3). Scale bar: 20µm.

Figure 11. Activity of Olig2 CRM candidates in postnatal retinal cells expressing Olig2. (**A**) Representative transverse sections of postnatal retinas electroporated at P0 and incubated *in vivo* for 24 hours, stained with antibodies against Olig2 and GFP to identify co-localized expression (orange arrows). GFP expression was driven by plasmids containing one or more Notch-inhibitor responsive regions (NR1-3). (**B**) Analysis of GFP and Olig2 co-localization, shown with pie charts depicting the percent of Olig2+ electroporated cells expressing GFP (column 1), the percent of GFP+ cells expressing Olig2 (column 2), and the percent of Olig2- electroporated cells expressing GFP in retinas electroporated at P0 with plasmids containing one or more Notch-inhibitor responsive regions driving GFP. Scale bar: 20µm.

ACKNOWLEDGEMENTS:

First, we thank Dr. Brian Rabe for developing the original LS-MPRA and d-MPRA methods that formed the basis of this study. We would like to thank Dr. Changhee Lee for discussions related to the study design and for expertise in methodology. As well, we thank Dr. Ryoji Amamoto and Henry Bushnell for expertise in methodology. We would also like to thank Dr. Paula Montero Llopis, Dr. Praju Vikas Anekal, and Dr. Adrienne Wells from the MicRoN imaging core at Harvard Medical School for providing expert advice concerning imaging and analysis. We thank BioRender for assisting in the creation of several schematics (https://BioRender.com). We are grateful to the Howard Hughes Medical Institute (C.L.C. and A.J.T.), the National Eye Institute (5K99EY034603, R.N.D. and 5R01EY029771 R.C-P) for support.

REFERENCES

Advani J, Mehta PA, Hamel AR, Mehrotra S, Kiel C, Strunz T, Corso-Diaz X, Kwicklis M, van Asten F, Ratnapriya R, Chew EY, Hernandez DG, Montezuma SR, Ferrington DA, Weber BHF, Segre AV, Swaroop A. 2024. QTL mapping of human retina DNA methylation identifies 87 gene-epigenome interactions in age-related macular degeneration. *Nat Commun* 15: 1972. PMID: 38438351.

Agarwal V, Inoue F, Schubach M, Penzar D, Martin BK, Dash PM, Keukeleire P, Zhang Z, Sohota A, Zhao J, Georgakopoulos-Soares I, Noble WS, Yardimci GG, Kulakovskiy IV, Kircher M, Shendure J, Ahituv N. 2025. Massively parallel characterization of transcriptional regulatory elements. *Nature*. PMID: 39814889.

Alexiades MR, Cepko C. 1996. Quantitative analysis of proliferation and cell cycle length during development of the rat retina. *Dev Dyn* 205: 293-307. PMID: 8850565.

Amemiya HM, Kundaje A, Boyle AP. 2019. The ENCODE Blacklist: Identification of Problematic Regions of the Genome. *Sci Rep* 9: 9354. PMID: 31249361.

Andrews S. 2010. *FASTQC. A quality control tool for high throughput sequence data*. https://www.bioinformatics.babraham.ac.uk/projects/fastqc/

Arnold CD, Gerlach D, Stelzer C, Boryn LM, Rath M, Stark A. 2013. Genome-wide quantitative enhancer activity maps identified by STARR-seq. *Science* 339: 1074-7. PMID: 23328393.

Balasubramanian R, Bui A, Ding Q, Gan L. 2014. Expression of LIM-homeodomain transcription factors in the developing and mature mouse retina. *Gene Expr Patterns* 14: 1-8. PMID: 24333658.

Balasubramanian R, Bui A, Dong X, Gan L. 2018. Lhx9 Is Required for the Development of Retinal Nitric Oxide-Synthesizing Amacrine Cell Subtype. *Mol Neurobiol* 55: 2922-33. PMID: 28456934.

Barrett T, Dowle M, Srinivasan A, Gorecki J, Chirico M, Hocking T, Schwendinger B, Krylov I. 2025. *data.table: Extension of 'data.frame'*. 1.17.99. https://Rdatatable.gitlab.io/data.table

Billings NA, Emerson MM, Cepko CL. 2010. Analysis of thyroid response element activity during retinal development. *PLoS One* 5: e13739. PMID: 21060789.

Bonfield JK, Marshall J, Danecek P, Li H, Ohan V, Whitwham A, Keane T, Davies RM. 2021. HTSlib: C library for reading/writing high-throughput sequencing data. *Gigascience* 10. PMID: 33594436.

Brzezinski JAt, Kim EJ, Johnson JE, Reh TA. 2011. Ascl1 expression defines a subpopulation of lineage-restricted progenitors in the mammalian retina. *Development* 138: 3519-31. PMID: 21771810.

Buenaventura DF, Ghinia-Tegla MG, Emerson MM. 2018. Fate-restricted retinal progenitor cells adopt a molecular profile and spatial position distinct from multipotent progenitor cells. *Dev Biol* 443: 35-49. PMID: 30145104.

Buschmann T. 2017. DNABarcodes: an R package for the systematic construction of DNA sample tags. *Bioinformatics* 33: 920-22. PMID: 28052927.

Bushnell B, Rood J, Singer E. 2017. BBMerge - Accurate paired shotgun read merging via overlap. *PLoS One* 12: e0185056. PMID: 29073143.

Catta-Preta R, Lindtner S, Ypsilanti A, Seban N, Price JD, et al. 2025. Combinatorial transcription factor binding encodes cis-regulatory wiring of mouse forebrain GABAergic neurogenesis. *Dev Cell* 60: 288-304 e6. PMID: 39481376.

Cepko C. 2014. Intrinsically different retinal progenitor cells produce specific types of progeny. *Nat Rev Neurosci* 15: 615-27. PMID: 25096185.

Chan CSY, Lonfat N, Zhao R, Davis AE, Li L, Wu MR, Lin CH, Ji Z, Cepko CL, Wang S. 2020. Cell type- and stage-specific expression of Otx2 is regulated by multiple transcription factors and cis-regulatory modules in the retina. *Development* 147. PMID: 32631829.

Chen CT, Gottlieb DI, Cohen BA. 2008. Ultraconserved elements in the Olig2 promoter. *PLoS One* 3: e3946. PMID: 19079603.

Clark BS, Stein-O'Brien GL, Shiau F, Cannon GH, Davis-Marcisak E, Sherman T, Santiago CP, Hoang TV, Rajaii F, James-Esposito RE, Gronostajski RM, Fertig EJ, Goff LA, Blackshaw S. 2019.

Single-Cell RNA-Seq Analysis of Retinal Development Identifies NFI Factors as Regulating Mitotic Exit and Late-Born Cell Specification. *Neuron* 102: 1111-26 e5. PMID: 31128945.
Consortium EP, Moore JE, Purcaro MJ, Pratt HE, Epstein CB, et al. 2020. Expanded encyclopaedias of DNA elements in the human and mouse genomes. *Nature* 583: 699-710. PMID: 32728249.
Corbo JC, Lawrence KA, Karlstetter M, Myers CA, Abdelaziz M, Dirkes W, Weigelt K, Seifert M, Benes V, Fritsche LG, Weber BH, Langmann T. 2010. CRX ChIP-seq reveals the cis-regulatory architecture of mouse photoreceptors. *Genome Res* 20: 1512-25. PMID: 20693478.
Cvekl A, Callaerts P. 2017. PAX6: 25th anniversary and more to learn. *Exp Eye Res* 156: 10-21. PMID: 27126352.
Danecek P, Bonfield JK, Liddle J, Marshall J, Ohan V, Pollard MO, Whitwham A, Keane T, McCarthy SA, Davies RM, Li H. 2021. Twelve years of SAMtools and BCFtools. *Gigascience* 10. PMID: 33590861.
de Melo J, Du G, Fonseca M, Gillespie LA, Turk WJ, Rubenstein JL, Eisenstat DD. 2005. Dlx1 and Dlx2 function is necessary for terminal differentiation and survival of late-born retinal ganglion cells in the developing mouse retina. *Development* 132: 311-22. PMID: 15604100.
Emerson MM, Cepko CL. 2011. Identification of a retina-specific Otx2 enhancer element active in immature developing photoreceptors. *Dev Biol* 360: 241-55. PMID: 21963459.
Fan C, Kim D, An H, Park Y. 2023. Identifying an oligodendrocyte enhancer that regulates Olig2 expression. *Hum Mol Genet* 32: 835-46. PMID: 36193754.
Farhy C, Elgart M, Shapira Z, Oron-Karni V, Yaron O, Menuchin Y, Rechavi G, Ashery-Padan R. 2013. Pax6 is required for normal cell-cycle exit and the differentiation kinetics of retinal progenitor cells. *PLoS One* 8: e76489. PMID: 24073291.
Feng L, Xie X, Joshi PS, Yang Z, Shibasaki K, Chow RL, Gan L. 2006. Requirement for Bhlhb5 in the specification of amacrine and cone bipolar subtypes in mouse retina. *Development* 133: 4815-25. PMID: 17092954.
Friedli M, Barde I, Arcangeli M, Verp S, Quazzola A, Zakany J, Lin-Marq N, Robyr D, Attanasio C, Spitz F, Duboule D, Trono D, Antonarakis SE. 2010. A systematic enhancer screen using lentivector transgenesis identifies conserved and non-conserved functional elements at the Olig1 and Olig2 locus. *PLoS One* 5: e15741. PMID: 21206754.
Gel B, Diez-Villanueva A, Serra E, Buschbeck M, Peinado MA, Malinverni R. 2016. regioneR: an R/Bioconductor package for the association analysis of genomic regions based on permutation tests. *Bioinformatics* 32: 289-91. PMID: 26424858.
Github. 2022. *10XGenomics/bamtofastq: Convert 10x BAM files to the original FASTQs compatible with 10x pipelines* v1.4.1. https://github.com/10XGenomics/bamtofastq
Gordon PJ, Yun S, Clark AM, Monuki ES, Murtaugh LC, Levine EM. 2013. Lhx2 balances progenitor maintenance with neurogenic output and promotes competence state progression in the developing retina. *J Neurosci* 33: 12197-207. PMID: 23884928.
Haeseleer F, Sokal I, Verlinde CL, Erdjument-Bromage H, Tempst P, Pronin AN, Benovic JL, Fariss RN, Palczewski K. 2000. Five members of a novel Ca(2+)-binding protein (CABP) subfamily with similarity to calmodulin. *J Biol Chem* 275: 1247-60. PMID: 10625670.
Hafler BP, Surzenko N, Beier KT, Punzo C, Trimarchi JM, Kong JH, Cepko CL. 2012. Transcription factor Olig2 defines subpopulations of retinal progenitor cells biased toward specific cell fates. *Proc Natl Acad Sci U S A* 109: 7882-7. PMID: 22543161.
Hao Y, Stuart T, Kowalski MH, Choudhary S, Hoffman P, Hartman A, Srivastava A, Molla G, Madad S, Fernandez-Granda C, Satija R. 2024. Dictionary learning for integrative, multimodal and scalable single-cell analysis. *Nat Biotechnol* 42: 293-304. PMID: 37231261.
Harris CR, Millman KJ, van der Walt SJ, Gommers R, Virtanen P, et al. 2020. Array programming with NumPy. *Nature* 585: 357-62. PMID: 32939066.
Hatakeyama J, Tomita K, Inoue T, Kageyama R. 2001. Roles of homeobox and bHLH genes in specification of a retinal cell type. *Development* 128: 1313-22. PMID: 11262232.

Heinz S, Benner C, Spann N, Bertolino E, Lin YC, Laslo P, Cheng JX, Murre C, Singh H, Glass CK. 2010. Simple combinations of lineage-determining transcription factors prime cis-regulatory elements required for macrophage and B cell identities. *Mol Cell* 38: 576-89. PMID: 20513432.
Henke RM, Savage TK, Meredith DM, Glasgow SM, Hori K, Dumas J, MacDonald RJ, Johnson JE. 2009. Neurog2 is a direct downstream target of the Ptf1a-Rbpj transcription complex in dorsal spinal cord. *Development* 136: 2945-54. PMID: 19641016.
Hollyday M, Hamburger V. 1977. An autoradiographic study of the formation of the lateral motor column in the chick embryo. *Brain Res* 132: 197-208. PMID: 890480.
Honnell V, Norrie JL, Patel AG, Ramirez C, Zhang J, Lai YH, Wan S, Dyer MA. 2022. Identification of a modular super-enhancer in murine retinal development. *Nat Commun* 13: 253. PMID: 35017532.
Hrvatin S, Tzeng CP, Nagy MA, Stroud H, Koutsioumpa C, Wilcox OF, Assad EG, Green J, Harvey CD, Griffith EC, Greenberg ME. 2019. A scalable platform for the development of cell-type-specific viral drivers. *Elife* 8. PMID: 31545165.
Huang L, Hu F, Feng L, Luo XJ, Liang G, Zeng XY, Yi JL, Gan L. 2014. Bhlhb5 is required for the subtype development of retinal amacrine and bipolar cells in mice. *Dev Dyn* 243: 279-89. PMID: 24123365.
Hufnagel RB, Le TT, Riesenberg AL, Brown NL. 2010. Neurog2 controls the leading edge of neurogenesis in the mammalian retina. *Dev Biol* 340: 490-503. PMID: 20144606.
Hunter JD. 2007. *Matplotlib: A 2D Graphics Environment*. http://dx.doi.org/10.1109/MCSE.2007.55
Inoue F, Ahituv N. 2015. Decoding enhancers using massively parallel reporter assays. *Genomics* 106: 159-64. PMID: 26072433.
Jadhav AP, Mason HA, Cepko CL. 2006. Notch 1 inhibits photoreceptor production in the developing mammalian retina. *Development* 133: 913-23. PMID: 16452096.
Jiang Y, Ding Q, Xie X, Libby RT, Lefebvre V, Gan L. 2013. Transcription factors SOX4 and SOX11 function redundantly to regulate the development of mouse retinal ganglion cells. *J Biol Chem* 288: 18429-38. PMID: 23649630.
Kaufman ML, Park KU, Goodson NB, Chew S, Bersie S, Jones KL, Lamba DA, Brzezinski JAt. 2019. Transcriptional profiling of murine retinas undergoing semi-synchronous cone photoreceptor differentiation. *Dev Biol* 453: 155-67. PMID: 31163126.
Kent WJ. 2002. BLAT--the BLAST-like alignment tool. *Genome Res* 12: 656-64. PMID: 11932250.
Kim DS, Matsuda T, Cepko CL. 2008. A core paired-type and POU homeodomain-containing transcription factor program drives retinal bipolar cell gene expression. *J Neurosci* 28: 7748-64. PMID: 18667607.
Kowalchuk AM, Maurer KA, Shoja-Taheri F, Brown NL. 2018. Requirements for Neurogenin2 during mouse postnatal retinal neurogenesis. *Dev Biol* 442: 220-35. PMID: 30048641.
Krueger F. 2015. *Trim Galore!: A wrapper tool around Cutadapt and FastQC to consistently apply quality and adapter trimming to FastQ files*. https://doi.org/10.1002/maco.200603986
Lagunas T, Jr., Plassmeyer SP, Fischer AD, Friedman RZ, Rieger MA, Selmanovic D, Sarafinovska S, Sol YK, Kasper MJ, Fass SB, Aguilar Lucero AF, An JY, Sanders SJ, Cohen BA, Dougherty JD. 2023. A Cre-dependent massively parallel reporter assay allows for cell-type specific assessment of the functional effects of non-coding elements in vivo. *Commun Biol* 6: 1151. PMID: 37953348.
Langmead B, Salzberg SL. 2012. Fast gapped-read alignment with Bowtie 2. *Nat Methods* 9: 357-9. PMID: 22388286.
Lawrence M, Huber W, Pages H, Aboyoun P, Carlson M, Gentleman R, Morgan MT, Carey VJ. 2013. Software for computing and annotating genomic ranges. *PLoS Comput Biol* 9: e1003118. PMID: 23950696.
Li H. 2018. Minimap2: pairwise alignment for nucleotide sequences. *Bioinformatics* 34: 3094-100. PMID: 29750242.
Li H, Durbin R. 2009. Fast and accurate short read alignment with Burrows-Wheeler transform. *Bioinformatics* 25: 1754-60. PMID: 19451168.

Li H, Handsaker B, Wysoker A, Fennell T, Ruan J, Homer N, Marth G, Abecasis G, Durbin R, Genome Project Data Processing S. 2009. The Sequence Alignment/Map format and SAMtools. *Bioinformatics* 25: 2078-9. PMID: 19505943.

Li S, Mo Z, Yang X, Price SM, Shen MM, Xiang M. 2004. Foxn4 controls the genesis of amacrine and horizontal cells by retinal progenitors. *Neuron* 43: 795-807. PMID: 15363391.

Liu IS, Chen JD, Ploder L, Vidgen D, van der Kooy D, Kalnins VI, McInnes RR. 1994. Developmental expression of a novel murine homeobox gene (Chx10): evidence for roles in determination of the neuroretina and inner nuclear layer. *Neuron* 13: 377-93. PMID: 7914735.

Lonfat N, Wang S, Lee C, Garcia M, Choi J, Park PJ, Cepko C. 2021. Cis-regulatory dissection of cone development reveals a broad role for Otx2 and Oc transcription factors. *Development* 148. PMID: 33929509.

Lu QR, Yuk D, Alberta JA, Zhu Z, Pawlitzky I, Chan J, McMahon AP, Stiles CD, Rowitch DH. 2000. Sonic hedgehog--regulated oligodendrocyte lineage genes encoding bHLH proteins in the mammalian central nervous system. *Neuron* 25: 317-29. PMID: 10719888.

Lunde A, Glover JC. 2020. A versatile toolbox for semi-automatic cell-by-cell object-based colocalization analysis. *Sci Rep* 10: 19027. PMID: 33149236.

Lyu P, Hoang T, Santiago CP, Thomas ED, Timms AE, Appel H, Gimmen M, Le N, Jiang L, Kim DW, Chen S, Espinoza DF, Telger AE, Weir K, Clark BS, Cherry TJ, Qian J, Blackshaw S. 2021. Gene regulatory networks controlling temporal patterning, neurogenesis, and cell-fate specification in mammalian retina. *Cell Rep* 37: 109994. PMID: 34788628.

Ma W, Wang SZ. 2006. The final fates of neurogenin2-expressing cells include all major neuron types in the mouse retina. *Mol Cell Neurosci* 31: 463-9. PMID: 16364654.

Marquardt T, Ashery-Padan R, Andrejewski N, Scardigli R, Guillemot F, Gruss P. 2001. Pax6 is required for the multipotent state of retinal progenitor cells. *Cell* 105: 43-55. PMID: 11301001.

McAfee JC, Bell JL, Krupa O, Matoba N, Stein JL, Won H. 2022. Focus on your locus with a massively parallel reporter assay. *J Neurodev Disord* 14: 50. PMID: 36085003.

McDowell GS, Hardwick LJ, Philpott A. 2014. Complex domain interactions regulate stability and activity of closely related proneural transcription factors. *Biochem Biophys Res Commun* 450: 1283-90. PMID: 24998442.

McInnes L, Healy J, Saul N, Großberger L. 2018. *UMAP: Uniform Manifold Approximation and Projection*. https://doi.org/10.21105/joss.00861

McKinney W. 2010. *Data Structures for Statistical Computing in Python*. Proceedings of the 9th Python in Science Conference. ed. S van der Walt, J Millman. 56-61. Austin, TX: SciPy.

Melnikov A, Murugan A, Zhang X, Tesileanu T, Wang L, Rogov P, Feizi S, Gnirke A, Callan CG, Jr., Kinney JB, Kellis M, Lander ES, Mikkelsen TS. 2012. Systematic dissection and optimization of inducible enhancers in human cells using a massively parallel reporter assay. *Nat Biotechnol* 30: 271-7. PMID: 22371084.

Montana CL, Myers CA, Corbo JC. 2011. Quantifying the activity of cis-regulatory elements in the mouse retina by explant electroporation. *J Vis Exp*. PMID: 21730952.

Mu X, Fu X, Beremand PD, Thomas TL, Klein WH. 2008. Gene regulation logic in retinal ganglion cell development: Isl1 defines a critical branch distinct from but overlapping with Pou4f2. *Proc Natl Acad Sci U S A* 105: 6942-7. PMID: 18460603.

Nakazaki H, Reddy AC, Mania-Farnell BL, Shen YW, Ichi S, McCabe C, George D, McLone DG, Tomita T, Mayanil CS. 2008. Key basic helix-loop-helix transcription factor genes Hes1 and Ngn2 are regulated by Pax3 during mouse embryonic development. *Dev Biol* 316: 510-23. PMID: 18308300.

Nie Z, Chen S, Kumar R, Zack DJ. 1996. RER, an evolutionarily conserved sequence upstream of the rhodopsin gene, has enhancer activity. *J Biol Chem* 271: 2667-75. PMID: 8576239.

Nishida A, Furukawa A, Koike C, Tano Y, Aizawa S, Matsuo I, Furukawa T. 2003. Otx2 homeobox gene controls retinal photoreceptor cell fate and pineal gland development. *Nat Neurosci* 6: 1255-63. PMID: 14625556.

O'Leary NA, Wright MW, Brister JR, Ciufo S, Haddad D, et al. 2016. Reference sequence (RefSeq) database at NCBI: current status, taxonomic expansion, and functional annotation. *Nucleic Acids Res* 44: D733-45. PMID: 26553804.

Oron-Karni V, Farhy C, Elgart M, Marquardt T, Remizova L, Yaron O, Xie Q, Cvekl A, Ashery-Padan R. 2008. Dual requirement for Pax6 in retinal progenitor cells. *Development* 135: 4037-47. PMID: 19004853.

Pagès H, Aboyoun P, Gentleman R, DebRoy S. 2025. *Biostrings: Efficient manipulation of biological strings*. R package version 2.76.0. https://bioconductor.org/packages/Biostrings

Perez G, Barber GP, Benet-Pages A, Casper J, Clawson H, Diekhans M, Fischer C, Gonzalez JN, Hinrichs AS, Lee CM, Nassar LR, Raney BJ, Speir ML, van Baren MJ, Vaske CJ, Haussler D, Kent WJ, Haeussler M. 2025. The UCSC Genome Browser database: 2025 update. *Nucleic Acids Res* 53: D1243-D49. PMID: 39460617.

Quinlan AR, Hall IM. 2010. BEDTools: a flexible suite of utilities for comparing genomic features. *Bioinformatics* 26: 841-2. PMID: 20110278.

Rabe BA. 2020. *Investigation of the Multiple Roles of Notch Signaling in Embryonic Retinal Development Using Novel High-Throughput Techniques.* PhD thesis. Harvard University, Cambridge, MA

Rabe BA, Cepko C. 2020. A Simple Enhancement for Gibson Isothermal Assembly. *bioRxiv*: 2020.06.14.150979. PMID.

Ramirez F, Ryan DP, Gruning B, Bhardwaj V, Kilpert F, Richter AS, Heyne S, Dundar F, Manke T. 2016. deepTools2: a next generation web server for deep-sequencing data analysis. *Nucleic Acids Res* 44: W160-5. PMID: 27079975.

Rayon T, Stamataki D, Perez-Carrasco R, Garcia-Perez L, Barrington C, Melchionda M, Exelby K, Lazaro J, Tybulewicz VLJ, Fisher EMC, Briscoe J. 2020. Species-specific pace of development is associated with differences in protein stability. *Science* 369. PMID: 32943498.

Remez LA, Onishi A, Menuchin-Lasowski Y, Biran A, Blackshaw S, Wahlin KJ, Zack DJ, Ashery-Padan R. 2017. Pax6 is essential for the generation of late-born retinal neurons and for inhibition of photoreceptor-fate during late stages of retinogenesis. *Dev Biol* 432: 140-50. PMID: 28993200.

Robinson JT, Thorvaldsdottir H, Winckler W, Guttman M, Lander ES, Getz G, Mesirov JP. 2011. Integrative genomics viewer. *Nat Biotechnol* 29: 24-6. PMID: 21221095.

Rowan S, Cepko CL. 2004. Genetic analysis of the homeodomain transcription factor Chx10 in the retina using a novel multifunctional BAC transgenic mouse reporter. *Dev Biol* 271: 388-402. PMID: 15223342.

Rowan S, Cepko CL. 2005. A POU factor binding site upstream of the Chx10 homeobox gene is required for Chx10 expression in subsets of retinal progenitor cells and bipolar cells. *Dev Biol* 281: 240-55. PMID: 15893976.

Satpathy AT, Granja JM, Yost KE, Qi Y, Meschi F, et al. 2019. Massively parallel single-cell chromatin landscapes of human immune cell development and intratumoral T cell exhaustion. *Nat Biotechnol* 37: 925-36. PMID: 31375813.

Scardigli R, Baumer N, Gruss P, Guillemot F, Le Roux I. 2003. Direct and concentration-dependent regulation of the proneural gene Neurogenin2 by Pax6. *Development* 130: 3269-81. PMID: 12783797.

Scardigli R, Schuurmans C, Gradwohl G, Guillemot F. 2001. Crossregulation between Neurogenin2 and pathways specifying neuronal identity in the spinal cord. *Neuron* 31: 203-17. PMID: 11502253.

Shekhar K, Lapan SW, Whitney IE, Tran NM, Macosko EZ, Kowalczyk M, Adiconis X, Levin JZ, Nemesh J, Goldman M, McCarroll SA, Cepko CL, Regev A, Sanes JR. 2016. Comprehensive Classification of Retinal Bipolar Neurons by Single-Cell Transcriptomics. *Cell* 166: 1308-23 e30. PMID: 27565351.

Shen SQ, Myers CA, Hughes AE, Byrne LC, Flannery JG, Corbo JC. 2016a. Massively parallel cis-regulatory analysis in the mammalian central nervous system. *Genome Res* 26: 238-55. PMID: 26576614.

Shen W, Le S, Li Y, Hu F. 2016b. SeqKit: A Cross-Platform and Ultrafast Toolkit for FASTA/Q File Manipulation. *PLoS One* 11: e0163962. PMID: 27706213.
Shibasaki K, Takebayashi H, Ikenaka K, Feng L, Gan L. 2007. Expression of the basic helix-loop-factor Olig2 in the developing retina: Olig2 as a new marker for retinal progenitors and late-born cells. *Gene Expr Patterns* 7: 57-65. PMID: 16815098.
Simmons AD, Horton S, Abney AL, Johnson JE. 2001. Neurogenin2 expression in ventral and dorsal spinal neural tube progenitor cells is regulated by distinct enhancers. *Dev Biol* 229: 327-39. PMID: 11203697.
Smith T, Heger A, Sudbery I. 2017. UMI-tools: modeling sequencing errors in Unique Molecular Identifiers to improve quantification accuracy. *Genome Res* 27: 491-99. PMID: 28100584.
Soula C, Danesin C, Kan P, Grob M, Poncet C, Cochard P. 2001. Distinct sites of origin of oligodendrocytes and somatic motoneurons in the chick spinal cord: oligodendrocytes arise from Nkx2.2-expressing progenitors by a Shh-dependent mechanism. *Development* 128: 1369-79. PMID: 11262237.
Sun C, Ruzycki PA, Chen S. 2023. Rho enhancers play unexpectedly minor roles in Rhodopsin transcription and rod cell integrity. *Sci Rep* 13: 12899. PMID: 37558693.
Sun T, Hafler BP, Kaing S, Kitada M, Ligon KL, Widlund HR, Yuk DI, Stiles CD, Rowitch DH. 2006. Evidence for motoneuron lineage-specific regulation of Olig2 in the vertebrate neural tube. *Dev Biol* 292: 152-64. PMID: 16469306.
Tareen A, Kinney JB. 2020. Logomaker: beautiful sequence logos in Python. *Bioinformatics* 36: 2272-74. PMID: 31821414.
Thorvaldsdottir H, Robinson JT, Mesirov JP. 2013. Integrative Genomics Viewer (IGV): high-performance genomics data visualization and exploration. *Brief Bioinform* 14: 178-92. PMID: 22517427.
Trimarchi JM, Stadler MB, Cepko CL. 2008. Individual retinal progenitor cells display extensive heterogeneity of gene expression. *PLoS One* 3: e1588. PMID: 18270576.
Tulloch A. 2025. *LS-MPRA / d-MPRA Data Repository*. Harvard Dataverse. Draft Version. https://doi.org/10.7910/DVN/TW0ZQL
Ueda Y, Iwakabe H, Masu M, Suzuki M, Nakanishi S. 1997. The mGluR6 5' upstream transgene sequence directs a cell-specific and developmentally regulated expression in retinal rod and ON-type cone bipolar cells. *J Neurosci* 17: 3014-23. PMID: 9096137.
van der Loo MPJ. 2014. *The stringdist package for approximate string matching*. The R Journal. https://doi.org/10.32614/RJ-2014-011
Vosper JM, Fiore-Heriche CS, Horan I, Wilson K, Wise H, Philpott A. 2007. Regulation of neurogenin stability by ubiquitin-mediated proteolysis. *Biochem J* 407: 277-84. PMID: 17623011.
Wang S, Sengel C, Emerson MM, Cepko CL. 2014. A gene regulatory network controls the binary fate decision of rod and bipolar cells in the vertebrate retina. *Dev Cell* 30: 513-27. PMID: 25155555.
Wickham H. 2016. *ggplot2: Elegant Graphics for Data Analysis*. New York: Springer-Verlag.
Yaron O, Farhy C, Marquardt T, Applebury M, Ashery-Padan R. 2006. Notch1 functions to suppress cone-photoreceptor fate specification in the developing mouse retina. *Development* 133: 1367-78. PMID: 16510501.
Young RW. 1985. Cell differentiation in the retina of the mouse. *Anat Rec* 212: 199-205. PMID: 3842042.
Zack DJ, Bennett J, Wang Y, Davenport C, Klaunberg B, Gearhart J, Nathans J. 1991. Unusual topography of bovine rhodopsin promoter-lacZ fusion gene expression in transgenic mouse retinas. *Neuron* 6: 187-99. PMID: 1899580.
Zhang J, Roberts JM, Chang F, Schwakopf J, Vetter ML. 2023. Jarid2 promotes temporal progression of retinal progenitors via repression of Foxp1. *Cell Rep* 42: 112237. PMID: 36924502.
Zhang Q, Zagozewski J, Cheng S, Dixit R, Zhang S, de Melo J, Mu X, Klein WH, Brown NL, Wigle JT, Schuurmans C, Eisenstat DD. 2017. Regulation of Brn3b by DLX1 and DLX2 is required for

retinal ganglion cell differentiation in the vertebrate retina. *Development* 144: 1698-711. PMID: 28356311.

Zhang Y, Liu T, Meyer CA, Eeckhoute J, Johnson DS, Bernstein BE, Nusbaum C, Myers RM, Brown M, Li W, Liu XS. 2008. Model-based analysis of ChIP-Seq (MACS). *Genome Biol* 9: R137. PMID: 18798982.

Zhou Q, Wang S, Anderson DJ. 2000. Identification of a novel family of oligodendrocyte lineage-specific basic helix-loop-helix transcription factors. *Neuron* 25: 331-43. PMID: 10719889.

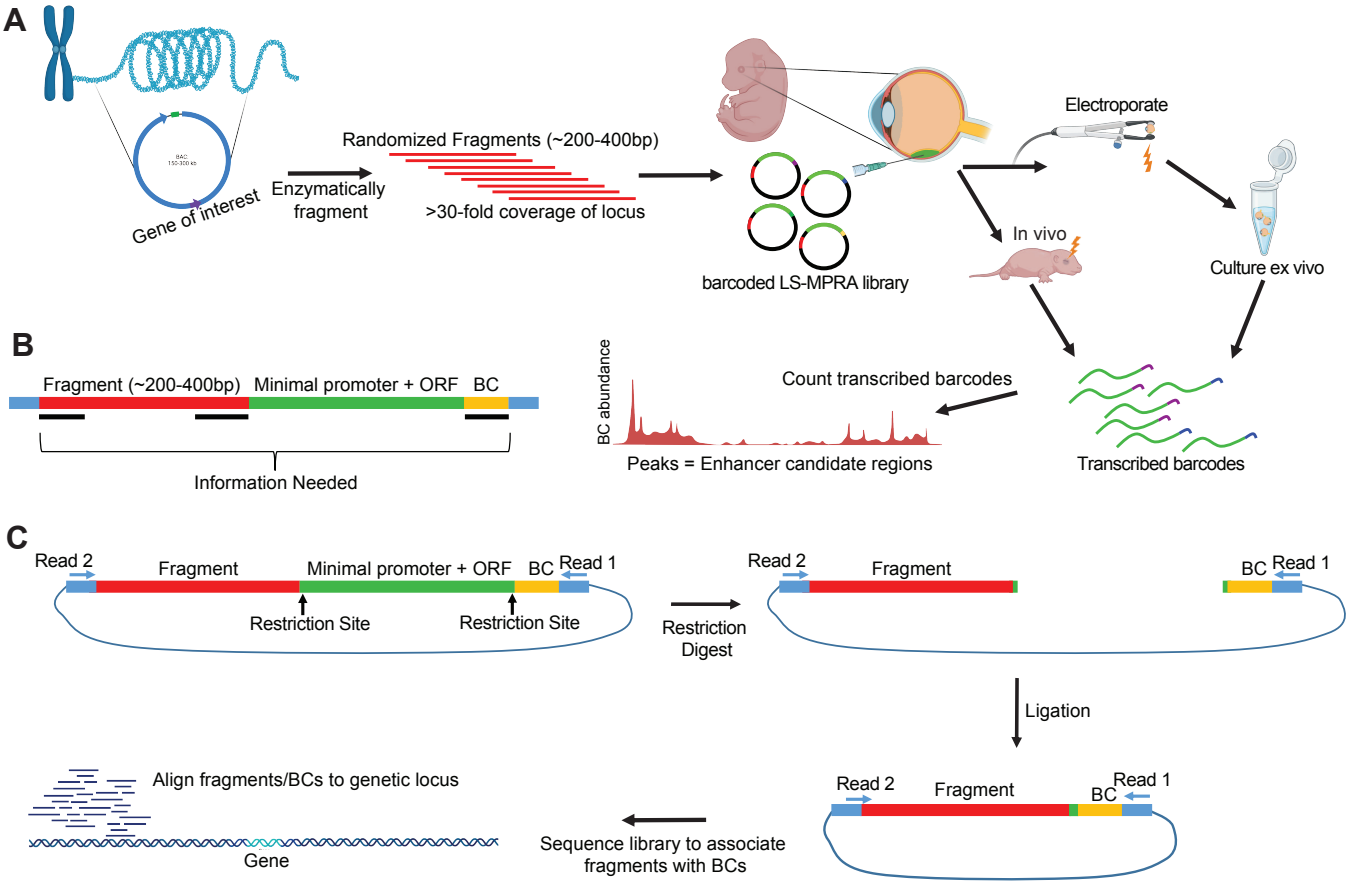
A
Gene of interest
Enzymatically fragment
Randomized Fragments (~200-400bp)
>30-fold coverage of locus
barcoded LS-MPRA library
Electroporate
In vivo
Culture ex vivo
Transcribed barcodes
Count transcribed barcodes
BC abundance
Peaks = Enhancer candidate regions
B
Fragment (~200-400bp)
Minimal promoter + ORF
BC
Information Needed
C
Read 2
Fragment
Minimal promoter + ORF
BC
Read 1
Restriction Site
Restriction Site
Restriction Digest
Ligation
Align fragments/BCs to genetic locus
Gene
Sequence library to associate fragments with BCs

Fig.1

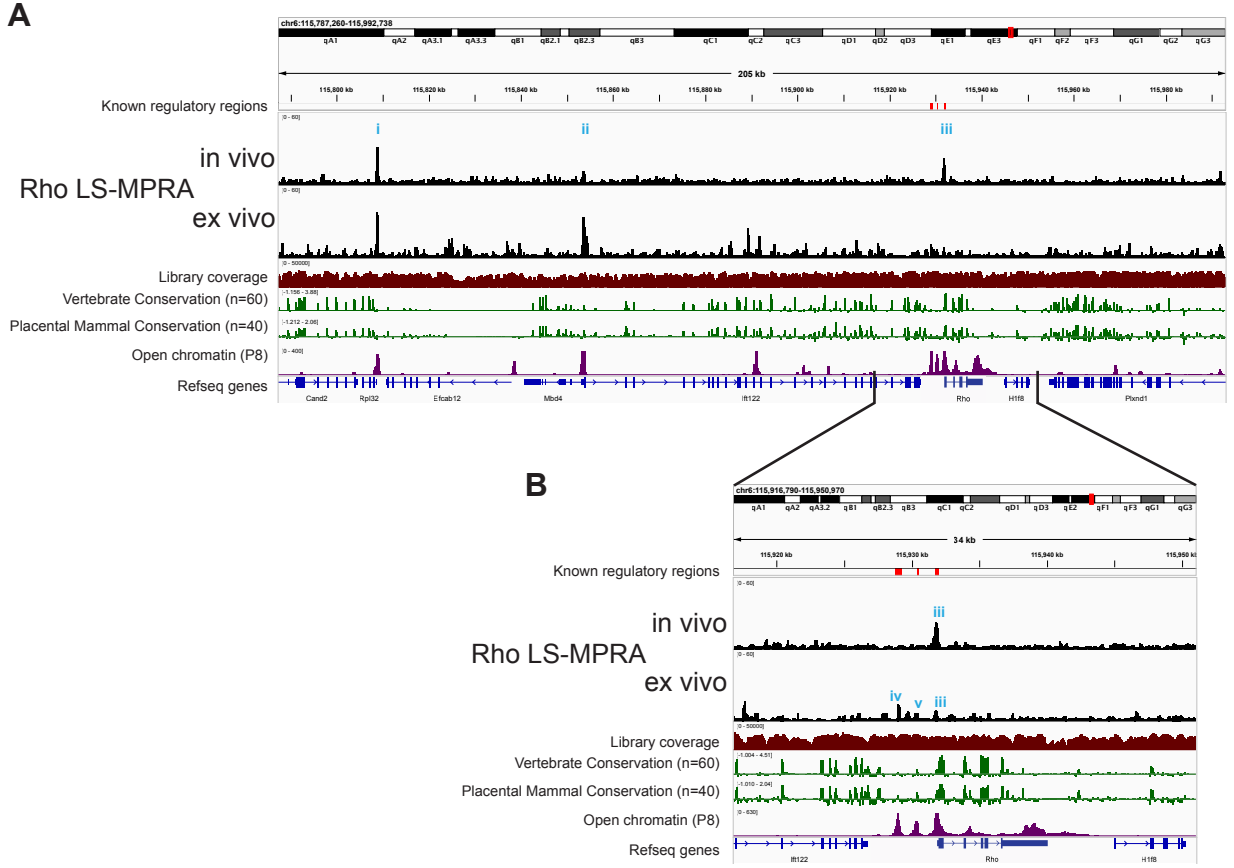
A
chr6:115,787,260-115,992,738
205 kb
Known regulatory regions
i
ii
iii
in vivo
Rho LS-MPRA
ex vivo
Library coverage
Vertebrate Conservation (n=60)
Placental Mammal Conservation (n=40)
Open chromatin (P8)
Refseq genes
Cand2
Rpl32
Efcab12
Mbd4
Ift122
Rho
H1f8
Plxnd1
B
chr6:115,916,790-115,950,970
34 kb
Known regulatory regions
iii
in vivo
Rho LS-MPRA
ex vivo
iv
v
iii
Library coverage
Vertebrate Conservation (n=60)
Placental Mammal Conservation (n=40)
Open chromatin (P8)
Refseq genes
Ift122
Rho
H1f8

Fig.2

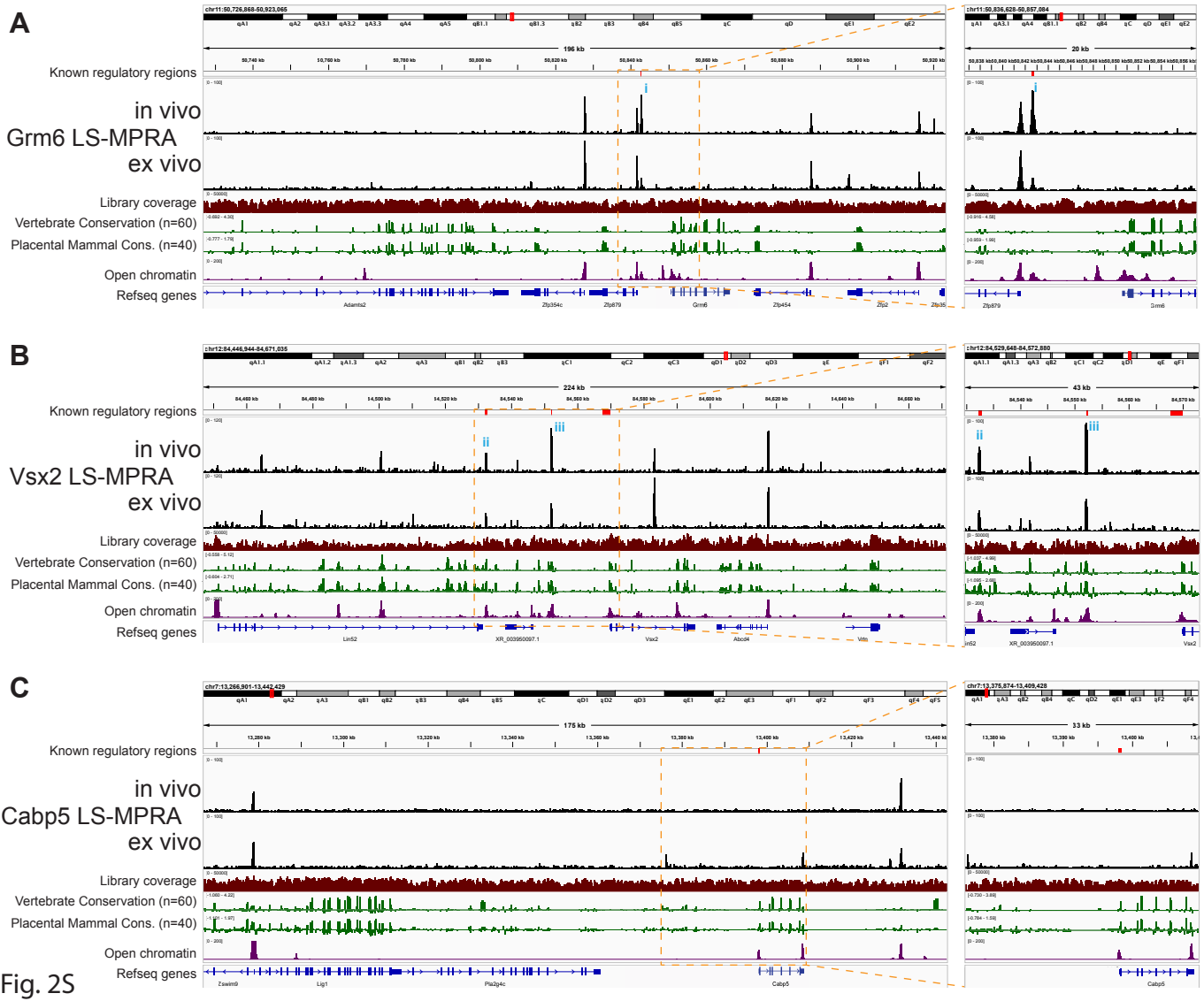
A
Known regulatory regions
in vivo
Grm6 LS-MPRA
ex vivo
Library coverage
Vertebrate Conservation (n=60)
Placental Mammal Cons. (n=40)
Open chromatin
Refseq genes
B
Known regulatory regions
in vivo
Vsx2 LS-MPRA
ex vivo
Library coverage
Vertebrate Conservation (n=60)
Placental Mammal Cons. (n=40)
Open chromatin
Refseq genes
C
Known regulatory regions
in vivo
Cabp5 LS-MPRA
ex vivo
Library coverage
Vertebrate Conservation (n=60)
Placental Mammal Cons. (n=40)
Open chromatin
Refseq genes

Fig. 2S

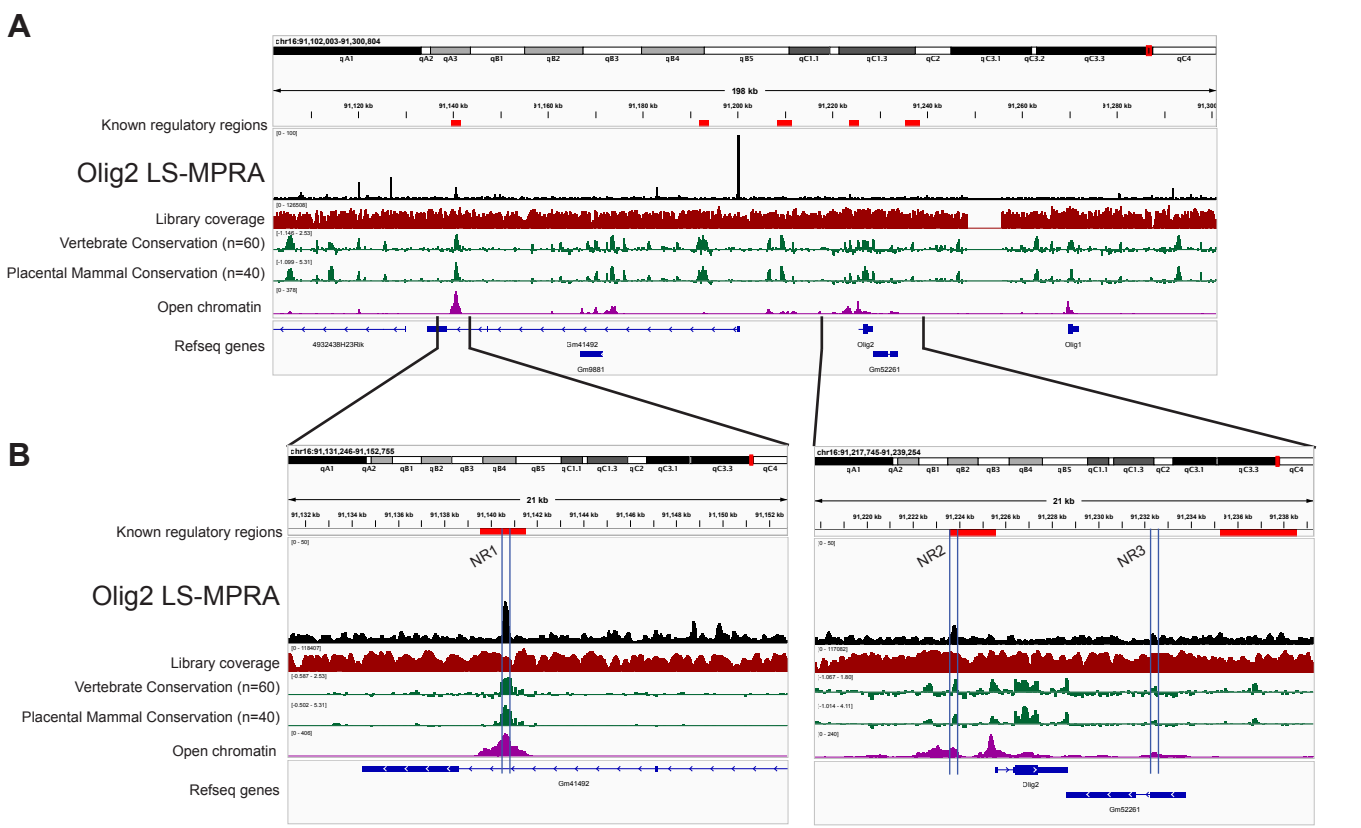
A
chr16:91,102,003-91,300,804
198 kb
Known regulatory regions
Olig2 LS-MPRA
Library coverage
Vertebrate Conservation (n=60)
Placental Mammal Conservation (n=40)
Open chromatin
Refseq genes
4932438H23Rik
Gm41492
Olig2
Olig1
Gm9881
Gm52261
B
chr16:91,131,246-91,152,755
21 kb
NR1
chr16:91,217,745-91,239,254
NR2
NR3

Fig. 3

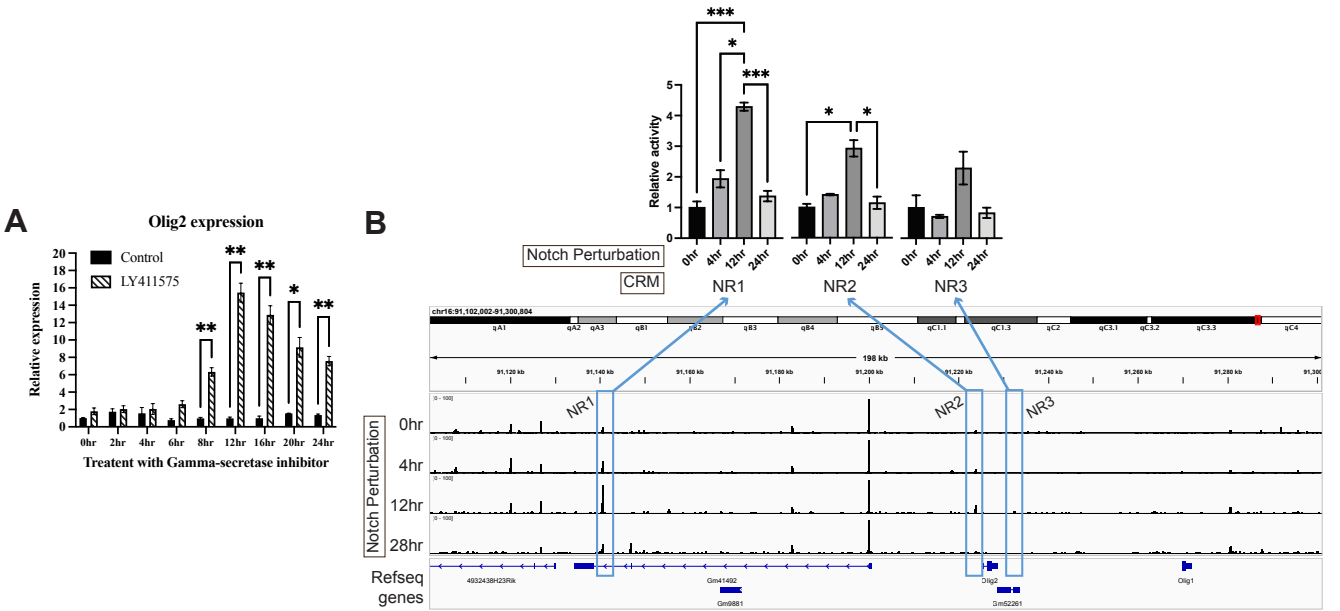
A
Olig2 expression
Control
LY411575
Relative expression
Treatent with Gamma-secretase inhibitor
0hr
2hr
4hr
6hr
8hr
12hr
16hr
20hr
24hr
B
Relative activity
Notch Perturbation
CRM
NR1
NR2
NR3
chr16:91,102,002-91,300,804
198 kb
Notch Perturbation
0hr
4hr
12hr
28hr
Refseq genes
4932438H23Rik
Gm41492
Gm9881
Olig2
Olig1
Gm52261

Fig. 4

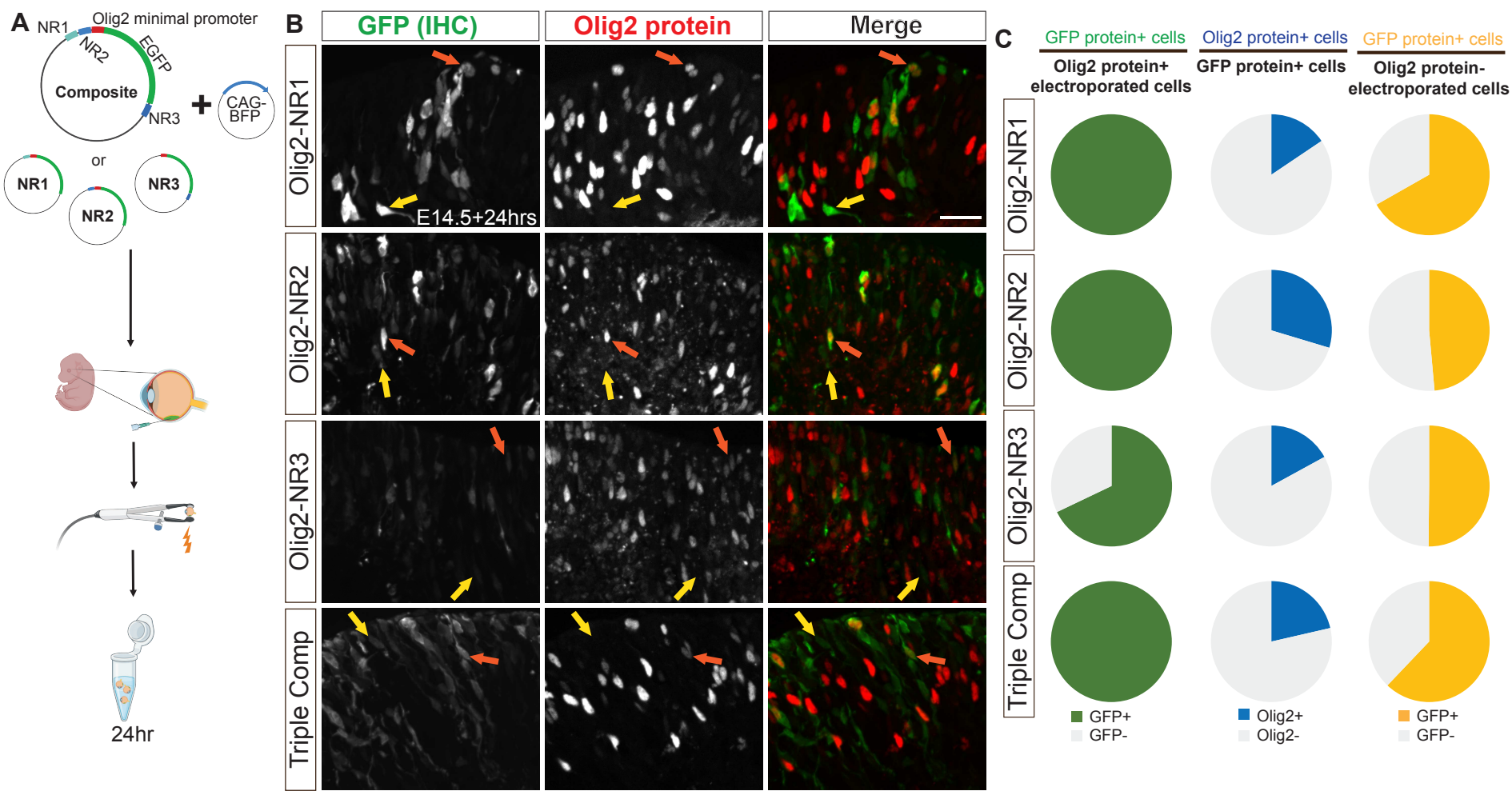
A
NR1
Olig2 minimal promoter
NR2
EGFP
Composite
NR3
CAG-BFP
or
NR1
NR2
NR3
24hr
B
GFP (IHC)
Olig2 protein
Merge
Olig2-NR1
Olig2-NR2
Olig2-NR3
Triple Comp
E14.5+24hrs
C
GFP protein+ cells
Olig2 protein+ electroporated cells
Olig2 protein+ cells
GFP protein+ cells
GFP protein+ cells
Olig2 protein- electroporated cells
Olig2-NR1
Olig2-NR2
Olig2-NR3
Triple Comp
GFP+
GFP-
Olig2+
Olig2-
GFP+
GFP-

Fig. 5

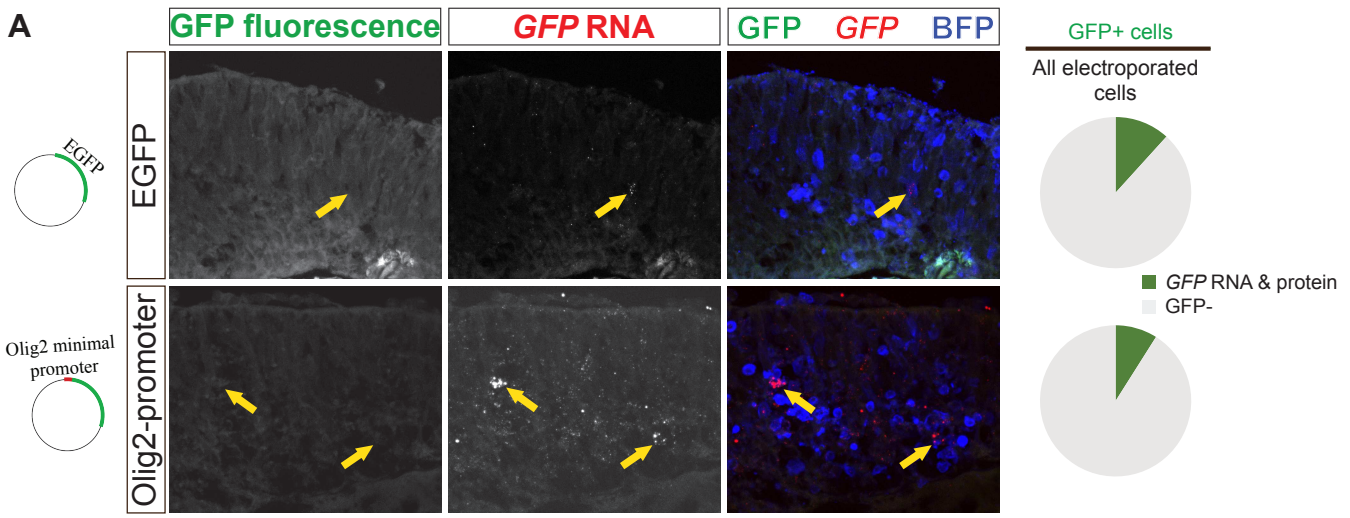
A
GFP fluorescence
GFP RNA
GFP GFP BFP
EGFP
Olig2 minimal promoter
EGFP
Olig2-promoter
GFP+ cells
All electroporated cells
GFP RNA & protein
GFP-

Fig. 5S

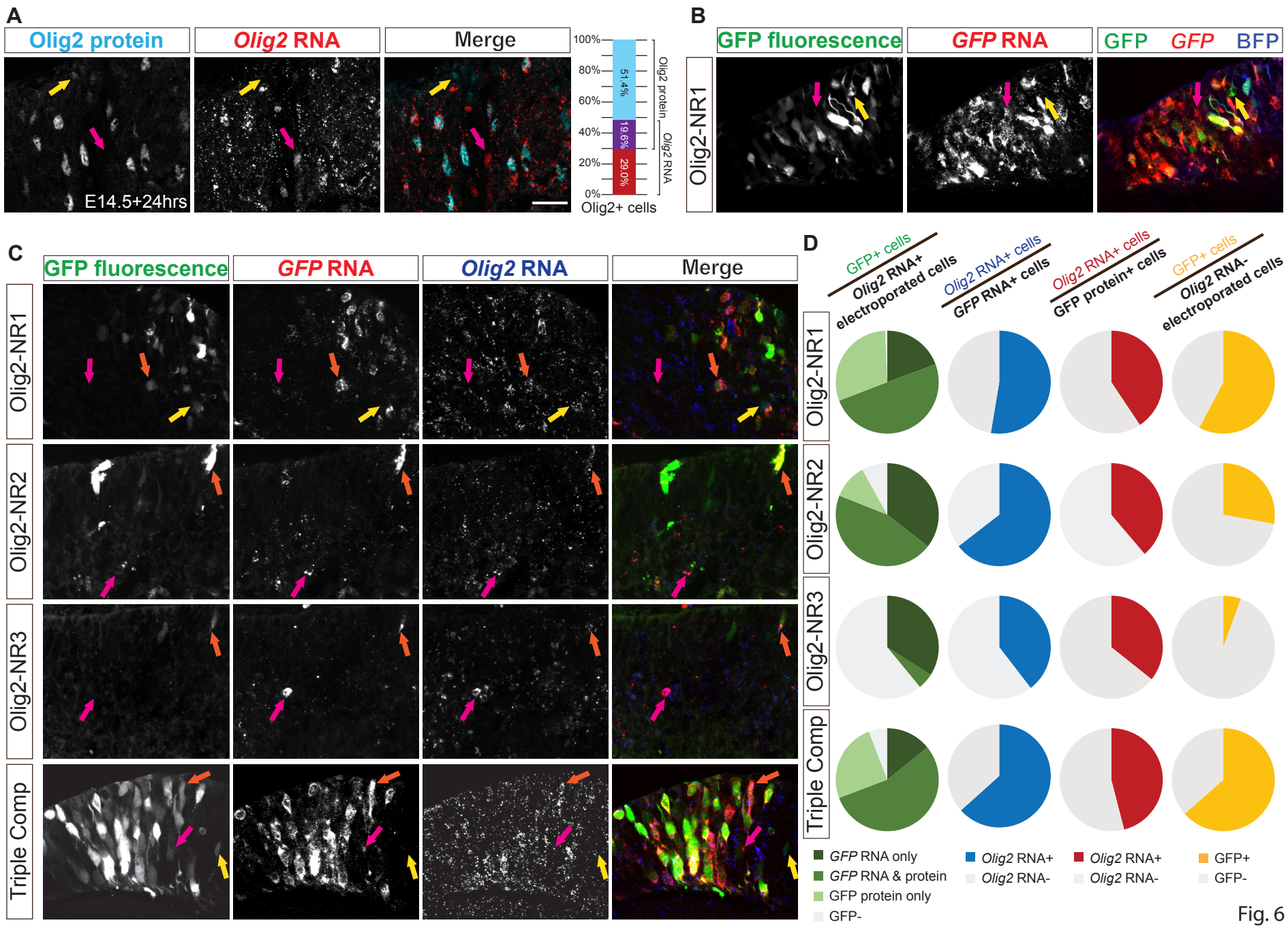
A
Olig2 protein
Olig2 RNA
Merge
E14.5+24hrs
100%
80%
60%
40%
20%
0%
51.4%
19.6%
29.0%
Olig2 protein
Olig2 RNA
Olig2+ cells
B
GFP fluorescence
GFP RNA
GFP GFP BFP
Olig2-NR1
C
GFP fluorescence
GFP RNA
Olig2 RNA
Merge
Olig2-NR1
Olig2-NR2
Olig2-NR3
Triple Comp
D
GFP+ cells
Olig2 RNA+ electroporated cells
Olig2 RNA+ cells
GFP RNA+ cells
Olig2 RNA+ cells
GFP protein+ cells
GFP+ cells
Olig2 RNA- electroporated cells
Olig2-NR1
Olig2-NR2
Olig2-NR3
Triple Comp
GFP RNA only
GFP RNA & protein
GFP protein only
GFP-
Olig2 RNA+
Olig2 RNA-
Olig2 RNA+
Olig2 RNA-
GFP+
GFP-

Fig. 6

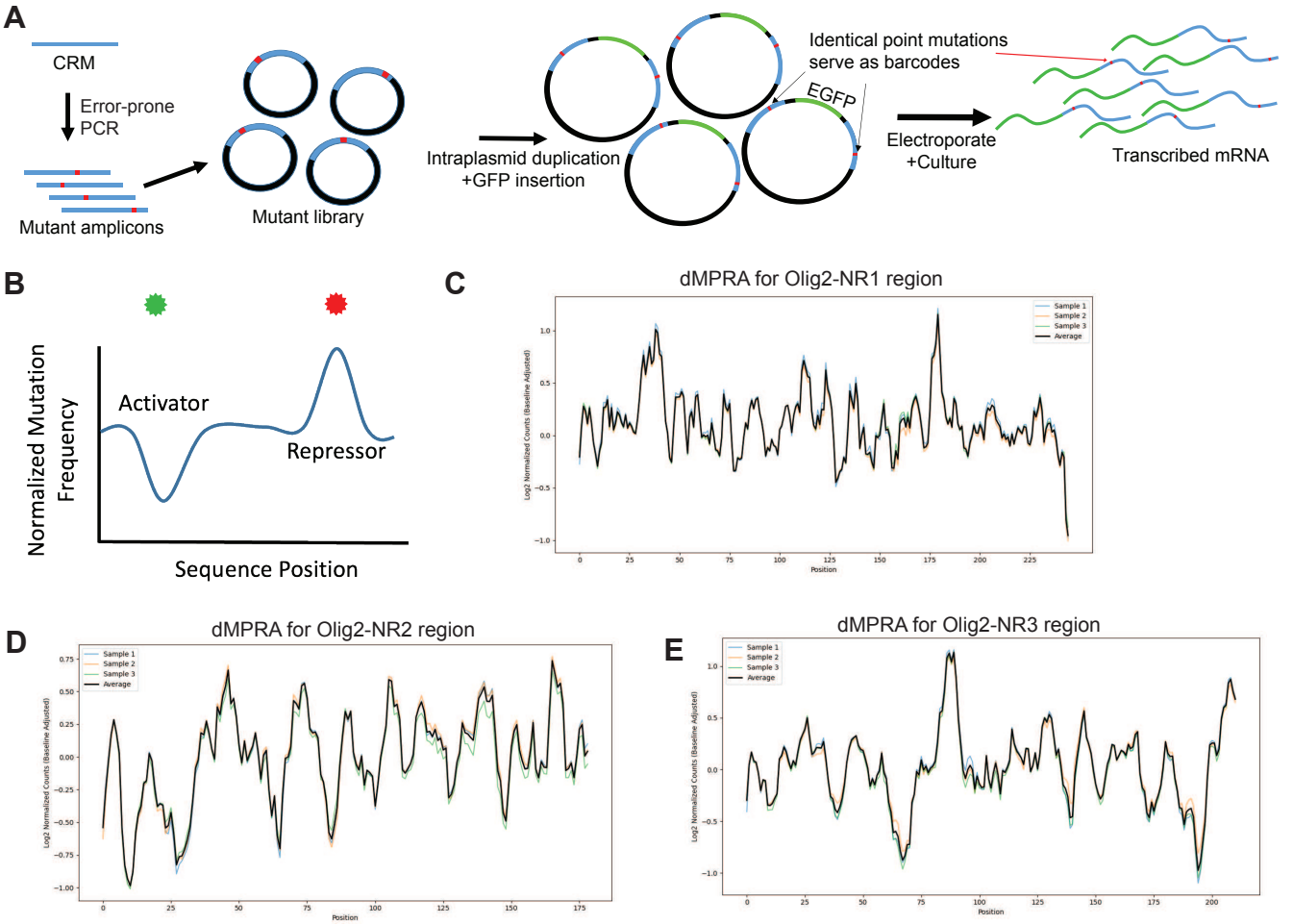
A
CRM
Error-prone PCR
Mutant amplicons
Mutant library
Intraplasmid duplication +GFP insertion
EGFP
Identical point mutations serve as barcodes
Electroporate +Culture
Transcribed mRNA
B
Normalized Mutation Frequency
Activator
Repressor
Sequence Position
C
dMPRA for Olig2-NR1 region
Sample 1
Sample 2
Sample 3
Average
Log2 Normalized Counts (Baseline Adjusted)
Position
D
dMPRA for Olig2-NR2 region
E
dMPRA for Olig2-NR3 region

Fig. 7

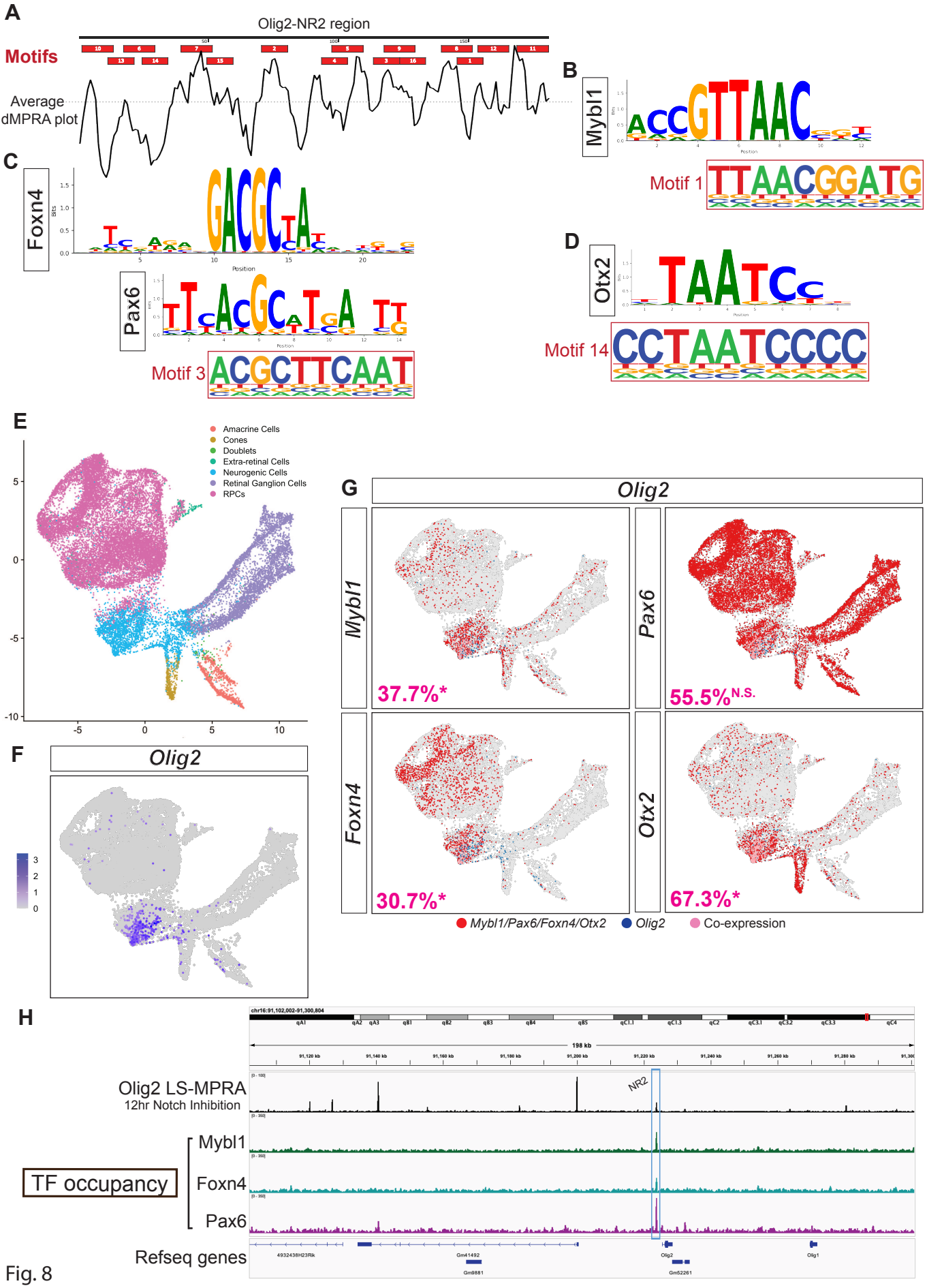
A
Olig2-NR2 region
Motifs
Average dMPRA plot
B
Mybl1
Motif 1
C
Foxn4
Pax6
Motif 3
D
Otx2
Motif 14
E
Amacrine Cells
Cones
Doublets
Extra-retinal Cells
Neurogenic Cells
Retinal Ganglion Cells
RPCs
F
Olig2
G
Olig2
Mybl1
Pax6
Foxn4
Otx2
37.7%*
55.5%N.S.
30.7%*
67.3%*
Mybl1/Pax6/Foxn4/Otx2
Olig2
Co-expression
H
Olig2 LS-MPRA
12hr Notch Inhibition
NR2
TF occupancy
Mybl1
Foxn4
Pax6
Refseq genes

Fig. 8

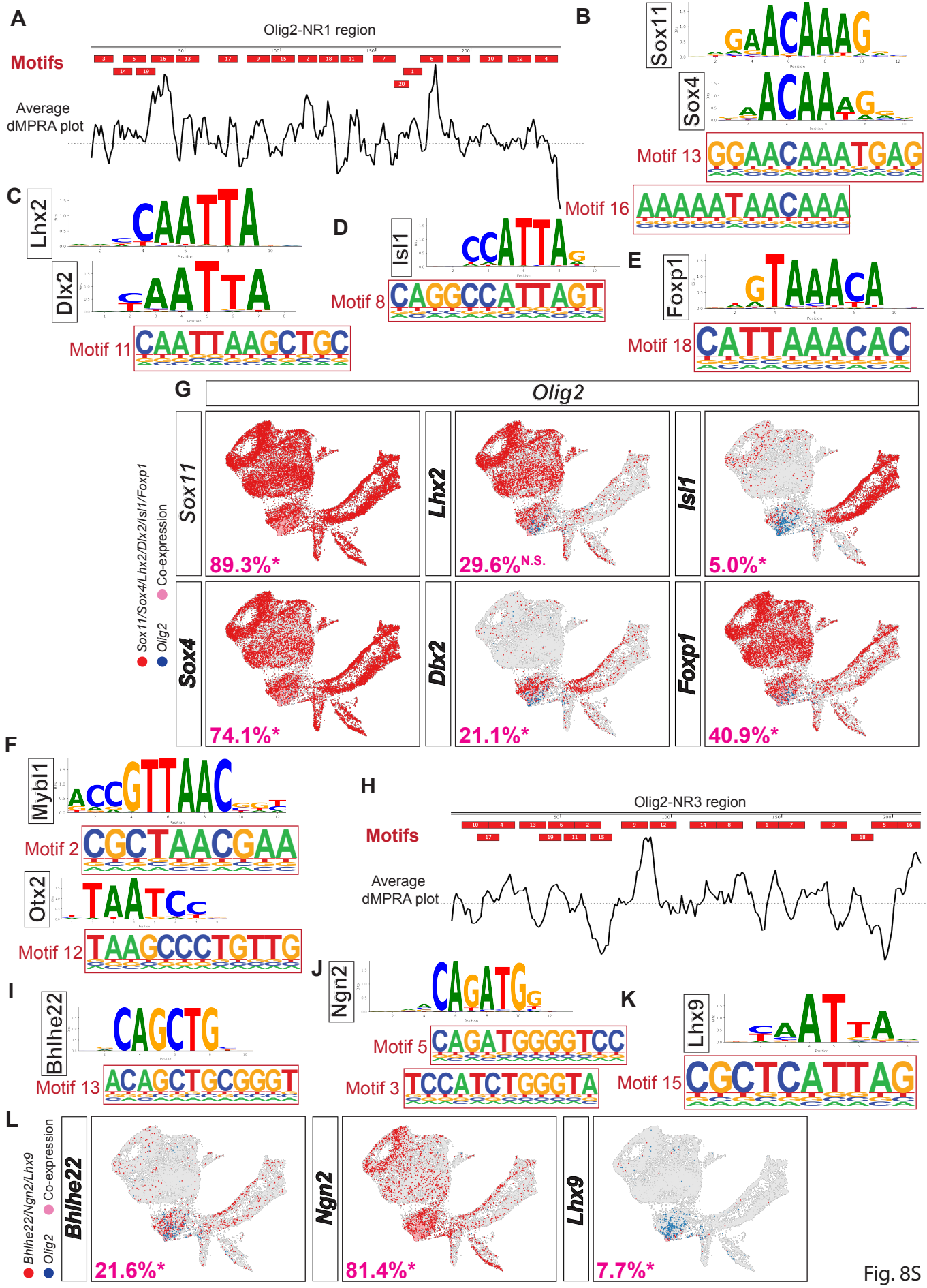
A
Olig2-NR1 region
Motifs
Average dMPRA plot
B
Sox11
Sox4
Motif 13
Motif 16
C
Lhx2
Dlx2
Motif 11
D
Isl1
Motif 8
E
Foxp1
Motif 18
G
Olig2
Sox11/Sox4/Lhx2/Dlx2/Isl1/Foxp1
Co-expression
Olig2
Sox11
89.3%*
Lhx2
29.6%N.S.
Isl1
5.0%*
Sox4
74.1%*
Dlx2
21.1%*
Foxp1
40.9%*
F
Mybl1
Motif 2
Otx2
Motif 12
H
Olig2-NR3 region
Motifs
Average dMPRA plot
I
Bhlhe22
Motif 13
J
Ngn2
Motif 5
Motif 3
K
Lhx9
Motif 15
L
Bhlhe22/Ngn2/Lhx9
Co-expression
Olig2
Bhlhe22
21.6%*
Ngn2
81.4%*
Lhx9
7.7%*

Fig. 8S

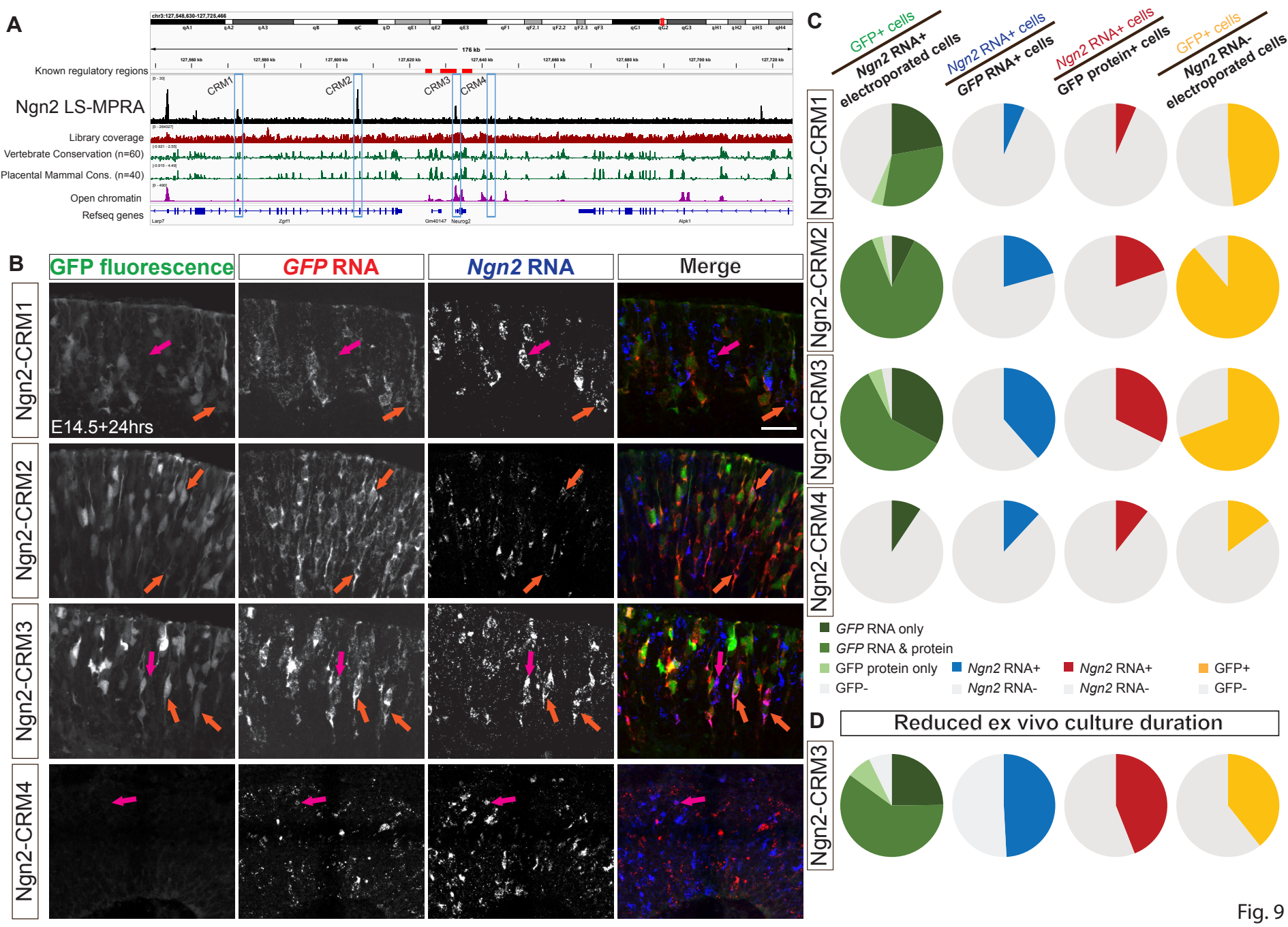
A
Known regulatory regions
Ngn2 LS-MPRA
Library coverage
Vertebrate Conservation (n=60)
Placental Mammal Cons. (n=40)
Open chromatin
Refseq genes
CRM1
CRM2
CRM3
CRM4
B
GFP fluorescence
GFP RNA
Ngn2 RNA
Merge
Ngn2-CRM1
Ngn2-CRM2
Ngn2-CRM3
Ngn2-CRM4
E14.5+24hrs
C
GFP+ cells
Ngn2 RNA+ electroporated cells
Ngn2 RNA+ cells
GFP RNA+ cells
Ngn2 RNA+ cells
GFP protein+ cells
GFP+ cells
Ngn2 RNA- electroporated cells
GFP RNA only
GFP RNA & protein
GFP protein only
GFP-
Ngn2 RNA+
Ngn2 RNA-
Ngn2 RNA+
Ngn2 RNA-
GFP+
GFP-
D
Reduced ex vivo culture duration

Fig. 9

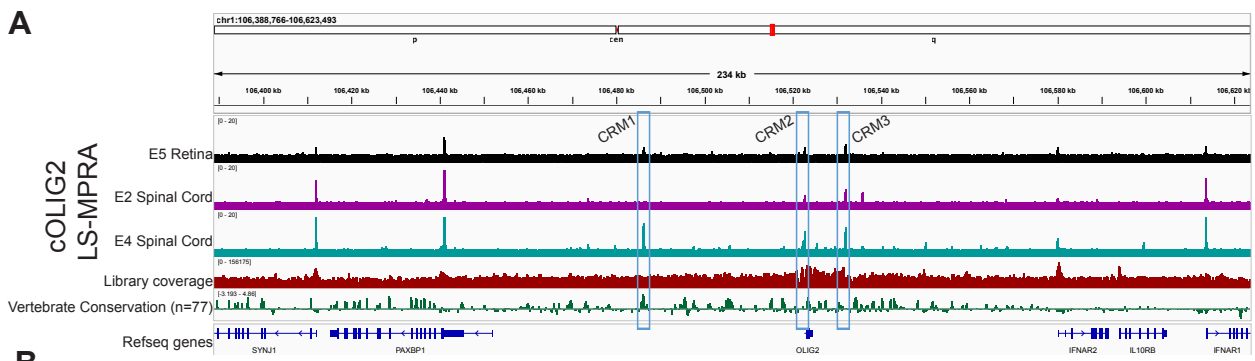
A
chr1:106,388,766-106,623,493
234 kb
CRM1
CRM2
CRM3
cOLIG2 LS-MPRA
E5 Retina
E2 Spinal Cord
E4 Spinal Cord
Library coverage
Vertebrate Conservation (n=77)
Refseq genes
SYNJ1
PAXBP1
OLIG2
IFNAR2
IL10RB
IFNAR1

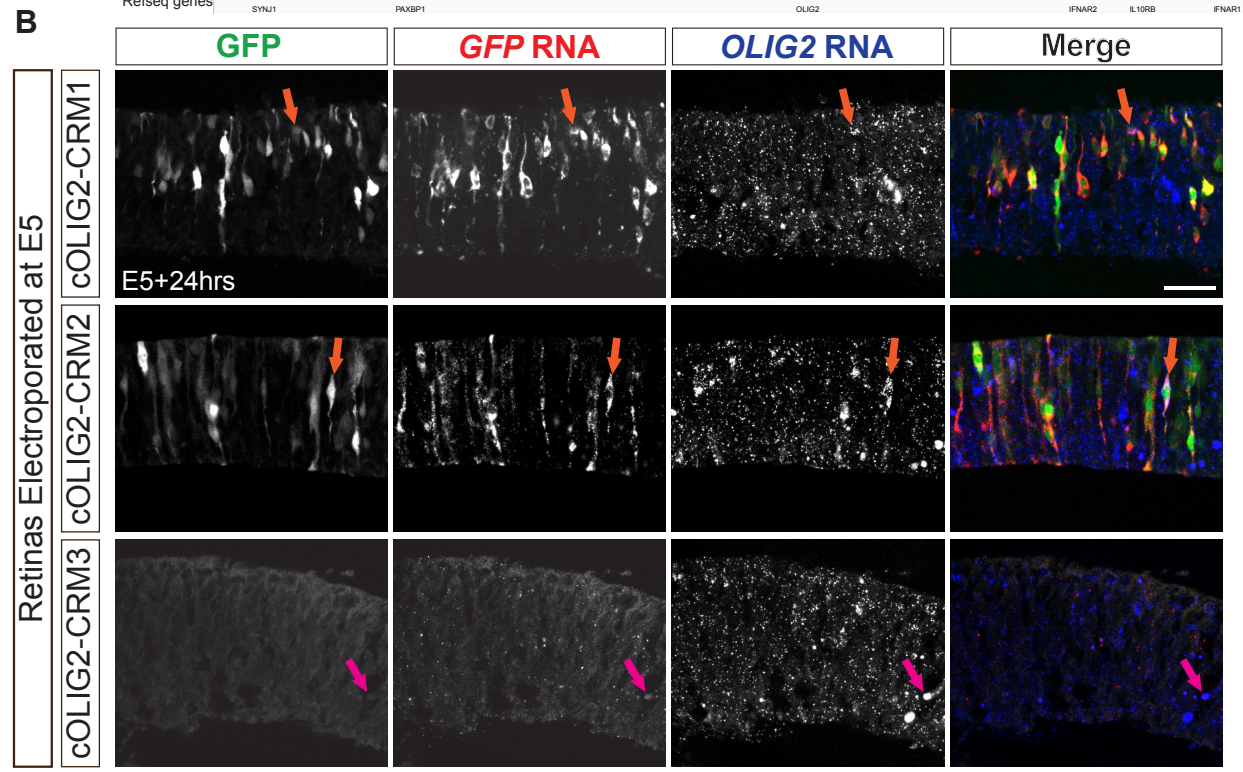
B
GFP
GFP RNA
OLIG2 RNA
Merge
Retinas Electroporated at E5
cOLIG2-CRM1
cOLIG2-CRM2
cOLIG2-CRM3
E5+24hrs

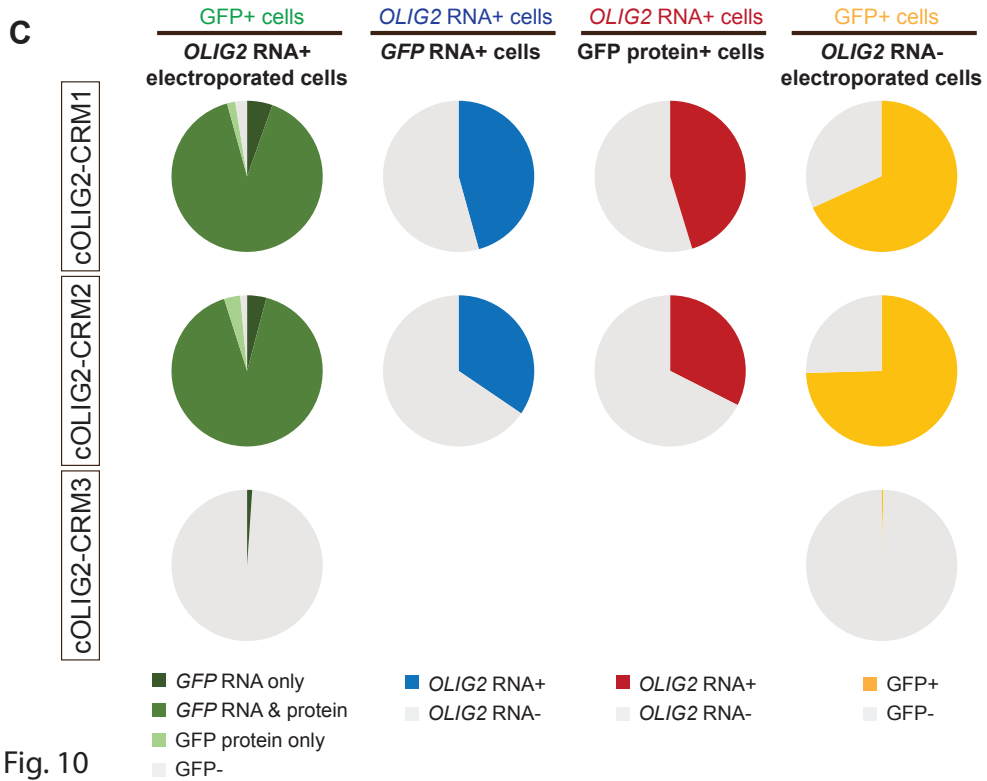
C
GFP+ cells
OLIG2 RNA+ electroporated cells
OLIG2 RNA+ cells
GFP RNA+ cells
OLIG2 RNA+ cells
GFP protein+ cells
GFP+ cells
OLIG2 RNA- electroporated cells
cOLIG2-CRM1
cOLIG2-CRM2
cOLIG2-CRM3
GFP RNA only
GFP RNA & protein
GFP protein only
GFP-
OLIG2 RNA+
OLIG2 RNA-
OLIG2 RNA+
OLIG2 RNA-
GFP+
GFP-

Fig. 10

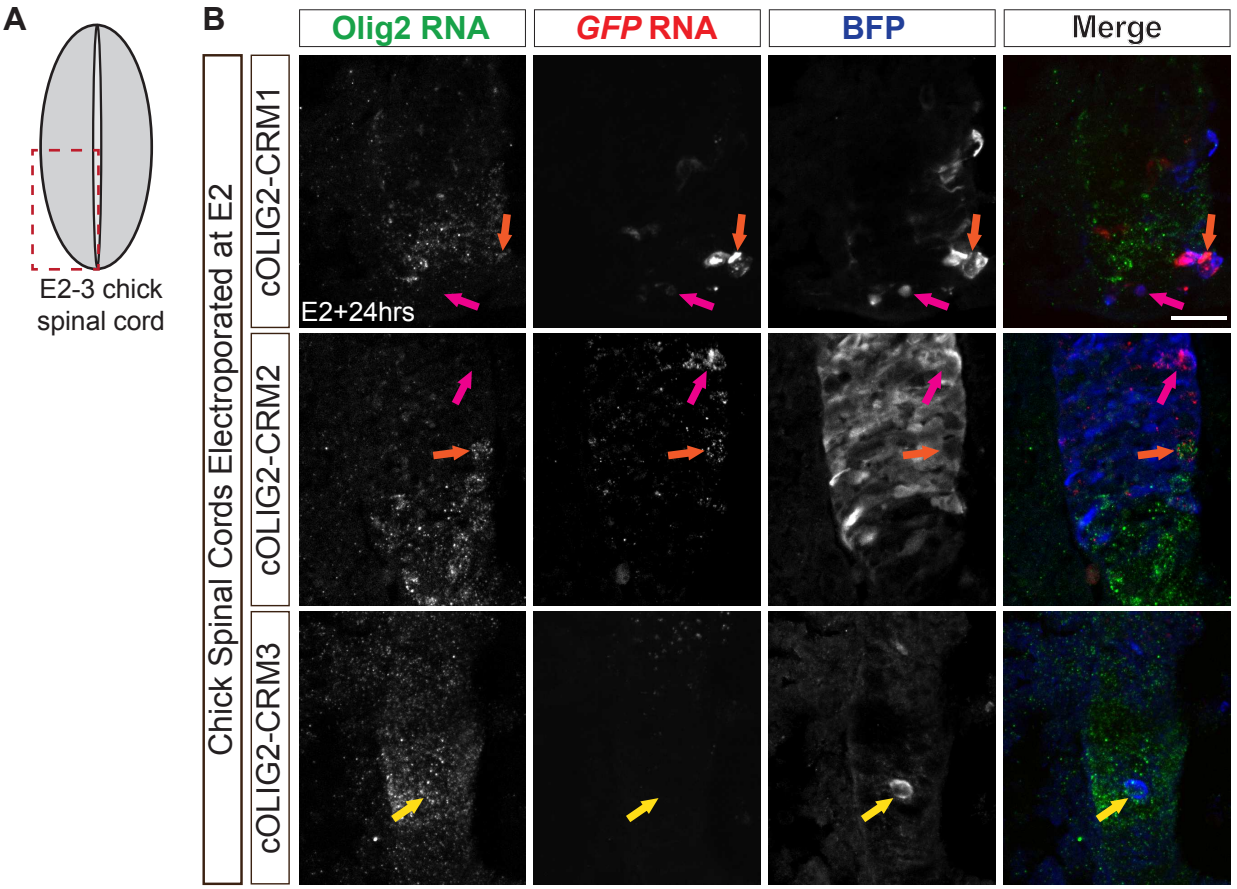
A
E2-3 chick
spinal cord
B
Olig2 RNA
GFP RNA
BFP
Merge
Chick Spinal Cords Electroporated at E2
cOLIG2-CRM1
cOLIG2-CRM2
cOLIG2-CRM3
E2+24hrs

Fig. 10S

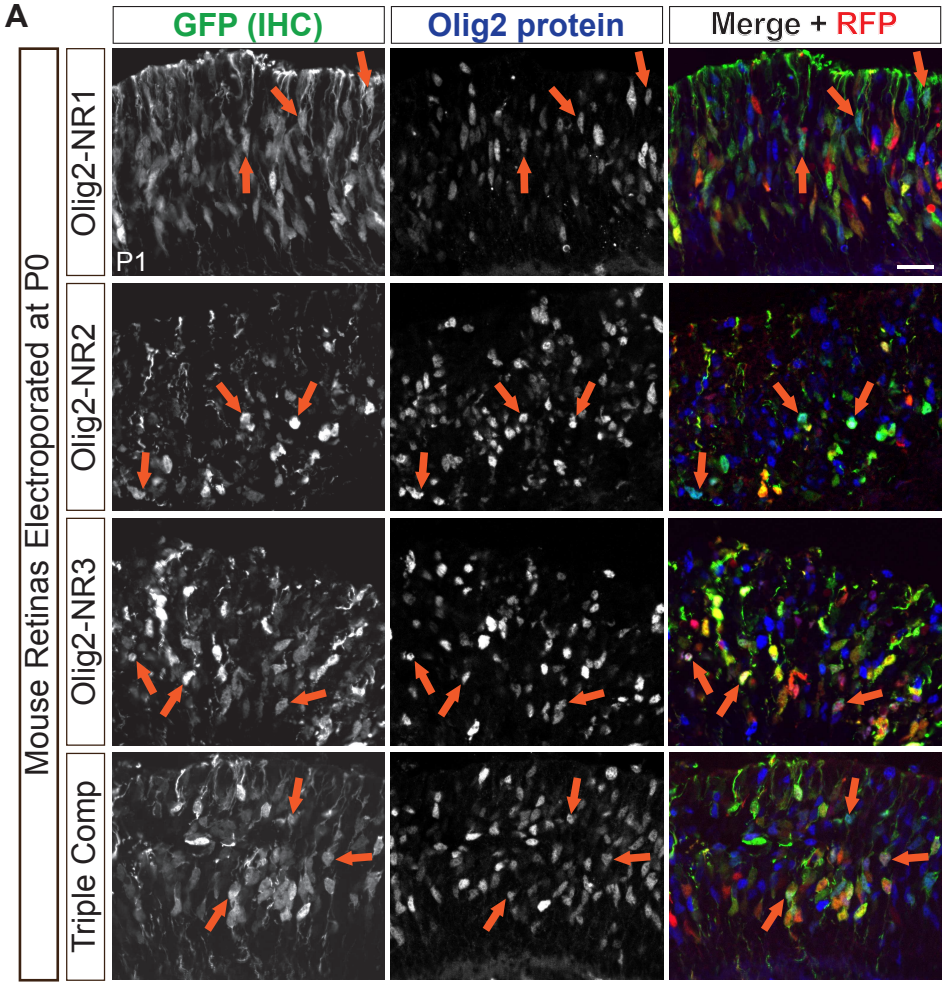
A
GFP (IHC)
Olig2 protein
Merge + RFP
Mouse Retinas Electroporated at P0
Olig2-NR1
Olig2-NR2
Olig2-NR3
Triple Comp
P1

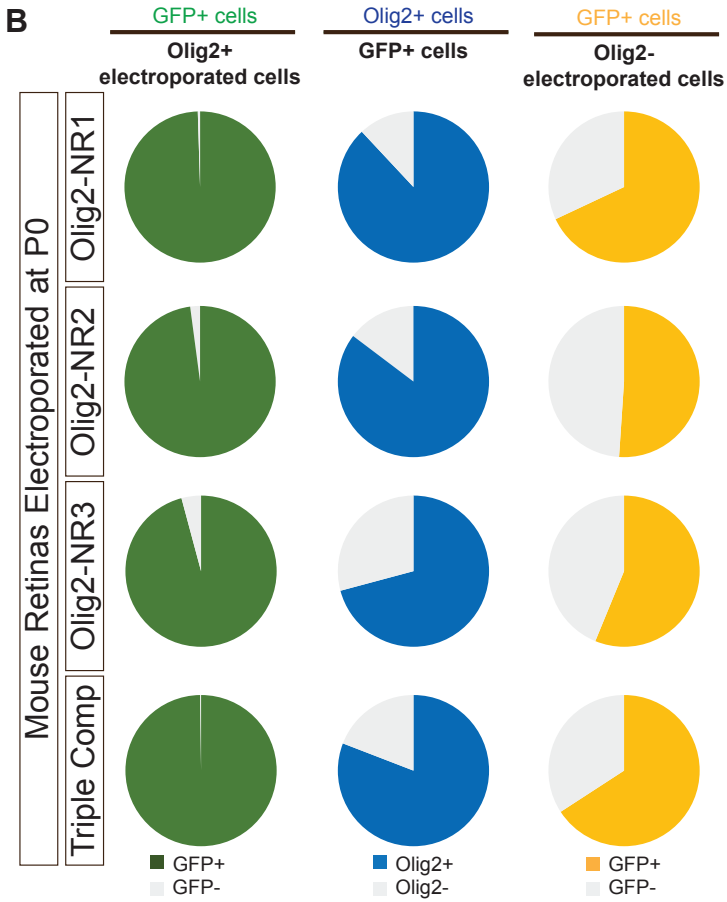
B
GFP+ cells
Olig2+ electroporated cells
Olig2+ cells
GFP+ cells
GFP+ cells
Olig2- electroporated cells
Mouse Retinas Electroporated at P0
Olig2-NR1
Olig2-NR2
Olig2-NR3
Triple Comp
GFP+
GFP-
Olig2+
Olig2-
GFP+
GFP-

Fig. 11

Table S1. Primer sequences		
Method	**Primer Name**	**Sequence**
Stagintbc7 vector design	bc7_ins1	GGCGCGCCaGATCGGAAGAGCACACGTCTGAACTCCAGTCACCCTTACTTGTACAGCTCGTCCATG
	bc7_ins2	CCGATCtGGCGCGCCSWSWSWSWSWSWSWSWSWSWSWaGATCGGAAGAGCGTCGTGTAGGGAAAGAGTGTCCGGCCCCTTGAGCATCT
	bc7_ins1A	GCCTGTATGGCGCGCCaGATCGGAAGAGCACACGTCTGAACTCCAGTCACCCTTACTTGTACAGCTCGTCCATG
	bc7_ins1B	CTTGCACAGGCGCGCCaGATCGGAAGAGCACACGTCTGAACTCCAGTCACCCTTACTTGTACAGCTCGTCCATG
	bc7_ins1C	TCTTCGTGGGCGCGCCaGATCGGAAGAGCACACGTCTGAACTCCAGTCACCCTTACTTGTACAGCTCGTCCATG
	bc7_ins1D	AGGTTCACGGCGCGCCaGATCGGAAGAGCACACGTCTGAACTCCAGTCACCCTTACTTGTACAGCTCGTCCATG
	bc7_ins2A	CCGATCtGGCGCGCCATACAGGCVHBDVHBDVHBDVHBDVHBDVHBDaGATCGGAAGAGCGTCGTGTAGGGAAAGAGTGTCCGGCCCCTTGAGCATCT
	bc7_ins2B	CCGATCtGGCGCGCCTGTGCAAGVHBDVHBDVHBDVHBDVHBDVHBDaGATCGGAAGAGCGTCGTGTAGGGAAAGAGTGTCCGGCCCCTTGAGCATCT
	bc7_ins2C	CCGATCtGGCGCGCCCACGAAGAVHBDVHBDVHBDVHBDVHBDVHBDaGATCGGAAGAGCGTCGTGTAGGGAAAGAGTGTCCGGCCCCTTGAGCATCT
	bc7_ins2D	CCGATCtGGCGCGCCGTGAACCTVHBDVHBDVHBDVHBDVHBDVHBDaGATCGGAAGAGCGTCGTGTAGGGAAAGAGTGTCCGGCCCCTTGAGCATCT
LS-MPRA Adapters	enh7_5'1S	CGATAGTCGACCAATTGCTCGAGGGTGACTGGAGTTCAGACGTGTGCTCTTCCGATC*t
	enh7_5'2phos	/5Phos/GATCGGAAGAGCACACGTCTGAACTCCAGTCACCCTCGAGCAATTGGTCGACTATCG
	enh7_3'1phos	/5Phos/GGCGCGCCattaaGCTGGTAGACTgcgatCT
	enh7_3'2S	AGatcgcAGTCTACCAGCttaatGGCGCGCC*t
Amplify fragments	enh7_ampF	CGATAGTCGACCAATTGCTC
	enh7_ampR	AGatcgcAGTCTACCAGC
d-MPRA assembly	Olig2_NR1_mutF	CGATAGTCGACCAATTGCTCGAcagacatcaaatcagtaagccctgttg
	Olig2_NR1_mutR	atcgcAGTCTACCAGCttaatTTGTTAGTGGCGTCTGTCCCG
	Olig2_NR2_mutF	CGATAGTCGACCAATTGCTCGAgagtggtcctcacatgcccaa
	Olig2_NR2_mutR	atcgcAGTCTACCAGCttaatCGTGTTTCCCAGCTGGCT
	Olig2_NR3_mutF	CGATAGTCGACCAATTGCTCGActaggtgcttggaccccatct
	Olig2_NR3_mutR	atcgcAGTCTACCAGCttaatAGTTGAGGCTTGGGATTCCGG
	MutF	CGATAGTCGACCAATTGCTCGA
	MutR	atcgcAGTCTACCAGCttaat
	StatadualA_gfpF	GCTGGTAGACTgcgatAcctcaCTATATAATGGAAGCTTG
	StatadualA_gfpR	CCTCGAGCAATTGGTCGACTATCGATTACTTGTACAGCTCGTCCATGCCG
LS-MPRA BC sequencing	bc7_cdnaR	AAGTCAGATGCTCAAGGGGC
	bc7_cdnaF	GCAGAAGAACGGCATCAAGG
	bc7_cdnaR2	GCCGGACACTCTTTCCCTAC
d-MPRA BC sequencing	bc7_cdnaR_WPRE	AGCAGCGTATCCACATAGCG
	bc7_cdnaF*	GCAGAAGAACGGCATCAAGG
	MutR*	atcgcAGTCTACCAGCttaat
	dualmut_IllR1F	ACACTCTTTCCCTACACGACGCTCTTCCGATCtACCAATTGCTCGAGG

	dualmut_IllR2F	ACACTCTTTCCCTACACGACGCTCTTCCGATCTACCAATTGCTCG ACA
	dualmut_IllR2R	GTGACTGGAGTTCAGACGTGTGCTCTTCCGATCtgcAGTCTACCAG Cttaat
Construct vector	compvec_F	CAGCTCACTCAAAGGCGGTA
	compvec_R	CCTCGAGCAATTGGTCGACTATC
Olig2-NR1 and -NR2 constructs	Olig2_NR1F	GACCAATTGCTCGAGGcagacatcaaatcagtaagccctgttg
	Olig2_NR1R	ATGTGCTTTTttgttagtggcgtctgtcccg
	Olig2_NR2F	GACCAATTGCTCGAGGgagtggtcctcacatgccc
	Olig2_NR2R	GGAACAATGTGCTTTTcgtgtttcccagctggc
	Olig2_minpr-GFPint	AAAAGCACATTGTTCCCGCC
	GFPint_vecR	GCCTTTGAGTGAGCTGgccctcccatatgtccttcc
Olig2-NR3 construct	Olig2_NR3F	GACATATGGGAGGGCCTAGGTGCTTGGACCCCATC
	Olig2_NR3R	GCCTTTGAGTGAGCTGagttgaggcttgggattccg
	Vec_GFPintF	gaccaattgctcgaggAAAAGCACATTGTTCCCGCC
	GFPint_R	GCCCTCCCATATGTCCTTCC
Olig2-composite construct	Olig2_NR1F*	GACCAATTGCTCGAGGcagacatcaaatcagtaagccctgttg
	Olig2comp_NR1R	GGACCACTCttgttagtggcgtctgtccc
	Olig2comp_NR2F	cactaacaaGAGTGGTCCTCACATGCCCa
	Olig2_NR2R*	GGAACAATGTGCTTTTcgtgtttcccagctggc
	Olig2_minpr-GFPint*	AAAAGCACATTGTTCCCGCC
	GFPint_R*	GCCCTCCCATATGTCCTTCC
	Olig2_NR3F*	GACATATGGGAGGGCCTAGGTGCTTGGACCCCATC
	Olig2_NR3R*	GCCTTTGAGTGAGCTGagttgaggcttgggattccg
Backbone control constructs	Vec_GFPintF*	gaccaattgctcgaggAAAAGCACATTGTTCCCGCC
	Vec_nominprGFPF	accaattgctcgaggGCCACCATGGTGAGCAAG
	GFPint_R*	GCCCTCCCATATGTCCTTCC
Ngn2-CRM1, -CRM2, and -CRM3 constructs	Ngn2-CRM1_F	ACCAATTGCTCGAGGgaagattgggagtatgaatagttgtc
	Ngn2-CRM1_R	atcgcAGTCTACCAGCaatgctcacatcctccctcag
	Ngn2-CRM2_F	ACCAATTGCTCGAGGtctcatcagtcccaaaactggc
	Ngn2-CRM2_R	atcgcAGTCTACCAGCaatgatggtgggatggagag
	Ngn2-CRM3_F	ACCAATTGCTCGAGGactcgggcccctaatgagc
	Ngn2-CRM3_R	atcgcAGTCTACCAGCtttatctaatcagcataaaatggttctaaagctcc
	TATAminpr_F	GCTGGTAGACTgcgatCT
	GFPint_vecR	GCCTTTGAGTGAGCTGgccctcccatatgtccttcc
Ngn2-CRM4 construct	Ngn2-CRM4_F	GACATATGGGAGGGCcctaaaagtgagaagcctggag
	Ngn2-CRM4_R	GCCTTTGAGTGAGCTGcaaggaggcaataaaccccc
	Vec_TATAminpr_F	GACCAATTGCTCGAGGGCTGGTAGACTgcgatCT
	GFPint_R*	GCCCTCCCATATGTCCTTCC
cOLIG2-CRM1 construct	cOLIG2_CRM1F	ACCAATTGCTCGAGGaccaaagagttaatttgcgtttttaaacc
	cOLIG2_CRM1R	CTTTATAGCCGCGCCGGGctgctgtaatgtttttgttatttttcctc
	cOLIG2_promF	cccggcgcggctataaaggc
	cOLIG2_promR	CTCACCATGGTGGCggctctcaccgtgctcgggg
	GFPint_F	GCCACCATGGTGAGCAAG
	GFPint_vecR*	GCCTTTGAGTGAGCTGGCCCTCCCATATGTCCTTCC
cOLIG2-CRM2 construct	cOLIG2_CRM2F	ACCAATTGCTCGAGGgttacgcgttacgatggatctgac
	cOLIG2_promR*	CTCACCATGGTGGCggctctcaccgtgctcgggg
	GFPint_F*	GCCACCATGGTGAGCAAG
	GFPint_vecR*	GCCTTTGAGTGAGCTGGCCCTCCCATATGTCCTTCC
cOLIG2-CRM3 construct	cOLIG2_CRM3F	GACATATGGGAGGGCgctcccattggtcagcgctg
	cOLIG2_CRM3R	GCCTTTGAGTGAGCTGagcccgtaatcccgcgc
	cOLIG2-vec_promF	ACCAATTGCTCGAGGcccggcgcggctataaaggc

	cOLIG2_promR*	CTCACCATGGTGGCggctctcaccgtgctcgggg
	GFPint_R*	GCCCTCCCATATGTCCTTCC
ddPCR	Olig2_qF	GCGAGCACCTCAAATCTAATTC
	Olig2_qR	AAAAGATCATCGGGTTCTGGG
	Hprt_qF	CCCCAAAATGGTTAAGGTTGC
	Hprt_qR	AACAAAGTCTGGCCTGTATCC
	*reused	

Table S2: Genome Coordinates for ROIs				
Genome	Chromosome	Start	End	Description
mm10	chr6	115930332	115930431	Rho PPR (Zack et al., 1991)
	chr6	115931731	115931977	Rho RER (Nie et al., 1996)
	chr6	115928742	115929214	Rho CBR (Corbo et al., 2010)
	chr11	50842558	50842758	Grm6 CRM (Kim et al., 2008)
	chr12	84567682	84569914	Vsx2 2.4 kb promoter CRM (Rowan et al., 2005)
	chr12	84552103	84552267	Vsx2 164 bp enhancer CRM (Kim et al., 2008)
	chr12	84532102	84532711	Vsx2 ECR4 homologue (Buenaventura et al., 2018)
	chr12	84532049	84533013	Vsx2 CRC-SE-mR0-37 (Honnell et al., 2022)
	chr12	84550173	84553991	Vsx2 CRC-SE-mR3-17 (Honnell et al., 2022)
	chr7	13397865	13398310	Cabp5 CRM (Kim et al., 2008)
	chr16	91140523	91140769	Olig2-NR1
	chr16	91223668	91223849	Olig2-NR2
	chr16	91232270	91232482	Olig2-NR3
	chr16	91225474	91225600	Olig2 minimal promoter
	chr16	91235256	91238546	Olig2-K23 (Sun et al., 2006)
	chr16	91139504	91141503	Olig2-ULTRA (Chen et al., 2008)
	chr16	91223550	91225549	Olig2-basal promoter (Chen et al., 2008)
	chr16	91191767	91193766	Olig2-EC2 (Fan et al., 2023)
	chr16	91208209	91211318	Olig2-5F7 (Friedli et al., 2010)
	chr3	127628497	127632832	Ngn2-TgN2 (Simmons et al., 2001)
	chr3	127642407	127642608	Ngn2-CRM1
	chr3	127605638	127605854	Ngn2-CRM2
	chr3	127632596	127632883	Ngn2-CRM3
	chr3	127572578	127572810	Ngn2-CRM4
galGal6	chr1	106522687	106522790	cOLIG2 minimal promoter
	chr1	106486012	106486309	cOLIG2-CRM1
	chr1	106522473	106522687	cOLIG2-CRM2
	chr1	106531687	106531776	cOLIG2-CRM3

Table S3: Association Library characteristics							
Gene-of-interest	**Cabp5**	**Grm6**	**Rho**	**Vsx2**	**Olig2**	**Neurog2**	**cOLIG2**
BAC clone	RP23-125H22	RP23-417M10	RP23-219M6	RP23-127O21	CH29-613L21	RP23-182M12	CH261-60J3
Size of clone (bp)	175,529	196,198	205,479	224,092	198,802	176,837	234,491
Sequenced reads	32,993,015	35,980,528	33,804,998	38,542,527	99,453,803	123,039,602	104,836,048
Unique fragments sequenced	6,742,335	6,342,682	6,528,168	5,065,113	7,273,814	9,236,041	11,579,155
Predicted total unique fragments (Vmax)	9,349,334	8,328,615	8,750,444	6,151,434	7,882,427	10,090,748	13,254,886
Estimated under-sequencing (fragments)	27.9%	23.8%	25.4%	17.7%	7.7%	8.5%	12.6%
Unique barcode–fragment pairings	9,283,048	8,115,758	8,339,844	7,121,265	17,931,082	27,383,903	44,774,642
Unique barcodes sequenced	2,745,009	3,299,572	3,434,846	3,541,130	6,494,202	7,894,680	6,859,915
Predicted total unique barcodes (Vmax)	3,033,326	3,694,093	3,902,617	3,991,963	6,911,736	8,419,118	7,213,082
Estimated under-sequencing (barcodes)	9.5%	10.7%	12.0%	11.3%	6.0%	6.2%	4.9%
Mean barcodes per fragment±SD	1.38±0.91	1.28±0.73	1.28±0.73	1.41±0.85	2.47±3.23	2.96±3.51	3.87±4.06
Fragments with 1 BC (%)	5,114,287 (75.9)	5,091,388 (80.3)	5,270,065 (80.7)	3,719,724 (73.4)	3,417,706 (47.0)	3,959,601 (42.9)	3,734,149 (32.2)
Barcode Collisions (%)	1,735,600 (63.2)	1,794,631 (54.4)	1,848,433 (53.8)	1,674,020 (47.3)	3,916,149 (60.3)	5,250,728 (66.5)	5,080,559 (70.1)

Table S4: Profiled Abundance Libraries			
Abundance Library	**Fragments observed in RNA**	**Total fragments in Association Library**	**Percent profiled**
Multiplex-ExVivo-A_Cabp5	40,810	6,742,335	0.61%
Multiplex-ExVivo-B_Cabp5	32,018		0.47%
Multiplex-ExVivo-C_Cabp5	65,346		0.97%
Multiplex-InVivoP10-1_Cabp5	62,482		0.93%
Multiplex-InVivoP10-2_Cabp5	52,526		0.78%
Multiplex-InVivoP10-3_Cabp5	84,138		1.25%
Multiplex-ExVivo-A_Grm6	16,902	6,342,682	0.27%
Multiplex-ExVivo-B_Grm6	14,886		0.23%
Multiplex-ExVivo-C_Grm6	41,249		0.65%
Multiplex-InVivoP10-1_Grm6	23,755		0.37%
Multiplex-InVivoP10-2_Grm6	19,854		0.31%
Multiplex-InVivoP10-3_Grm6	43,001		0.68%
Multiplex-ExVivo-A_Rho	26,371	6,528,168	0.40%
Multiplex-ExVivo-B_Rho	18,541		0.28%
Multiplex-ExVivo-C_Rho	20,949		0.32%
Multiplex-InVivoP10-1_Rho	47,920		0.73%
Multiplex-InVivoP10-2_Rho	37,309		0.57%
Multiplex-InVivoP10-3_Rho	44,261		0.68%
Multiplex-ExVivo-A_Vsx2	9,219	5,065,113	0.18%
Multiplex-ExVivo-B_Vsx2	8,169		0.16%
Multiplex-ExVivo-C_Vsx2	23,762		0.47%
Multiplex-InVivoP10-1_Vsx2	18,753		0.37%
Multiplex-InVivoP10-2_Vsx2	14,380		0.28%
Multiplex-InVivoP10-3_Vsx2	32,321		0.64%
Olig2_LS-MPRA101	400,054	7,273,814	5.50%
Olig2_LS-MPRA202	250,985		3.45%
Olig2_LS-MPRA303	190,997		2.63%
Olig2_4hrA	223,053		3.07%
Olig2_4hrB	210,608		2.90%
Olig2_4hrC	258,610		3.56%
Olig2_12hrA	335,853		4.62%
Olig2_12hrB	323,185		4.44%
Olig2_12hrC	202,155		2.78%
Olig2_28hrA	238,341		3.28%
Olig2_28hrB	218,220		3.00%
Olig2_28hrC	212,975		2.93%
Ngn2-bc101	866,959	9,236,041	9.39%
Ngn2-bc202	754,450		8.17%
Ngn2-bc303	2,751,469		29.79%
cOLIG2_retinaA	2,441,108	11,579,155	21.08%
cOLIG2_retinaB	2,392,209		20.66%
cOLIG2_retinaC	2,557,087		22.08%
cOLIG2_retinaD	2,222,483		19.19%
cOLIG2-E2_SC1	601,082		5.19%
cOLIG2-E2_SC2	788,047		6.81%
cOLIG2-E2_SC3	1,074,630		9.28%
cOLIG2-E2_SC4	1,212,194		10.47%
cOLIG2-E4_SC1	3,719,067		32.12%
cOLIG2-E4_SC2	3,374,676		29.14%
cOLIG2-E4_SC3	2,260,800		19.52%
cOLIG2-E4_SC4	1,725,824		14.90%

Table S5. Quantification of GFP and Olig2 co-localization in embryonic mouse retina						
Plasmid	**Electroporated Olig2+ cells that express GFP protein (%)**		**GFP protein+ cells that express Olig2 (%)**		**Electroporated Olig2-cells that express GFP protein (%)**	
	GFP+	**GFP-**	**Olig2+**	**Olig2-**	**GFP+**	**GFP-**
Olig2-NR1	100	0	15.6	84.4	66.8	33.2
Olig2-NR2	100	0	29.7	70.3	48.6	51.4
Olig2-NR3	67.9	32.1	17.0	83.0	50.2	49.8
Olig2-Triple Composite	100	0	21.4	78.6	62.1	37.9

Table S6. Quantification of CRM-directed RNA and *Olig2* RNA or protein										
Plasmid	**Electroporated *Olig2* RNA+ cells that expressed GFP (%)**				***GFP* RNA+ cells that expressed *Olig2* RNA (%)**		**GFP protein+ cells that expressed *Olig2* RNA (%)**		***Olig2* RNA-cells that expressed GFP (%)**	
	***GFP* RNA only**	***GFP* RNA & protein**	**GFP protein only**	**GFP-**	***Olig2* RNA+**	***Olig2* RNA-**	***Olig2* RNA+**	***Olig2* RNA-**	**GFP+**	**GFP-**
Olig2-NR1	19.3	49.8	30.2	0.64	52.6	47.4	40.6	59.4	57.7	42.3
Olig2-NR2	35.6	45.5	10.9	8.0	64.5	35.5	38.8	61.2	27.9	72.1
Olig2-NR3	34.0	5.1	0.0	60.9	39.6	60.4	35.7	64.3	5.5	94.5
Olig2-Triple Composite	14.2	55.0	25.0	5.8	63.3	36.7	46.0	54.0	63.5	36.5

Table S7. Quantification of CRM-directed RNA and *Ngn2* RNA or protein										
Plasmid	**Electroporated *Ngn2* RNA+ cells that expressed GFP (%)**				***GFP* RNA+ cells that expressed *Ngn2* RNA (%)**		**GFP protein+ cells that expressed *Ngn2* RNA (%)**		***Ngn2* RNA-cells that expressed GFP (%)**	
	***GFP* RNA only**	***GFP* RNA & protein**	**GFP protein only**	**GFP-**	***Ngn2* RNA+**	***Ngn2* RNA-**	***Ngn2* RNA+**	***Ngn2* RNA-**	**GFP+**	**GFP-**
Ngn2-CRM1	22.2	30.6	3.7	43.5	6.6	93.4	6.5	93.5	48.2	51.8
Ngn2-CRM2	7.3	86.4	3.3	2.9	20.7	79.3	19.7	80.3	88.8	11.2
Ngn2-CRM3	32.9	59.6	4.4	3.1	38.5	61.5	32.3	67.7	69.3	30.7
Ngn2-CRM4	9.4	0	0	90.6	11.9	88.1	10.6	89.4	14.8	85.2
Ngn2-CRM3 (reduced ex vivo culture)	24.8	60.2	7.7	7.2	49.2	50.8	44.0	56.0	39.3	60.7

Table S8. Quantification of CRM-directed RNA and *cOLIG2* RNA or protein										
Plasmid	**Electroporated *cOLIG2* RNA+ cells that expressed GFP (%)**				***GFP* RNA+ cells that expressed *cOLIG2* RNA (%)**		**GFP protein+ cells that expressed *cOLIG2* RNA (%)**		***cOLIG2* RNA- cells that expressed GFP (%)**	
	***GFP* RNA only**	***GFP* RNA & protein**	**GFP protein only**	**GFP-**	***cOLIG2* RNA+**	***cOLIG2* RNA-**	***cOLIG2* RNA+**	***cOLIG2* RNA-**	**GFP+**	**GFP-**
cOLIG2-CRM1	5.5	90.3	1.7	2.5	45.7	54.3	45.3	54.7	68.2	31.8
cOLIG2-CRM2	4.1	90.9	3.5	1.5	34.5	65.5	32.5	67.5	74.6	25.4
cOLIG2-CRM3	1.0	0	0	98.9					0.4	99.6

Table S9. Quantification of GFP and Olig2 co-localization in postnatal mouse retina						
Plasmid	**Electroporated Olig2+ cells that express GFP protein (%)**		**GFP protein+ cells that express Olig2 (%)**		**Electroporated Olig2-cells that express GFP protein (%)**	
	GFP+	**GFP-**	**Olig2+**	**Olig2-**	**GFP+**	**GFP-**
Olig2-NR1	99.5	0.5	88.0	12.0	68.0	32.0
Olig2-NR2	97.9	2.1	85.3	14.7	51.1	48.9
Olig2-NR3	95.8	4.2	70.8	29.2	56.2	43.8
Olig2-Triple Composite	99.8	0.2	80.9	19.1	65.8	34.2

Supplemental Document A.

Association Library Supplemental QC plots

Fragment size distribution plots

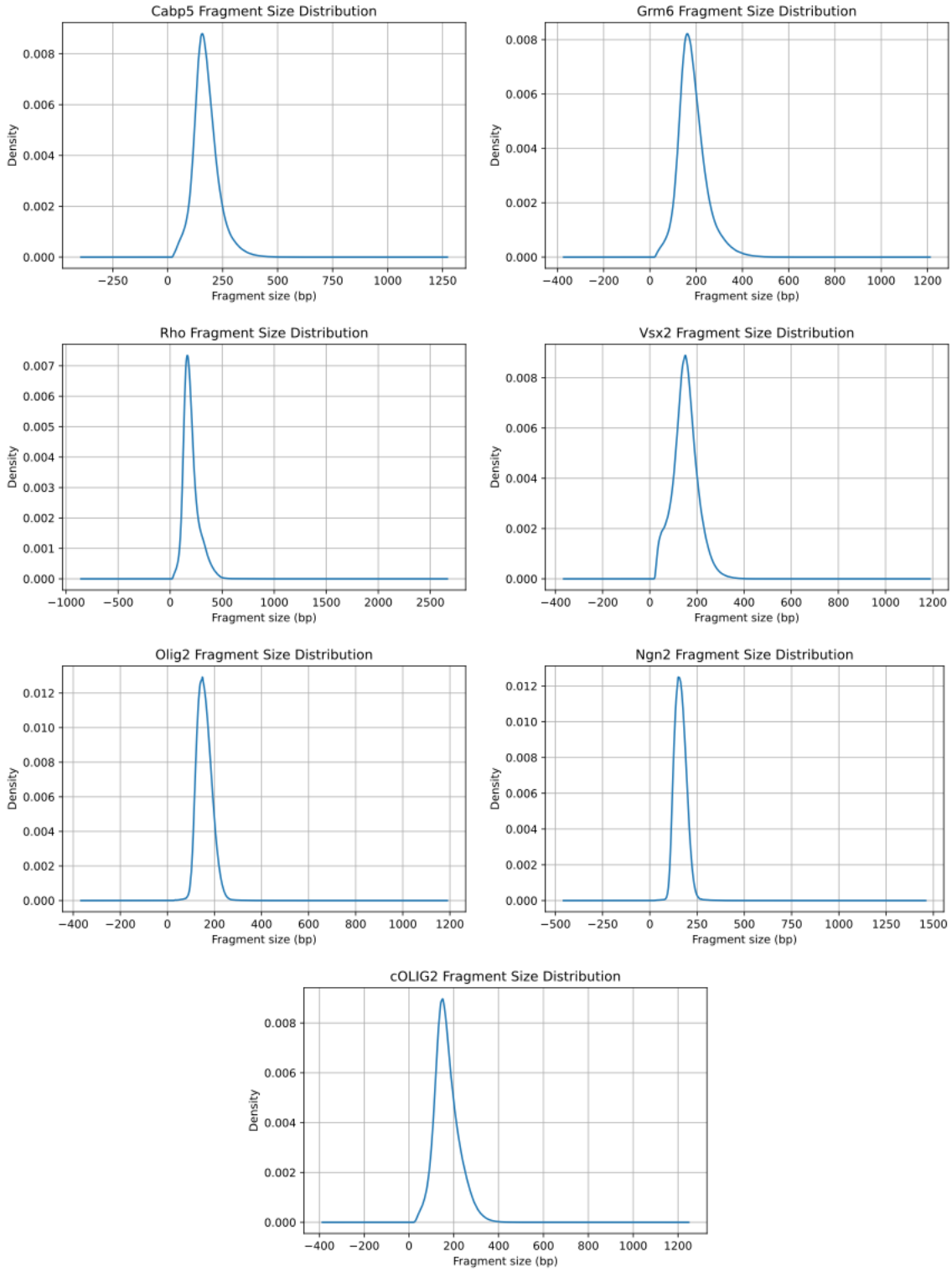

Correlation between fragment size and activity plots

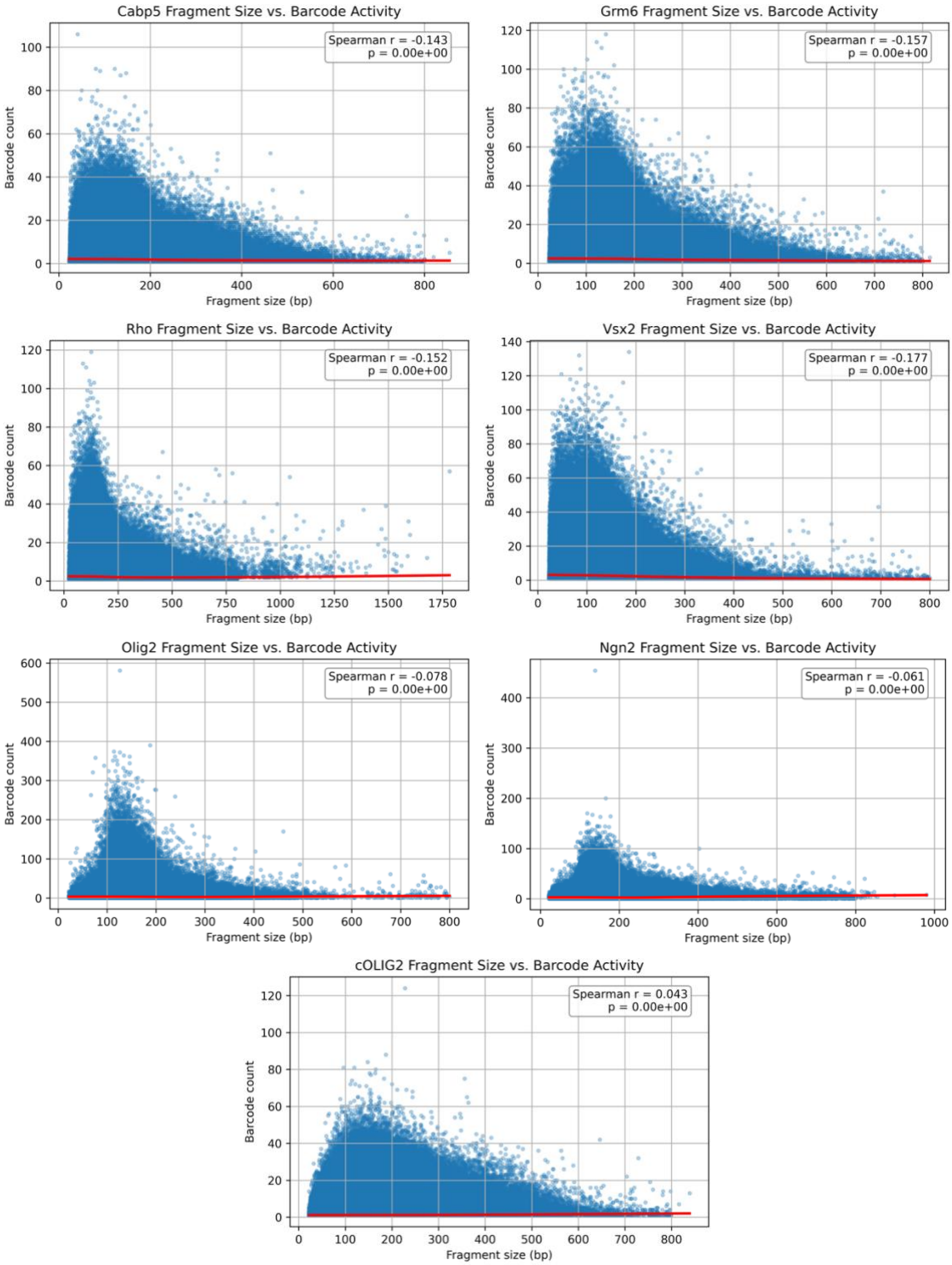

Barcode and sequence saturation curves

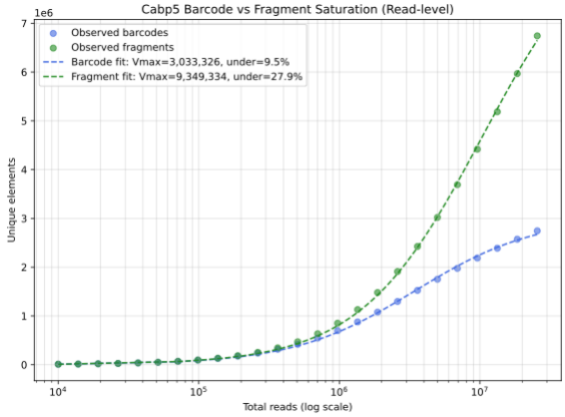

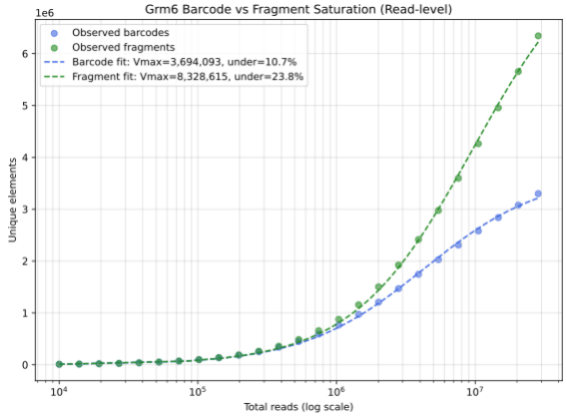

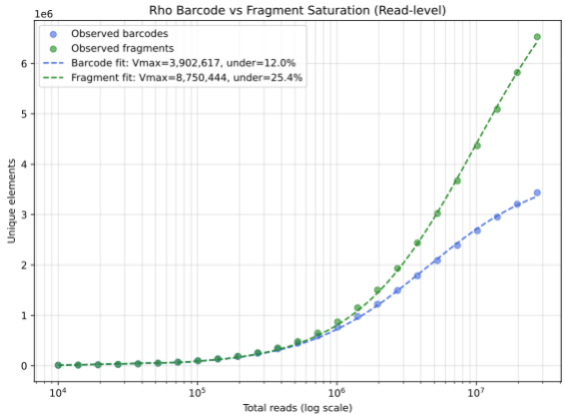

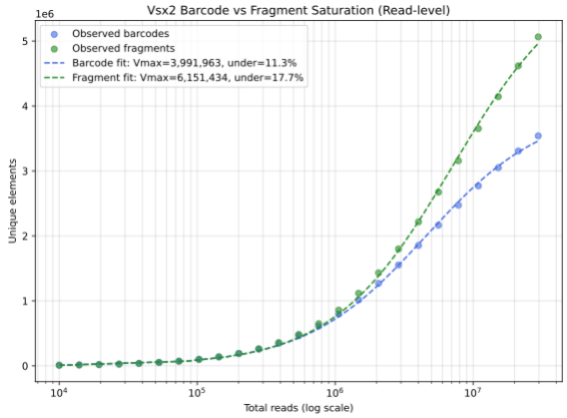

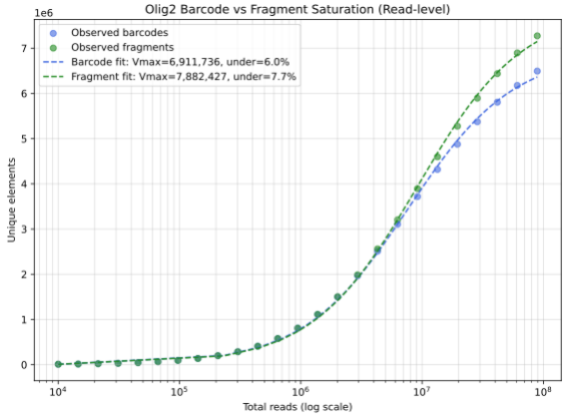

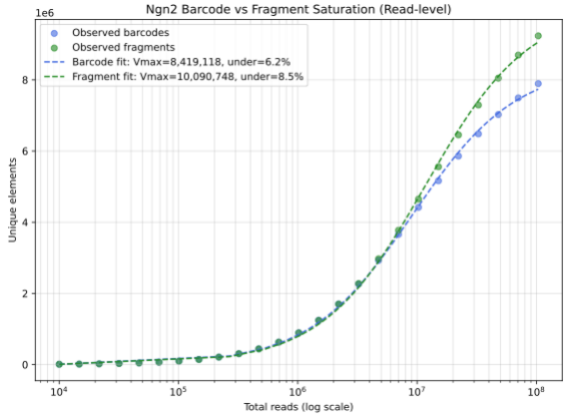

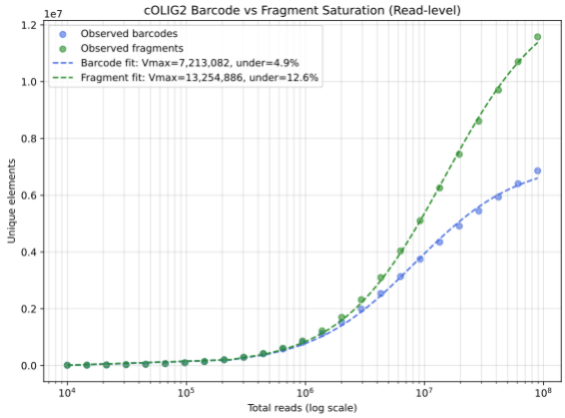

Unique barcode-fragment pair saturation curves

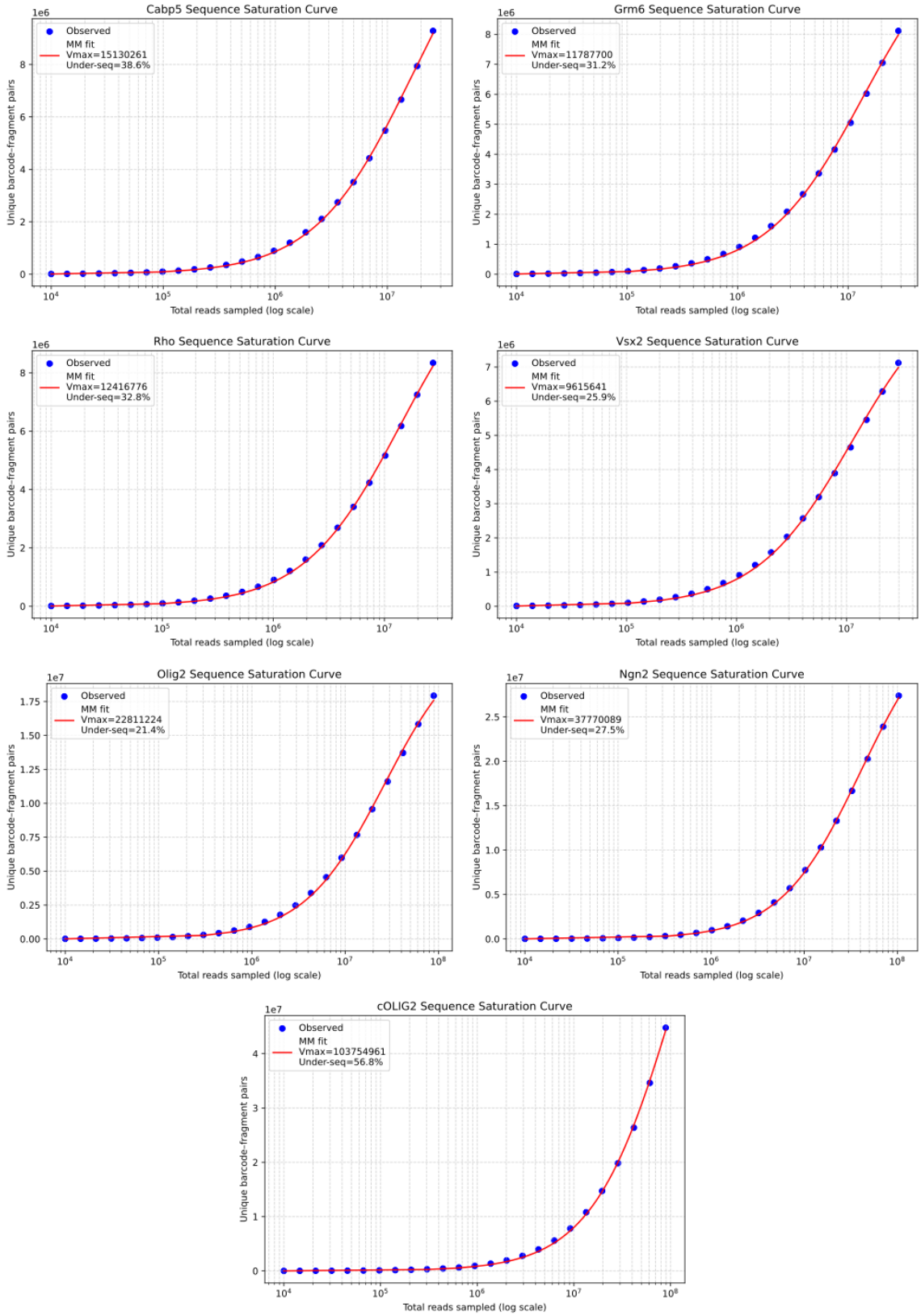

D-MPRA Library Supplemental QC plots

Note: d-MPRA libraries were sequenced with different designated names than those in the main text. For the below supplemental plots:
Olig2_NR1 corresponds with the Olig2-NR2 library in the main text
Olig2_NR2 corresponds with the Olig2-NR3 library in the main text
Olig2_NR3 corresponds with the Olig2-NR1 library in the main text

Substitution Rate across CRM regions

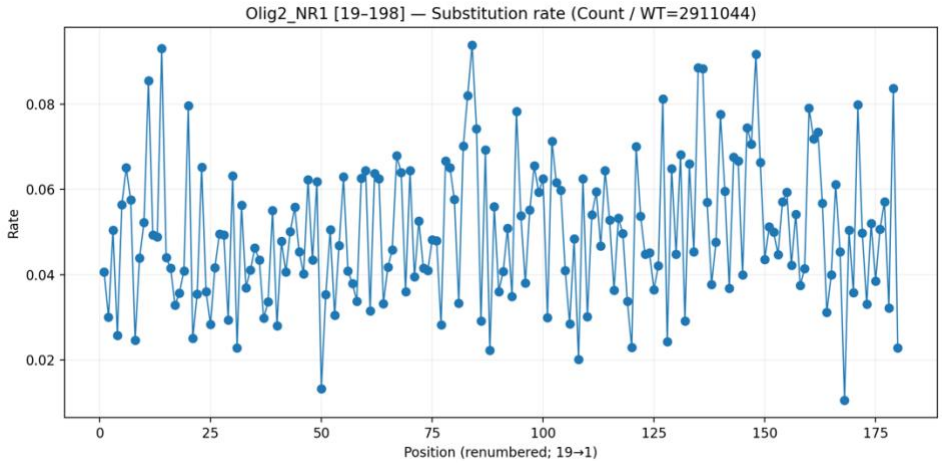

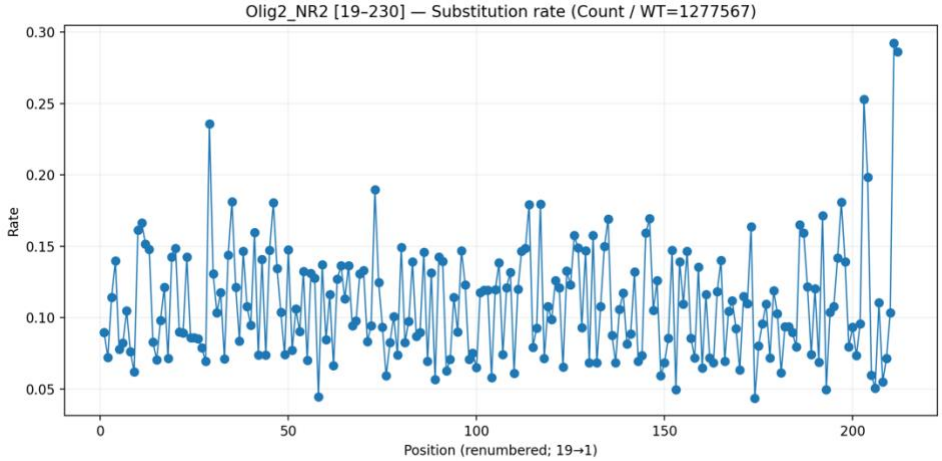

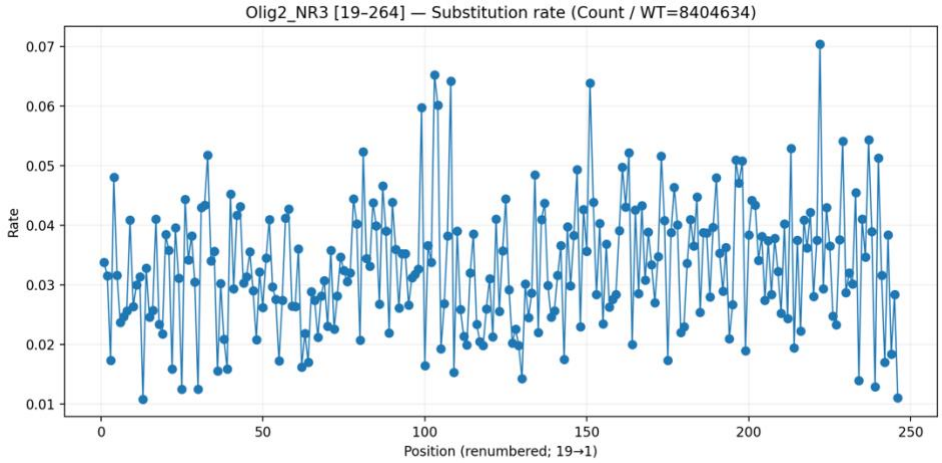

Co-occurrence of substitutions across CRM region

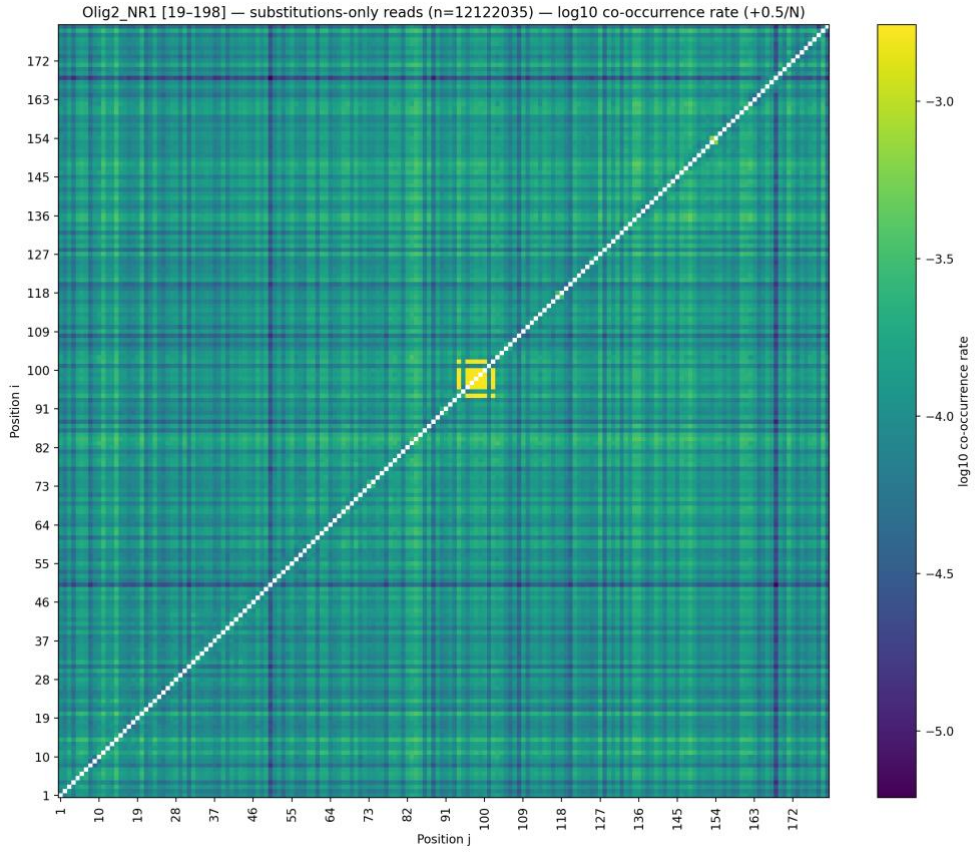

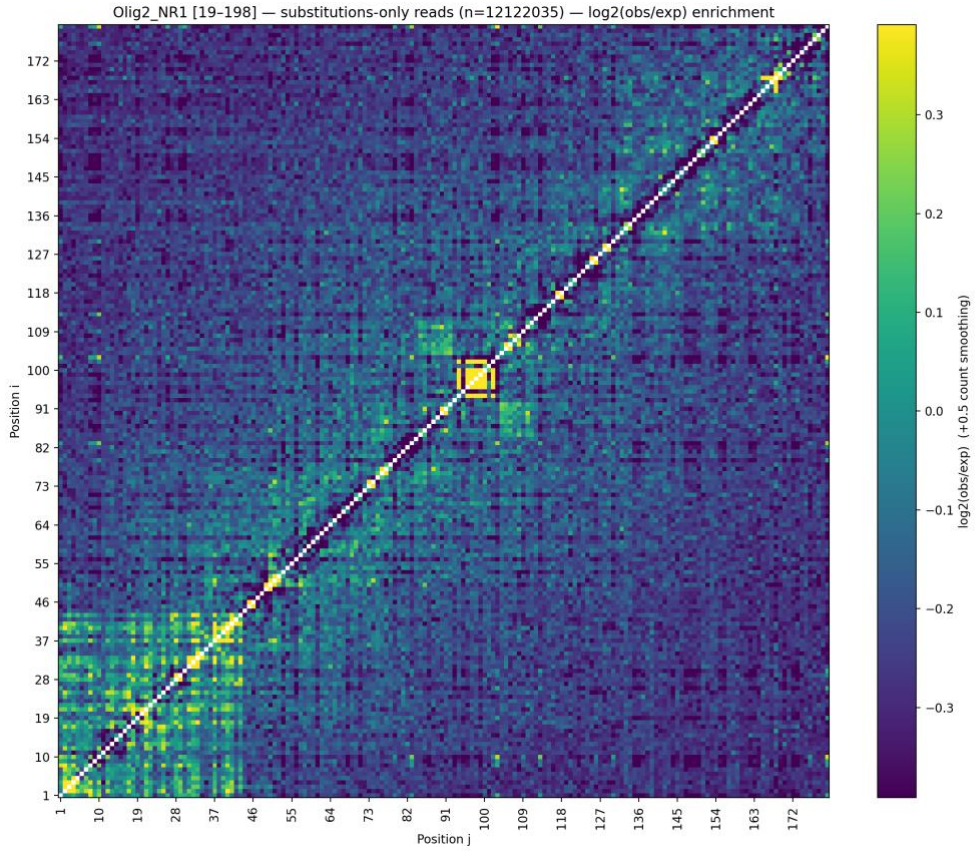

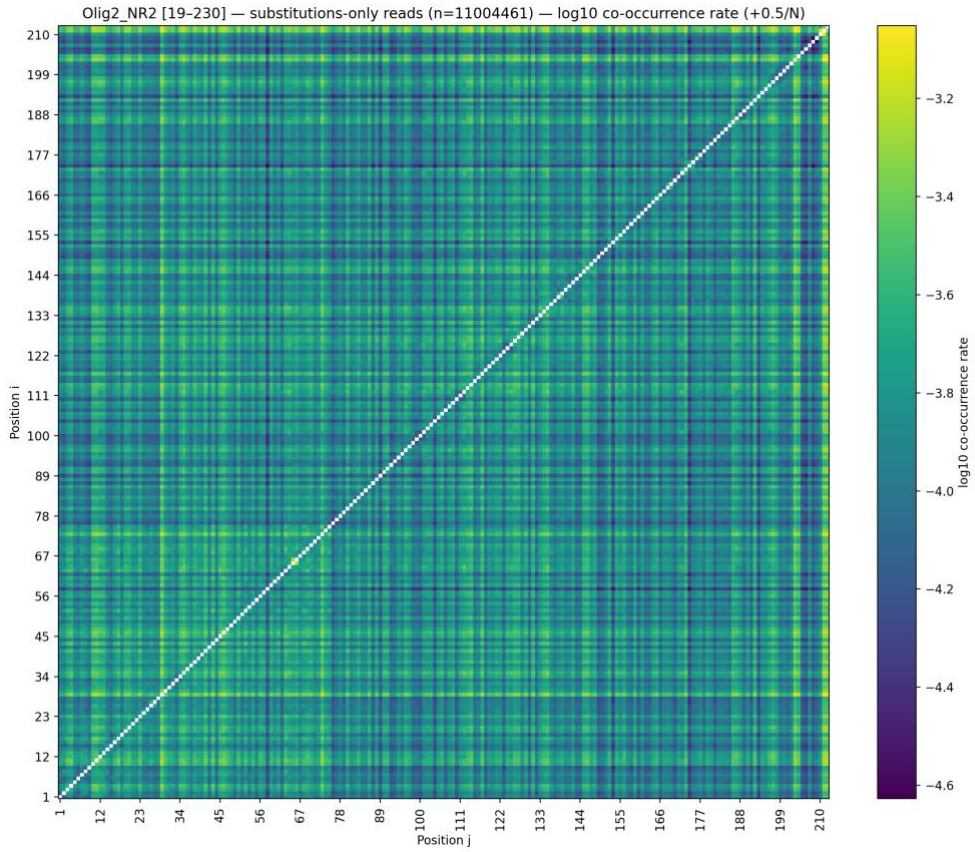
Olig2_NR2 [19–230] — substitutions-only reads (n=11004461) — log10 co-occurrence rate (+0.5/N)
Position i
Position j
log10 co-occurrence rate
−3.2
−3.4
−3.6
−3.8
−4.0
−4.2
−4.4
−4.6

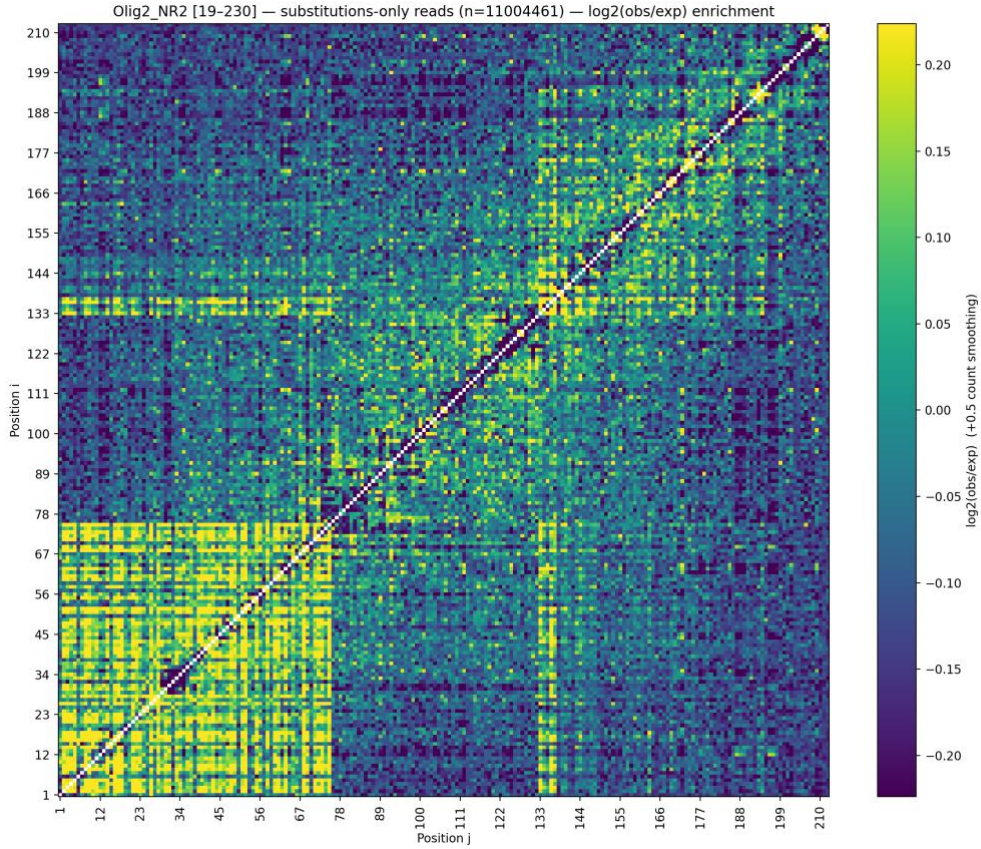
Olig2_NR2 [19–230] — substitutions-only reads (n=11004461) — log2(obs/exp) enrichment
Position i
Position j
log2(obs/exp) (+0.5 count smoothing)
0.20
0.15
0.10
0.05
0.00
−0.05
−0.10
−0.15
−0.20

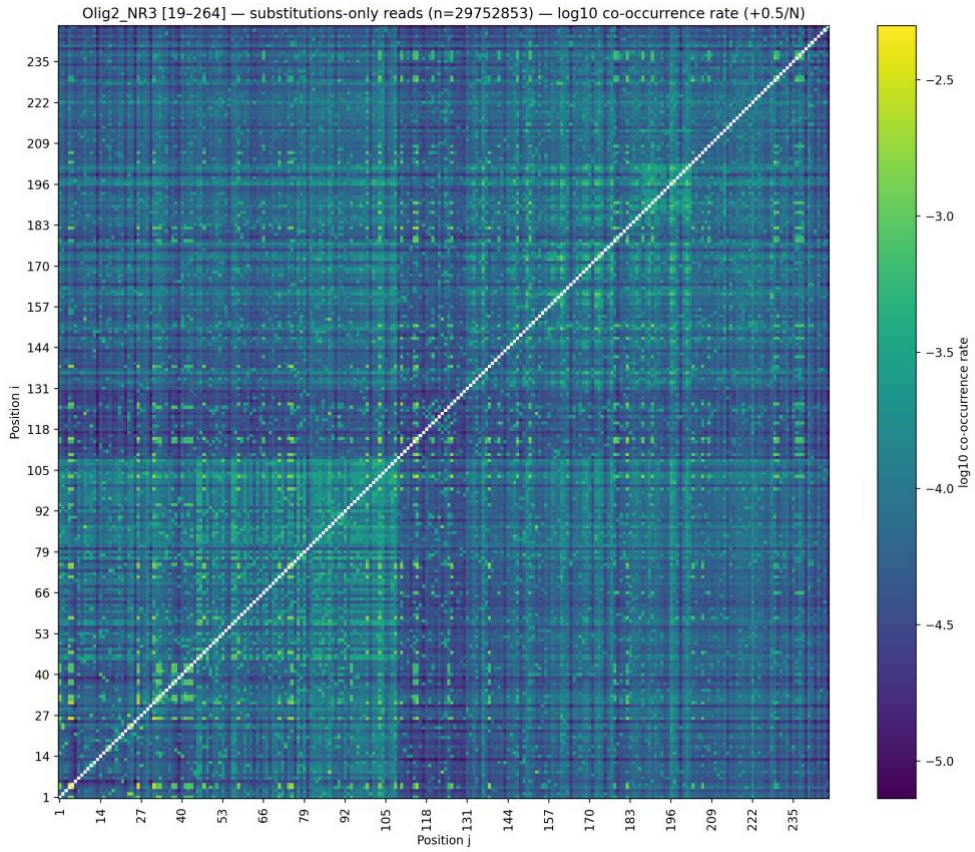
Olig2_NR3 [19–264] — substitutions-only reads (n=29752853) — log10 co-occurrence rate (+0.5/N)
Position i
Position j
log10 co-occurrence rate
−2.5
−3.0
−3.5
−4.0
−4.5
−5.0

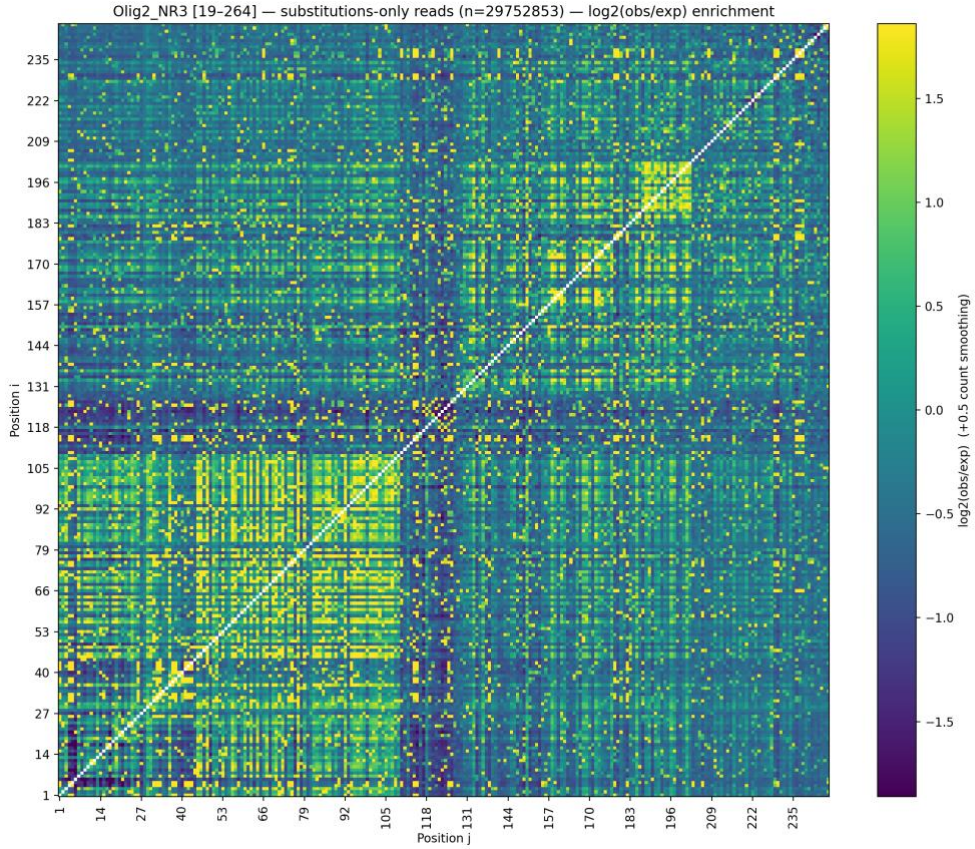
Olig2_NR3 [19–264] — substitutions-only reads (n=29752853) — log2(obs/exp) enrichment
Position i
Position j
log2(obs/exp) (+0.5 count smoothing)
1.5
1.0
0.5
0.0
−0.5
−1.0
−1.5

Comparison of Singleton vs Bulk analysis

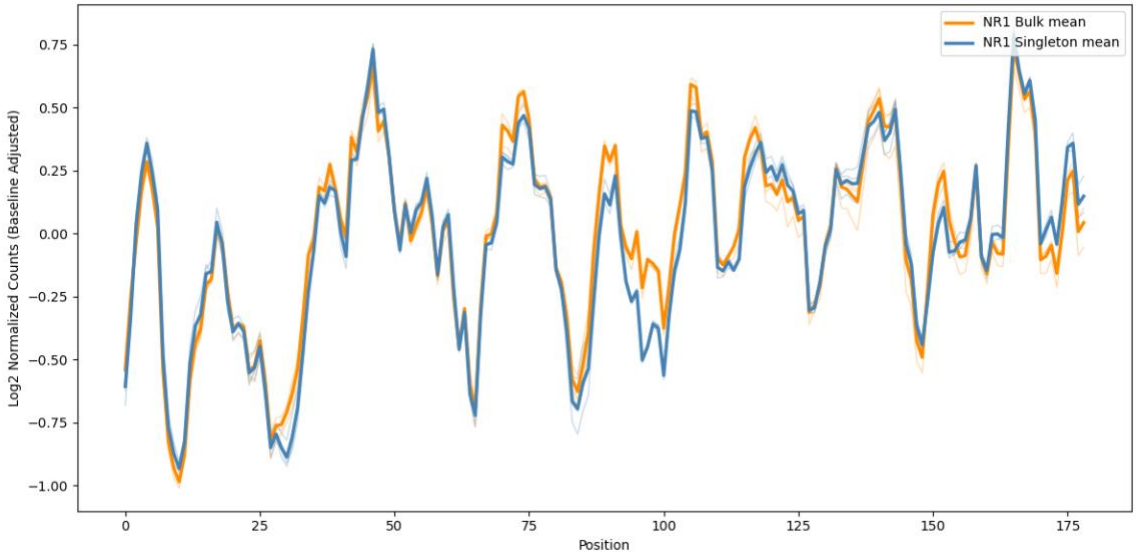

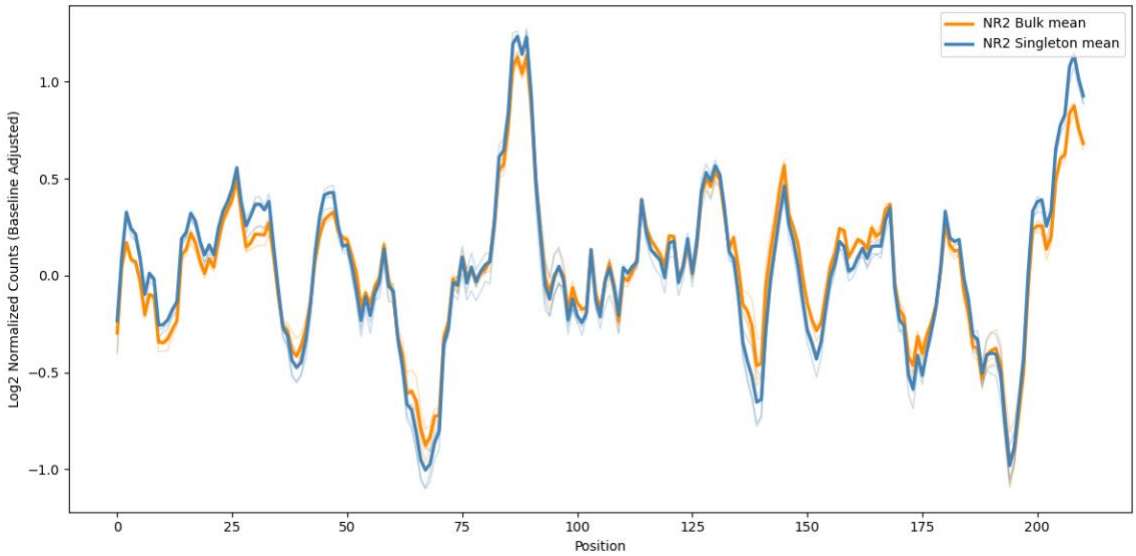

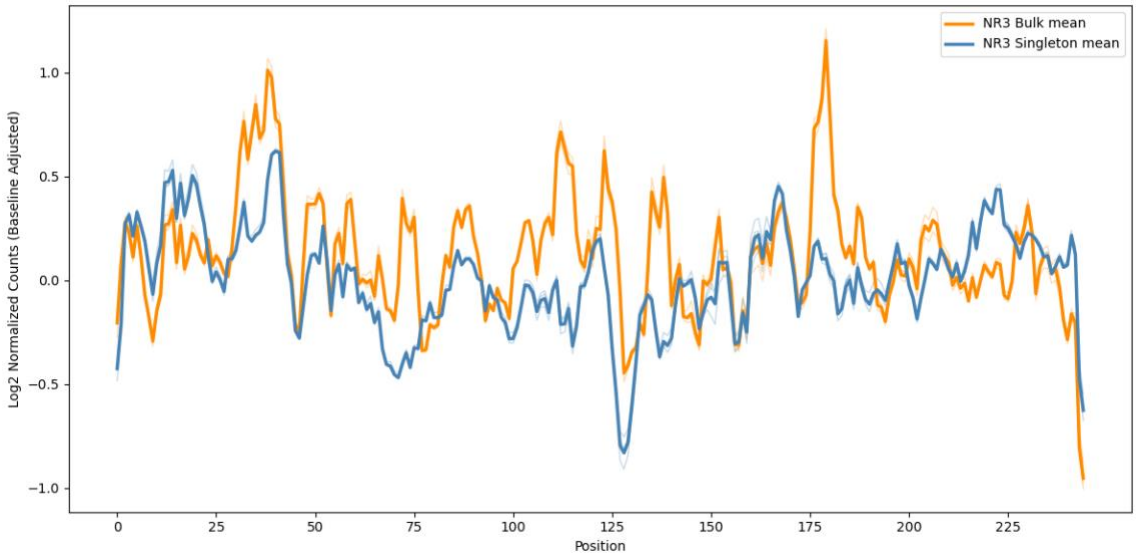
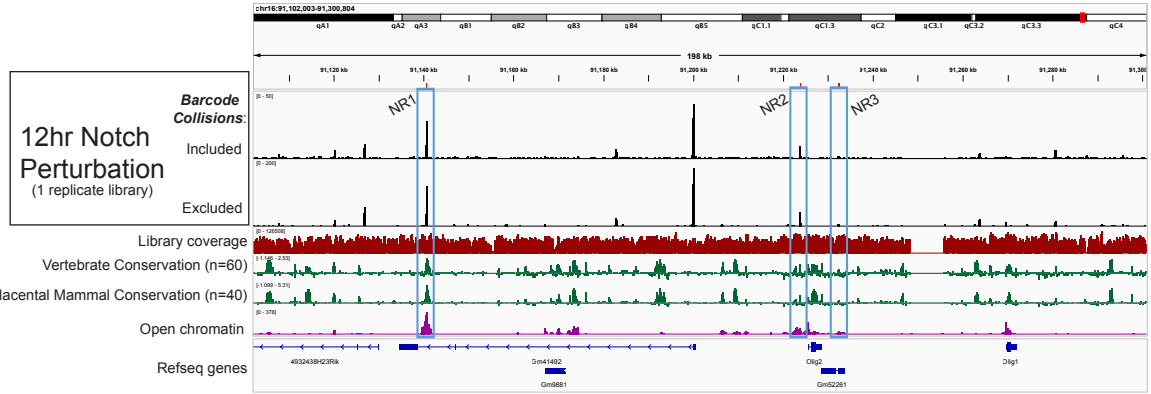
Supplemental Document B.